Searches for Supersymmetric signatures in all hadronic final states with the α_T variable.

Darren Burton

Imperial College London
Department of Physics

A thesis submitted to Imperial College London
for the degree of Doctor of Philosophy

Abstract

A search for supersymmetric particles with in events with a missing energy signature and high p_T jets, is conducted using data recorded by the Compact Muon Solenoid detector based at the Large Hadron Collider. The analysis is performed with 11.7 fb^{-1} of data, collected with a center-of-mass collision energy of 8 TeV during the 2012 run period. The dimensionless kinematic variable α_T is used as a tool to select events with genuine missing energy signatures, whilst Standard Model backgrounds in the signal region are estimated using data driven control samples, which have similar kinematic to the signal region. No excess of over Standard Model expectations is found. Exclusion limits are set at the 95% confidence level in the parameter space of a range of supersymmetric simplified model topologies, with special emphasis on those with compressed spectra (small mass splittings) and natural SUSY scenarios (large number of b flavoured quarks). A complementary method to search for natural SUSY signatures with a high number of b-flavoured jets, through the use of a simple template fit is also presented. The event selections of the α_T search are used as a vehicle to demonstrate proof of principle of the technique in both data and simulation. Estimated Standard Model backgrounds from the template fits are compared with those determined from the data driven background estimation method of the α_T search within the signal search region, where good agreement between the individual predictions and that of data are observed. Additionally the efficiency of the hadronic Level-1 single jet triggers are measured throughout the 2012 run period, where a change to the jet seed algorithm was implemented during the data taking period. This change was introduced to negate an increase in rate which can be attributed to pileup jets, whilst maintaining similar performance in the triggering of physics events.

Declaration

I, the author of this thesis, declare that the work presented within this document to be my own. The work presented in Chapters 4, 5, 6 and Section 3.4, is a result of the author's own work or that of which I have been a major contributor unless explicitly stated otherwise, and is carried out within the context of the Imperial College London and CERN SUSY groups, itself a subsection of the greater CMS collaboration. All figures and studies taken from external sources are referenced appropriately throughout this document.

Darren Burton

Acknowledgements

I would like to thank the many people whom I have had the pleasure of working with during the course of the last three and a half years. The opportunity to work as part one of the largest scientific collaborations during one of the most exciting times in particle physics for decades, has been a real privilege to be a part of. I could not have achieved the results presented in this thesis without the help of my colleagues who were part of the RA1 team, Edward Laird, Chris Lucas, Henning Flaecher, Yossof Eshaq, Bryn Mathais, Sam Rogerson, Zhaoxia Meng and Georgia Karapostoli whom I worked with on L1 jets. I also thank my supervisor Oliver Buchmuller for his guidance in getting me to this point.

I also feel it important to single out thanks to the postdocs that I have worked with during my PhD. Jad Marrouche from whom I have learnt a great deal and Robert Bainbridge who has been like a second supervisor to me, helping me during my time at Imperial and CERN, especially during those most stressful of times approaching conference deadlines!

My fellow PhD students who I live with and have seen on an almost daily basis for the last few years, Andrew Gilbert, Patrick Owen, Indrek Sepp, Matthew Kenzie and my girlfriend Hannah. Thanks for putting up with the whinging, complaining and clomping.

Finally my largest thanks go to my Mum and Dad whose patience, encouragement and considerable financial support have allowed me to take the many steps that lead me here today.

Contents

List of Figures

List of Tables

"The Universe is about 1,000,000 years old."

— Matthew Kenzie, 1987-present : Discoverer of the Higgs Boson.

Chapter 1.

Introduction

During the 20th century, great advances have been made in the human understanding of the universe, it's origins, it's future and its composition. The Standard Model (SM) first formulated in the 1960's is one of the crowning achievements in science's quest to explain the most fundamental processes and interactions that make up our universe. It has provided a highly successful explanation of a wide range of phenomena in Particle Physics and has stood up to extensive experimental scrutiny [1].

Despite it's successes it is not a complete theory, with significant questions remaining unanswered. It describes only three of the four known forces with gravity not incorporated within the framework of the SM. Cosmological experiments infer that just $\sim 4\%$ of the observable universe exists as matter, with elusive "Dark Matter" accounting for a further $\sim 23\%$ [2]. However no particle predicted by the SM is able to account for it. At higher energy scales and small distances, the (non-)unification of the fundamental forces point to problems with the SM at least at higher energies not yet probed experimentally.

Many theories exist as extensions to the SM, predicting a range of observables that can be detected at the Large Hadron Collider (LHC) of which SUperSYmmetry (SUSY) is one such example. It predicts a new symmetry of nature in which all current particles in the SM would have a corresponding supersymmetric partner. Common to most Supersymmetric theories is a stable, weakly interacting Lightest Supersymmetric Partner (LSP), which has the properties of a possible dark matter candidate. The SM and the main principles of Supersymmetric theories are outlined in Chapter 2, with emphasis placed on how experimental signatures of SUSY may reveal themselves in proton collisions at the LHC.

The experimental goal of the LHC is to further test the framework of the SM, exploring the TeV mass scale for the first time, and to seek a connection between the particles produced in proton collisions and dark matter. The first new discovery by this extraordinary machine was announced on the 4th of July 2012. The long-awaited discovery was the culmination of decades of experimental endeavours in the search for the Higgs boson, providing an answer to the mechanism of electroweak symmetry breaking within the SM [3][4].

This discovery was made possible through data taken by the two multi purpose detectors (Compact Muon Solenoid (CMS) and A Toroidal LHC ApparatuS (ATLAS)) located on the LHC ring. An experimental description of the CMS detector and the LHC is described in Chapter 3, including some of the object reconstruction used by CMS in searches for SUSY signatures.

The performance of the CMS Level-1 single jet trigger, measured over the course of the year is also included within this chapter. The Level-1 triggers are of paramount importance to the recording of physics events at CMS, and to which a change in the jet seed algorithm was introduced approximately half way through the data taking period. The aim of this change, was to facilitate a reduction in the rate at which data from events not of interest to physics analyses were recorded, whilst avoiding impact on those which were.

Chapter 4, contains a description of the search for evidence of the production of Supersymmetric particles at the LHC. The main basis of the search centres around the kinematic dimensionless α_T variable, which provides strong rejection of backgrounds with fake missing energy signatures whilst maintaining good sensitivity to a variety of SUSY topologies. The author's work (as an integral part of the analysis group) is documented in detail, which has culminated in numerous publications over the past two years, the latest of which was published in the European Physical Journal C (EPJC) [5]. The results and interpretations within the framework of a variety of Simplified Model Spectra (SMS), which describe an array of possible SUSY event topologies is documented in Chapter 5.

The author in particular has played a major role in the extension of the α_T analysis into the additional b-tagged and jet multiplicity dimensions increasing the sensitivity of the analysis to a range of SUSY topologies. Additionally the author has worked extensively in both increasing the statistical precision of electroweak predictions measured from simulation through analytical techniques, and the derivation of a data driven systematic uncertainty through the establishment of closure tests within the control samples of the analysis.

Finally a method to search for SUSY signatures rich in top and bottom flavoured jet final states, is introduced in Chapter 6. These particular SUSY topologies are increasingly of interest to physicists in light of the discovery of the Higgs boson, and is discussed within the chapter. A parametrisation of the b-tagging distribution for different Electroweak processes is used to establish template shapes, which are then fitted at low b-tagged jet multiplicity (0-2), to estimate the expected number of 3 and 4 b-tagged jet events from SM processes. The α_T event selections are used to test the functionality of this template method in both data and simulation, with background predictions from the signal region selection compared to those presented in Chapter 5.

Natural units are used throughout this thesis in which $\hbar$ = c = 1.

Chapter 2.

A Theoretical Overview

Within this chapter, a brief introduction and background to the SM is given. Its success as a rigorously tested and widely accepted theory is discussed as are it's deficiencies, leading to the argument that this theory is not a complete description of our universe. The motivations for new physics at the TeV scale and in particular Supersymmetric theories are outlined within Section (2.3), with the chapter concluding with how an experimental signature of such theories can be produced and observed at the LHC, Section (2.4).

2.1. The Standard Model

The SM is the name given to the relativistic Quantum Field Theory (QFT), where particles are represented as excitations of fields, which describe the interactions and properties of all the known elementary particles [6][7][8][9]. It is a renormalisable field theory which contains three symmetries: $SU(3)$ for colour charge, SU(2) for weak isospin and U(1) relating to weak hyper charge, which require its Lagrangian $\mathcal{L}_{SM}$ to be invariant under local gauge transformation.

Within the SM theory, matter is composed of spin $\frac{1}{2}$ fermions, which interact with each other via the exchange of spin-1 gauge bosons. A summary of the known fundamental fermions and bosons is given in Table 2.1.

Fermions are separated into quarks and leptons of which only quarks interact with the strong nuclear force. Quarks unlike leptons are not seen as free particles in nature, but rather exist only within baryons, composed of three quarks with an overall integer charge, and quark-anti-quark pairs called mesons. Both leptons and quarks are grouped into

Particle	Symbol	Spin	Charge	Mass (GeV)
First Generation Fermions				
Electron Neutrino	ν_e	$\frac{1}{2}$	0	$< 2.2 \times 10^{-6}$
Electron	e	$\frac{1}{2}$	-1	0.51×10^{-3}
Up Quark	u	$\frac{1}{2}$	$\frac{2}{3}$	$2.3^{+0.7}_{-0.5} \times 10^{-3}$
Down Quark	d	$\frac{1}{2}$	$-\frac{1}{3}$	$4.8^{+0.7}_{-0.3} \times 10^{-3}$
Second Generation Fermions				
Muon Neutrino	ν_μ	$\frac{1}{2}$	0	-
Muon	μ	$\frac{1}{2}$	-1	1.05×10^{-3}
Charm Quark	c	$\frac{1}{2}$	$\frac{2}{3}$	1.275 ± 0.025
Strange Quark	s	$\frac{1}{2}$	$-\frac{1}{3}$	$95 \pm 5 \times 10^{-3}$
Third Generation Fermions				
Tau Neutrino	ν_τ	$\frac{1}{2}$	0	-
Tau	τ	$\frac{1}{2}$	-1	1.77
Top Quark	t	$\frac{1}{2}$	$\frac{2}{3}$	173.5 ± 0.8
Bottom Quark	b	$\frac{1}{2}$	$-\frac{1}{3}$	4.65 ± 0.03
Gauge Bosons				
Photon	γ	1	0	0
W Boson	$W^\pm$	1	± 1	80.385 ± 0.015
Z Boson	Z	1	0	91.187 ± 0.002
Gluons	g	1	0	0
Higgs Boson	H	0	0	125.3 ± 0.5 [4]

Table 2.1.: The fundamental particles of the SM, with spin, charge and mass displayed. Latest mass measurements taken from [1].

three generations which have the same properties, but with ascending mass in each subsequent generation.

The gauge bosons mediate the interactions between fermions. The field theories of Quantum Electro-Dynamics (QED) and Quantum Chromo-Dynamics (QCD), yield massless mediator bosons, the photon and eight coloured gluons which are consequences of the gauge invariance of those theories, detailed in Section (2.1.1).

The unification of the electromagnetic and weak-nuclear forces into the current Electroweak theory yield the weak gauge bosons, $W^\pm$ and Z through the mixing of the associated gauge fields. The force carriers of this theory were experimentally detected by the observation of weak neutral current, discovered in 1973 in the Gargamelle bubble chamber located at European Organization for Nuclear Research (CERN) [10], with the masses of the weak gauge bosons measured by the UA1 and U2 experiments at the Super Proton Synchrotron (SPS) collider in 1983 [11][12].

2.1.1. Gauge Symmetries of the SM

Symmetries are of fundamental importance in the description of physical phenomena. Noether's theorem states that for a dynamical system, the consequence of any symmetry is an associated conserved quantity [13]. Invariance under translations, rotations, and Lorentz transformations in physical systems lead to conservation of momentum, energy and angular momentum.

In the SM, a quantum theory described by Lagrangian formalism, the weak, strong and electromagnetic interactions are described in terms of "gauge theories". A gauge theory possesses invariance under a set of "local transformations", which are transformations whose parameters are space-time dependent. The requirement of gauge invariance within the SM necessitates the introduction of force-mediating gauge bosons and interactions between fermions and the bosons themselves. Given the nature of the topics covered by this thesis, the formulation of EWK within the SM Lagrangian is reviewed within this section.

The simplest example of the application of the principle of local gauge invariance within the SM is in Quantum Electro-Dynamics (QED), the consequences of which require a massless photon field [14][15].

Starting from the free Dirac Lagrangian written as

$$\mathcal{L} = \bar{\psi}(i\gamma^{\mu}\partial_{\mu} - m)\psi, \tag{2.1}$$

where ψ represents a free non interacting fermionic field, with the matrices γ^{μ}, $\mu \in 0, 1, 2, 3$ defined by the anti commutator relationship $\gamma^{\mu}\gamma^{\nu} + \gamma^{\mu}\gamma^{\nu} = 2\eta^{\mu\nu}I_4$, with $\eta^{\mu\nu}$ being the flat space-time metric $(+, -, -, -)$, and I_4 the 4×4 identity matrix.

Under a local U(1) abelian gauge transformation in which ψ transforms as:

$$\psi(x) \rightarrow \psi^{'}(x) = e^{i\theta(x)}\psi(x) \qquad \bar{\psi}(x) \rightarrow \bar{\psi}^{'}(x) = e^{i\theta(x)}\bar{\psi}(x) \tag{2.2}$$

the kinetic term of the Lagrangian will not remain invariant, due to the partial derivative interposed between the $\bar{\psi}$ and ψ yielding,

$$\partial_\mu \psi \to e^{i\theta(x)} \partial_\mu \psi + ie^{i\theta(x)} \psi \partial_\mu \theta. \tag{2.3}$$

To ensure that $\mathcal{L}$ remains invariant, a modified derivative, D_μ, that transforms covariantly under phase transformations is introduced. In doing this a vector field A_μ with transformation properties that cancel out the unwanted term in (2.3) must also be included,

$$D_\mu \equiv \partial_\mu - ieA_\mu, \qquad A_\mu \to A_\mu + \frac{1}{e}\partial_\mu \theta. \tag{2.4}$$

Invariance of the Lagrangian is then achieved by replacing ∂_μ by D_μ:

$$\begin{aligned} \mathcal{L} &= i\bar{\psi}\gamma^\mu D_\mu \psi - m\bar{\psi}\psi \\ &= \bar{\psi}(i\gamma^\mu \partial_\mu - m)\psi + e\bar{\psi}\gamma^\mu \psi A_\mu \end{aligned} \tag{2.5}$$

An additional interaction term is now present in the Lagrangian, coupling the Dirac particle to this vector field, which is interpreted as the photon in QED. To regard this new field as the physical photon field, a term corresponding to its kinetic energy must be added to the Lagrangian from Equation (2.5). Since this term must also be invariant under the conditions of Equation (2.4), it is defined in the form $F_{\mu\nu} = \partial^\mu A^\nu - \partial_\nu A_\mu$.

This then leads to the Lagrangian of QED:

$$\mathcal{L}_{QED} = .\overbrace{i\bar{\psi}\gamma^\mu \partial_\mu \psi - \frac{1}{4}F_{\mu\nu}F^{\mu\nu}}^{\text{kinetic term}} + \overbrace{m\bar{\psi}\psi}^{\text{mass term}} + \overbrace{e\bar{\psi}\gamma^\mu \psi A_\mu}^{\text{interaction term}} \tag{2.6}$$

Within the Lagrangian there remains no mass term of the form $m^2 A_\mu A^\mu$, which is prohibited by gauge invariance. This implies that the gauge particle, the photon, must be massless.

2.1.2. The Electroweak Sector and Electroweak Symmetry Breaking

The same application of gauge symmetry and the requirement of local gauge invariance can be used to unify QED and the Weak force in the Electroweak Sector (EWK). The nature of EWK interactions is encompassed within a Lagrangian invariant under transformations of the group $SU(2)_L \times U(1)_Y$.

The weak interactions from experimental observation [16], are known to violate parity and are therefore not symmetric under interchange of left and right helicity fermions. Thus within the SM the left and right handed parts of these fermion fields are treated separately. A fermion field is then split into two left and right handed chiral components, $\psi = \psi_L + \psi_R$, where $\psi_{L/R} = (1 \pm \gamma^5)\psi$.

The $SU(2)_L$ group is the special unitary group of 2×2 matrices U satisfying $UU^\dagger = I$ and det(U) $= 1$. It may be written in the form $U = e^{-i\omega_i T_i}$, with the generators of the group $T_i = \frac{1}{2}\tau_i$ where τ_i, $i \in 1,2,3$ being the 2×2 Pauli matrices

$$\tau_1 = \begin{pmatrix} 0 & 1 \\ 1 & 0 \end{pmatrix} \qquad \tau_2 = \begin{pmatrix} 0 & -i \\ i & 0 \end{pmatrix} \qquad \tau_3 = \begin{pmatrix} 1 & 0 \\ 0 & -1 \end{pmatrix}, \tag{2.7}$$

which form a non Abelian group obeying the commutation relation $[T^a, T^b] \equiv i f^{abc} T^c \neq 0$. The gauge fields that accompany this group are represented by $\hat{W}_\mu = (\hat{W}^1_\mu, \hat{W}^2_\mu, \hat{W}^3_\mu\ )$ and act only on the left handed component of the fermion field ψ_L.

One additional generator Y which represents the hypercharge of the particle under consideration is introduced through the $U(1)_Y$ group acting on both components of the fermion field, with an associated vector boson field $\hat{B}_\mu$.

The $SU(2)_L \times U(1)_Y$ transformations of the left and right handed components of ψ are summarised by,

$$\begin{aligned} \chi_L &\rightarrow \chi_L^{'} = e^{i\theta(x)\cdot T + i\theta(x)Y}\chi_L, \\ \psi_R &\rightarrow \psi_R^{'} = e^{i\theta(x)Y}\psi_R, \end{aligned} \tag{2.8}$$

where the left handed fermions form isospin doubles χ_L and the right handed fermions are isosinglets ψ_R. For the first generation of leptons and quarks this represents

$$\begin{aligned} \chi_L &= \begin{pmatrix} \nu_e \\ e \end{pmatrix}_L, & \begin{pmatrix} u \\ d \end{pmatrix}_L, \\ \psi_R &= e_R, & u_R, d_R. \end{aligned} \tag{2.9}$$

Imposing local gauge invariance within $\mathcal{L}_{EWK}$ is once again achieved by modifying the covariant derivative

$$D_\mu = \partial_\mu - \frac{ig}{2}\tau^i W^i_\mu - \frac{ig^{'}}{2} Y B_\mu, \tag{2.10}$$

where g and $g^{'}$ are the coupling constant of the $SU(2)_L$ and $U(1)_Y$ groups respectively. Taking the example of the first generation of fermions defined in Equation.(2.9), with input hypercharge values of -1 and -2 for χ_L and e_R respectively, would lead to a Lagrangian $\mathcal{L}_1$ of the form,

$$\begin{aligned} \mathcal{L}_1 =& \bar{\chi}_L \gamma^\mu [i\partial_\mu - g\frac{1}{2}\tau \cdot W_\mu - g^{'}(-\frac{1}{2})B_\mu]\chi_L \\ &+ \bar{e}_R \gamma^\mu [i\partial_\mu - g^{'}(-1)B_\mu]e_R - \frac{1}{4}W_{\mu\nu} \cdot W^{\mu\nu} - \frac{1}{4}B_{\mu\nu}B^{\mu\nu}. \end{aligned} \tag{2.11}$$

As in QED, these additional gauge fields introduce field strength tensors $B_{\mu\nu}$ and $W_{\mu\nu}$,

$$\hat{B}_{\mu\nu} = \partial_\mu \hat{B}_\nu - \partial_\nu \hat{B}_\mu \tag{2.12}$$

$$\hat{W}_{\mu\nu} = \partial_\mu \hat{W}_\nu - \partial_\nu \hat{W}_\mu - g\hat{W}_\mu \times \hat{W}_\mu \tag{2.13}$$

corresponding to the kinetic energy and self coupling of the W_μ fields and the kinetic energy term of the B_μ field.

None of these gauge bosons are physical particles, and instead linear combinations of these gauge bosons make up γ and the W and Z bosons, defined as

$$W^{\pm} = \frac{1}{\sqrt{2}}\left(W_\mu^1 \mp iW_\mu^2\right), \qquad \begin{pmatrix} Z_\mu \\ A_\mu \end{pmatrix} = \begin{pmatrix} cos\theta_W & -sin\theta_W \\ sin\theta_W & cos\theta_W \end{pmatrix} \begin{pmatrix} W_\mu^3 \\ B_\mu \end{pmatrix}, \tag{2.14}$$

where the mixing angle, $\theta_w = \tan^{-1}\frac{g'}{g}$, relates the coupling of the neutral weak and electromagnetic interactions.

As in the case of the formulation of the QED Lagrangian there remains no mass term for the photon. However this is also the case for the W, Z and fermions in the Lagrangian, contrary to experimental measurement. Any explicit introduction of mass terms would break the symmetry of the Lagrangian and instead mass terms can be introduced through spontaneous breaking of the EWK symmetry via the Higgs mechanism.

The Higgs mechanism induces spontaneous symmetry breaking through the introduction of a complex scalar SU(2) doublet field ϕ which attains a non-zero Vacuum Expectation Value (VEV) [17][18][19][20].

$$\phi = \begin{pmatrix} \phi^+ \\ \phi^0 \end{pmatrix} \qquad with \qquad \begin{array}{l} \phi^+ \equiv (\phi_1 + i\phi_2)/\sqrt{2} \\ \phi^0 \equiv (\phi_3 + i\phi_4)/\sqrt{2} \end{array} \tag{2.15}$$

The Lagrangian defined in Equation (2.11) attains an additional term $\mathcal{L}_{Higgs}$ of the form

$$\begin{aligned} \mathcal{L}_{Higgs} &= \overbrace{(D_\mu\phi)^\dagger(D^\mu\phi)}^{\text{kinetic}} - \overbrace{\mu^2\phi^\dagger\phi - \lambda(\phi^\dagger\phi)^2}^{\text{potential V}(\phi)} \qquad (\mu^2, \lambda) > 0 \in \mathbb{R}, \\ \mathcal{L}_{SM} &= \mathcal{L}_{EWK} + \mathcal{L}_{Higgs}, \end{aligned} \tag{2.16}$$

where the covariant derivative D_μ is that defined in Equation (2.10). The last two terms of $\mathcal{L}_{Higgs}$ correspond to the Higgs potential, in which real positive values of μ^2 and λ are required to ensure the generation of masses for the bosons and leptons. The minimum of this potential is found at $\phi^\dagger\phi = \frac{1}{2}(\phi_1^2 + \phi_2^2 + \phi_3^2 + \phi_4^2) = \mu^2/\lambda = v^2$, where v represents the VEV.

Defining the ground state of the ϕ field to be consistent with the $V(\phi)$ minimum, and then expanding around a ground state chosen to maintain an unbroken electromagnetic symmetry thus preserving a zero photon mass [21] leads to

$$\phi_0 = \sqrt{\frac{1}{2}}\begin{pmatrix} 0 \\ v \end{pmatrix}, \qquad \phi(x) = e^{i\tau\cdot\theta(x)/v}\sqrt{\frac{1}{2}}\begin{pmatrix} 0 \\ v + h(x) \end{pmatrix}, \tag{2.17}$$

where the fluctuations from the vacuum ϕ_0 are parametrized in terms of four real fields, $\theta_1, \theta_2, \theta_3$ and $h(x)$.

Choosing to gauge away the three massless Goldstone boson fields by setting $\theta(x)$ to zero and substituting $\phi(x)$ back into kinetic term of $\mathcal{L}_{Higgs}$ from Equation (2.16) leads to mass terms for the $W^\pm$ and Z bosons

$$(D_\mu\phi)^\dagger(D^\mu\phi) = \frac{1}{2}(\partial_\mu h)^2 + \frac{g^2v^2}{2}W_\mu^+W^{-\mu} + \frac{v^2g^2}{8\cos^2\theta_w}Z_\mu Z^\mu + 0A_\mu A^\mu, \tag{2.18}$$

where the relations between the physical and electroweak gauge fields from Equation (2.14) are used. The $W^\pm$ and Z boson masses can then be determined to be

$$M_W = \frac{1}{2}gv \qquad M_Z = \frac{1}{2}\frac{gv}{\cos\theta_w}. \tag{2.19}$$

This mechanism is also used to generate fermion masses by introducing a Yukawa coupling between the fermions and the ϕ field [22], with the coupling strength of a particle to the ϕ field governing its mass. Additionally a scalar boson h with mass $m_h = v\sqrt{\frac{\lambda}{2}}$, is also predicted as a result of this spontaneous symmetry breaking and became known as the Higgs boson. Its discovery by the CMS and ATLAS experiments in 2012 is the first direct evidence to support this method of mass generation within the SM.

2.2. Motivation for Physics Beyond the Standard Model

As has been described, the SM has proven to be a very successful theory, predicting the existence of the $W^{\pm}$ and Z bosons and the top quark long before they were experimentally observed. However the theory does not accurately describe all observed phenomena and has some fundamental theoretical flaws that hint at the need for additional extensions to the current theory.

On a theoretical level, the SM is unable to incorporate the gravitational interactions of fundamental particles within the theory. Whilst at the electroweak energy scales the relative strength of gravity is negligible compared to the other three fundamental forces, at much higher energy scales, $\mathrm{M_{planck}} \sim 10^{18}\mathrm{GeV}$, quantum gravitational effects become increasingly dominant. The failure to reconcile gravity within the SM, demonstrates that the SM must become invalid at some higher energy scale.

Other deficiencies with the SM include the fact that the predicted rate of Charge-Parity violation does not account for the matter dominated universe which we inhabit, and that the SM prediction of a massless neutrino conflicts with the observation of neutrino flavour mixing, attributed to mixing between neutrino mass eigenstates [23][24].

Perhaps one of the most glaring gaps in the predictive power of the SM is that there exists no candidate to explain the cosmic dark matter observed in galactic structures through indirect techniques including gravitational lensing and measurement of the orbital velocity of stars at galactic edges. Any such candidate must be very weakly interacting but must also be stable, owing to the lack of direct detection of the decay products of such an process. Therefore a stable dark matter candidate, is one of the main obstacles to address for any Beyond Standard Model (BSM) physics model.

The recent discovery of the Higgs boson whilst a significant victory for the predictive power of the SM, brings with it still unresolved questions. This issue is commonly described as the "hierarchy problem".

In the absence of new physics between the TeV and Planck scale, calculating beyond tree-level contributions to the Higgs mass term given by its self interaction, result in divergent terms that push the Higgs mass up to the planck mass M_{planck}.

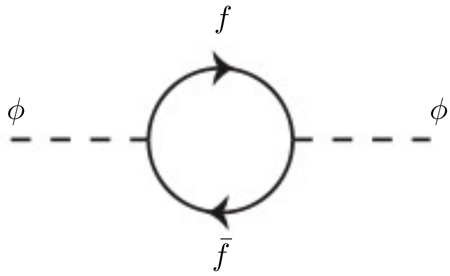

Figure 2.1.: One loop quantum corrections to the Higgs squared mass parameter m_h^2 due to a fermion.

This can be demonstrated by considering the one loop quantum correction to the Higgs mass with a fermion f, shown in Figure 2.1 with mass m_f. The Higgs field couples to f with a term in the Lagrangian $-\lambda_f h\bar{f}f$, yielding a correction of the form [25],

$$\delta m_h^2 = -\frac{|\lambda_f|^2}{8\pi^2}\Lambda^2 + .., \tag{2.20}$$

where λ_f represents the coupling strength for each type of fermion $\propto m_f$, and Λ the cutoff energy scale at which the SM ceases to be a valid theory.

To recover the mass of the now discovered Higgs boson would require a fine-tuning of the parameters to cancel out these mass corrections of the Higgs mass to the scale of 30 orders of magnitude. This appears as an unnatural solution to physicists and it is this hierarchy problem that provides one of the strongest motivations for the theory of SUperSYmmetry (SUSY).

2.3. Supersymmmetry Overview

Supersymmetry provides potential solutions to many of the issues raised in the previous section. It provides a dark matter candidate, can explain baryogenesis in the early universe and also provides an elegant solution to the hierarchy problem [26][27][28][29]. At it's heart it represents a new space-time symmetry that relates fermions and bosons. This symmetry converts bosonic states into fermionic states, and vice versa, see Equation (2.21) ,

$$Q|\text{Boson}\rangle = |\text{Fermion}\rangle \qquad Q|\text{Fermion}\rangle = |\text{Boson}\rangle, \tag{2.21}$$

where the operator Q is the generator of these transformations. Quantum field theories which are invariant under such transformations are called supersymmetric.

This symmetry operator therefore acts upon a particles spin altering it by a half integer value. The consequences of the application of this additional space-time symmetry introduce a new rich phenomenology. For example in supersymmetric theories, both the left handed SU(2) doublet and right handed singlet of fermions will have a spin-0 superpartner, containing the same electric charge, weak isospin, and colour as its SM partner. In the case of leptons $(\nu_l, l)_L$, they will have two superpartners, a sneutrino $\widetilde{\nu}_{lL}$ and a slepton $\widetilde{l}_L$, whilst the singlet l_R also has a superpartner slepton $\widetilde{l}_R$.

Each particle in a supersymmetric theory is paired together with their superpartners as a result of these supersymmetric transformations in a so called supermultiplet. These superpartners will then consequently also contribute to the corrections to the Higgs mass. Bosonic and fermionic loops contributing to the correction appear with opposite signs, and therefore cancellation of these divergent terms will stabilise the Higgs mass, solving the hierarchy problem [30][31].

One of the simplest forms of SUSY, is to simply have a set of SM supersymmetric partners with the same mass and interactions as their counterparts. However the current lack of any experimental evidence for that predicted sparticle spectrum implies SUSY must be a broken symmetry in which any sparticle masses must be greater than their SM counterparts.

There exist many techniques which can induce supersymmetric breaking [32][33][34]. Of particular interest to experimental physicists are those at which the breaking scale is of an order that is experimentally accessible to the LHC i.e. $\sim$ TeV scale. Whilst there is no requirement for supersymmetric breaking to occur at this energy scale, for supersymmetry to provide a solution to the hierarchy problem, it is necessary for this scale to not differ too drastically from the EWK scale [35][36].

2.3.1. R-Parity

Some supersymmetric theories also present a solution to the dark matter problem. These theories contain a Lightest Supersymmetric Partner (LSP), which matches the criteria of a Weakly Interacting Massive Particle (WIMP) required by cosmological observation when R-parity is conserved.

Baryon (B) and Lepton (L) number conservation is forbidden in the SM by renormalisability requirements. The violation of Baryon or Lepton number results in a proton lifetime much shorter than those set by experimental limits [37]. Another symmetry called R-parity is then often introduced to SUSY theories to maintain baryon and lepton conservation.

R-parity is described by the equation

$$R_P = (-1)^{3(B-L)+2s}, \tag{2.22}$$

where s represents the spin of the particles. $B = \pm\frac{1}{3}$ for quarks/antiquarks and $B = 0$ for all others, $L = \pm 1$ for leptons/antileptons, $L = 0$ for all others.

R-parity ensures the stability of the proton in SUSY models, and also has other consequences for the production and decay of supersymmetric particles. In particle colliders supersymmetric particles can only be pair produced, and similarly the decay of any produced supersymmetric particle is restricted to a SM particle and a lighter supersymmetric particle as allowed by conservation laws. A further implication of R-parity is that once a supersymmetric particle has decayed to the LSP it remains stable, unable to decay into a SM particle.

A LSP will not interact in a detector at a particle collider, leaving behind a missing energy $\not{E}_T$ signature. The assumption of R-parity and its consequences are used to determine the physical motivation and search strategies for SUSY models at the LHC.

2.4. Experimental Signatures of SUSY at the LHC

Should strongly interacting sparticles be within the experimental reach of the LHC, then it is expected that they can be produced in a variety of ways :

- squark/anti-squark and gluino pairs can be produced via both gluon fusion and quark/anti-quark scattering,
- a gluino and squark produced together via quark-gluon scattering,
- squark pairs produced via quark-quark scattering.

Whilst most SUSY searches invoke the requirement of R-parity to explore parameter phase space, there still exist a whole plethora of possible SUSY model topologies which could be waiting to be discovered at the LHC.

During the 2011 run period at $\sqrt{s} = 7$ TeV, particular models were used to benchmark performance and experimental reach of both CMS searches and previous experiments. The Compressed Minimal SuperSymmetric Model (CMSSM) was initially chosen for a number of reasons [38], one of the most compelling being the reduction of the up to 105 new parameters that can be introduced by SUSY (in addition to the existing 19 of the SM), to just 5 free extra free parameters. It was this simplicity, combined with the theory not requiring any fine tuning of particle masses to produce experimentally verified SM observables that made it an attractive model to interpret physics results.

However recent results from the LHC now strongly disfavour large swathes of CMSSM parameter space [39][40][41]. In the face of such results a more pragmatic model independent search strategy is now applied across most SUSY searches at the LHC, see Section (2.4.1).

As previously stated, a stable LSP that exhibits the properties of a dark matter candidate would be weakly interacting and therefore will not be directly detected in a detector environment. Additionally the cascade decays of supersymmetric particles to this LSP state would also result in significant hadronic activity. These signatures will then be characterised through large amounts of hadronic jets (see Section (3.3.1)), leptons and a significant amount of missing energy dependent upon the size of the mass splitting between the LSP and the supersymmetric particle it has decayed from.

The SM contains processes which can exhibit a similar event topology to that described above. The largest contribution coming from the general QCD environment of a hadron collider. A multitude of different analytical techniques are used by experimental physicists to reduce or estimate any reducible or irreducible backgrounds, allowing a possible SUSY signature to be extracted. The techniques employed within this thesis are described in great detail within Section (4.1).

2.4.1. Simplified models

With such a variety of different ways for a SUSY signal to manifest itself, it is necessary to be able to interpret experimental reach through the masses of gluinos and squarks which can be excluded by experimental searches rather than on a model specific basis.

This is accomplished through SMS models, which are defined by a set of hypothetical particles and a sequence of their production and decay modes [42][43]. In the SMS models considered within this thesis, only the production process for the two primary particles are considered. Each primary particle can undergo a direct or a cascade decay through an intermediate new particle. At the end of each decay chain there remains a neutral, undetected LSP particle, denoted $\widetilde{\chi}_{LSP}$ which can represent a neutralino or gravitino. Essentially it is easier to consider each SMS with branching ratios set to 100%. The masses of the primary particle and the LSP remain as free parameters, in which the absolute value and relative difference between the primary and LSP particle alter the kinematics of the event.

Different SMS models are denoted with a T-prefix, with a summary of the types interpreted within this thesis listed below [44].

- **T1,T1xxxx**, models represent a simplified version of gluino pair production with each gluino (superpartner to the gluon) undergoing a three-body decay to a quark-antiquark pair and the LSP (i.e. $\widetilde{g} \rightarrow q\bar{q}\widetilde{\chi}_{LSP}$). The resultant final state from this decay is typically 4 jets + $\not{E}_T$ in the absence of initial/final state radiation and detector effects. xxxx denotes models in which the quarks are of a specific flavour, typically t or b quark-antiquarks.

- **T2,T2xx**, models represent a simplified version of squark anti-squark production with each squark undergoing a two-body decay into a light-flavour quark and LSP (i.e. $\widetilde{q} \rightarrow q\widetilde{\chi}_{LSP}$). This results in final states with less jets than gluino mediated production, typically 2 jets + $\not{E}_T$ when again ignoring the effect of initial/final state radiation and detector effects. xx models represent decays in which both the quark and the squark within the decay is of a specific flavour, which in this thesis are again $\widetilde{t}$/t or $\widetilde{b}$/b.

Models rich in b and t quarks are interpreted within this thesis as they remain of particular interest within "Natural SUSY" scenarios [45][46]. The largest contribution to the quadratic divergence in the Higgs mass parameter comes from a loop of top quarks via the Yukawa coupling. Cancellation of these divergences can be achieved in supersymmetric theories by requiring a light right handed top squark, $\widetilde{t}_R$, and left-handed double $SU(2)_L$ doublet containing top and bottom squarks, $(\frac{\tilde{t}}{\tilde{b}})_L$ [47].

These theories therefore solve the hierarchy problem by predicting light $\sim$ EWK scale third generation sleptons, to be accessible at the LHC. Search strategies involving the requirement of b-tagging (see Section (3.3.2)) are used to give sensitivity to these type of SUSY scenarios and are discussed in greater detail within Chapter 4.

Two example decay chains are shown in Figure 2.2; the pair production of gluinos (`T1`) and the pair production of squarks (`T2`) decaying into SM particles and LSP's.

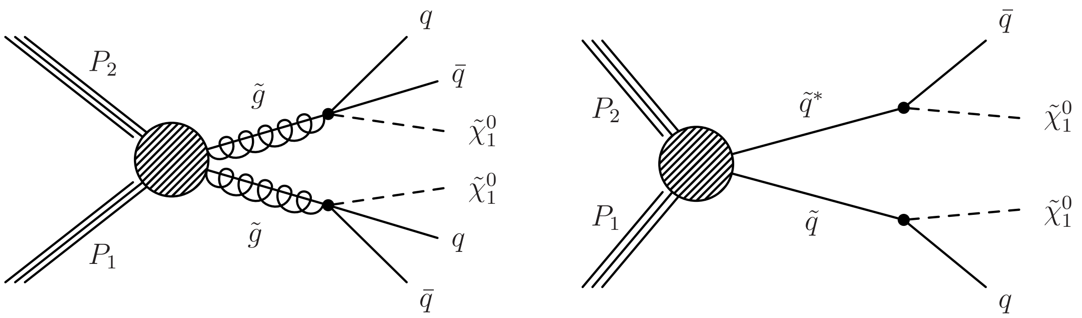

Figure 2.2.: Two example SMS model decays (`T1` (left),`T2` (right)), which are used in interpretations of physics reach by CMS.

Chapter 3.

The LHC And The CMS Detector

Probing the SM for signs of new physics would not be possible without the immensely complex electronics and machinery that makes the TeV energy scale accessible to physicists for the first time. This chapter will introduce both the LHC based at European Organization for Nuclear Research (CERN) and the Compact Muon Solenoid (CMS) detector (of which the author is a member). Section (3.2) serves to present an overview of the different components of the CMS detector, with specific components relevant to the search for supersymmetric particles described in greater detail. Section (3.3) will focus on event and object reconstruction again with more emphasis on jet level quantities which are most relevant to the author's analysis research. Finally Section (3.4) will describe and detail the service work for the CMS Collaboration performed by the author, in measuring the performance of L1 single jet triggers in the Global Calorimeter Trigger (GCT) during the 2012-2013 run period.

3.1. The LHC

The LHC is a storage ring, accelerator, and collider of circulating beams of protons or ions. Housed in the tunnel dug for Large Electron-Positron Collidor (LEP), it is approximately 27 km in circumference, 100 m underground, and straddles the border between France and Switzerland outside of Geneva. It is currently the only collider in operation that is able to study physics at the TeV scale. A double-ring circular synchrotron, it was designed to collide both proton-proton (pp) and heavy ion (PbPb) with a centre of mass energy $\sqrt{s} = 14$ TeV at a final design luminosity of $10^{34}\text{cm}^{-2}\text{s}^{-1}$.

These counter-circulating beams of protons or Pb ions are merged in four sections around the ring to enable collisions of the beams, with each interaction point being home to one of the four major experiments; A Large Ion Collider Experiment (ALICE) [48] , A Toroidal LHC ApparatuS (ATLAS) [49], Compact Muon Solenoid (CMS) [50] and Large Hadron Collider Beauty (LHCb) [51] which record the resultant collisions. The layout of the LHC ring is shown in Figure 3.1. The remaining four sections contain acceleration, collimation and beam dump systems. In the eight arc sections, the beams are steered by magnetic fields of up to 8 T provided by super conduction dipole magnets, which are maintained at temperatures of 2 K using superfluid helium. Additional magnets for focusing and corrections are also present in straight sections within the arcs and near the interaction regions where the detectors are situated.

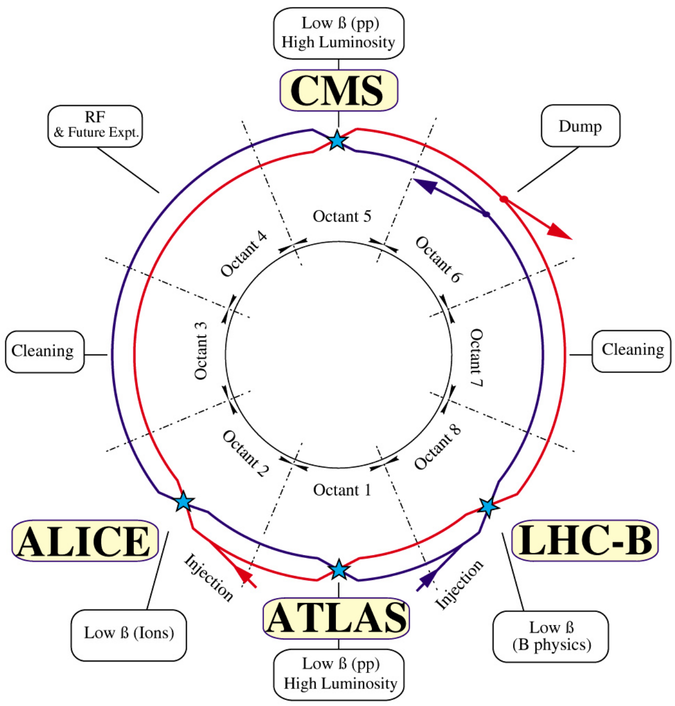

Figure 3.1.: A top down layout of the LHC. [52], with the position of the four main detectors labelled.

Proton beams are formed inside the Proton Synchrotron (PS) from bunches of protons 50 ns apart with an energy of 26 GeV. The protons are then accelerated in the Super Proton Synchrotron (SPS) to 450 GeV before being injected into the LHC. These LHC proton beams consists of many “bunches” (i.e. approximately 1.1×10^{11} protons localised into less than 1 ns in the direction of motion). Before collision, the beams are ramped to

4 TeV (2012) per beam in a process involving increasing the current passing through the dipole magnets. Once the desired $\sqrt{s}$ energy is reached then the beams are allowed to collide at the interaction points. The luminosity falls regularly as the run progresses as protons are lost in collisions, and eventually the beam is dumped before repeating the process again.

Colliding the beams produced an instantaneous luminosity of approximately 5×10^{33} $\text{cm}^{-2}\text{s}^{-1}$ during the 2012 run. The high number of protons in each bunch increases the likelihood of multiple interactions with each crossing of the counter-circulating beams. This leads to isotropic energy depositions within the detectors positioned at these interaction points, increasing the energy scale of the underlying event. This is known as pile-up and the counteracting of it's effects are important to the many measurements performed at the LHC.

In the early phase of prolonged operation after the initial shutdown the machine operated in 2010-2011 at 3.5 TeV per beam, $\sqrt{s} = 7$ TeV, delivering 6.13 fb^{-1} of data [53]. During the 2012-2013 run period, data was collected at an increased $\sqrt{s} = 8$ TeV improving the sensitivity of searches for new physics. Over the whole run period 23.3 fb^{-1} of data was delivered, of which 21.8 fb^{-1} was recorded by the CMS detector as shown in Figure 3.2 [53]. A total of 12 fb^{-1} of 8 TeV certified data was collected by October 2012, and it is this data which forms the basis of the results presented within this thesis.

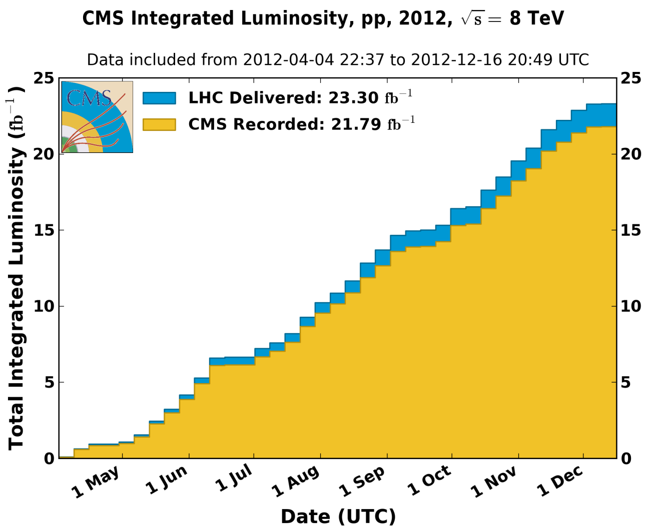

Figure 3.2.: The total integrated luminosity delivered to and collected by CMS during the 2012 8 TeV *pp* runs.

3.2. The CMS Detector

The Compact Muon Solenoid (CMS) detector is one of two general purpose detectors at the LHC designed to search for new physics. The detector is designed to provide efficient identification and measurement of many physics objects including photons, electrons, muons, taus, and hadronic showers over wide ranges of transverse momentum and direction. It's nearly 4π coverage in solid angle allows for accurate measurement of global transverse momentum imbalance. These design factors give CMS the ability to search for direct production of SUSY particles at the TeV scale, making the search for Supersymmetric particles one of the highest priorities among the wide range of physics programmes at CMS.

CMS uses a right-handed Cartesian coordinate system with the origin at the interaction point and the z-axis pointing along the beam axis, the x-axis points radially inwards to the centre of the collider ring, with the y-axis points vertically upward. The azimuthal angle, ϕ ranging between $[-\pi,\pi]$ is defined in the x-y plane starting from the x-axis. The polar angle θ is measured from the z axis. The common convention in particle physics is to express an out going particle in terms of ϕ and its pseudorapidity defined as

$$\eta = -\log\tan\left(\frac{\theta}{2}\right). \tag{3.1}$$

The variable $\Delta R = \sqrt{\Delta\phi^2 + \Delta\eta^2}$ is commonly used to define angular distance between objects within the detector and additionally energy and momentum is typically measured in the transverse plane perpendicular to the beam line. These values are calculated from the x and y components of the object and are denoted as $E_T = E\sin\theta$ and $p_T = \sqrt{p_x^2 + p_y^2}$.

3.2.1. Detector subsystems

As the range of particles produced from pp collisions interact in different ways with matter, CMS is divided into sub-detector systems, which perform complementary roles to identify the identity, mass, and momentum of the different physics objects present in each event. These detector sub-systems contained within CMS are wrapped in layers around a central 13 m long 4 T super conducting solenoid as shown in Figure 3.3. With the endcaps closed, CMS is a cylinder of length 22 m, diameter 15 m, and mass 12.5 kilotons. A more detailed complete description of the detector can be found elsewhere[50].

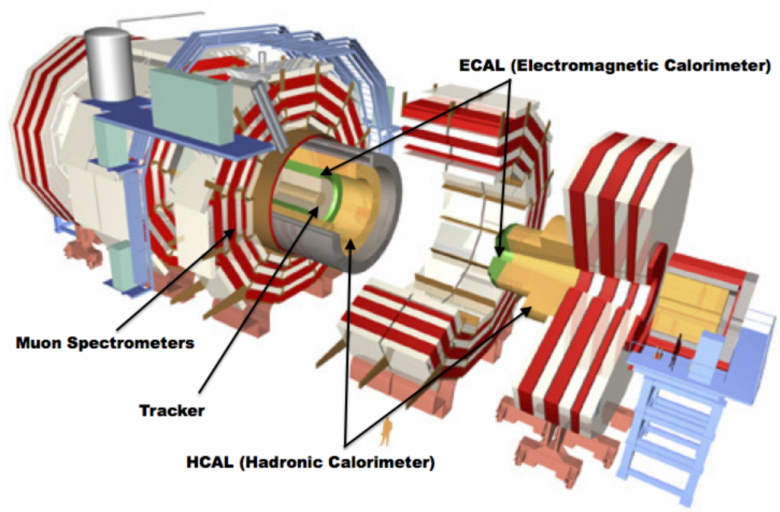

Figure 3.3.: A pictorial depiction of the CMS detector with the main detector subsystems labelled. [54]

3.2.2. Tracker

The inner-most sub-detector of the barrel is the multi-layer silicon tracker, formed of a pixel detector component encased by layers of silicon strip detectors. The pixel detector consists of three layers of silicon pixel sensors providing measurements of the momentum, position coordinates of the charged particles as they pass, and the location of primary and secondary vertices between 4 cm and 10 cm transverse to the beam. Outside the pixel detector, ten cylindrical layers of silicon strip detectors extend the tracking system out to a radius of 1.20 m from the beam line. The tracking system provides efficient and precise determination of the charges, momenta, and impact parameters of charged particles with the geometry of the tracker extending to cover a rapidity range up to $|\eta|<$ 2.5.

The tracking system also plays a crucial part in the identification of jets that originate from b-quarks through the measurement of displaced secondary vertices. The methods in which these b-flavoured jets are identified are discussed within Section (3.3.2). The identification of b-jets is important in many searches for natural SUSY models and forms an important part of the inclusive search strategy described within Section (4.2).

3.2.3. Electromagnetic calorimeter

Immediately outside of the tracker, but still within the magnet core, sits the Electromagnetic CALorimeter (ECAL). Covering a pseudorapidity up to $|\eta| < 3$ and compromising of over 75 $\times 10^3$ $PbWO_4$ (lead tungstate) crystals that scintillate as particles deposit energy, the ECAL provides high resolution measurements of the electromagnetic showers from photons and electrons in the detector.

Lead tungstate is used because of its short radiation length ($X_0 \sim 0.9$ cm) and small Molieré radius (~ 2.1 cm) leading to high granularity and resolution. It's fast scintillation time (~ 25 ns) reduces the effects of pile-up, which occurs when energy from previous collisions are still being read out, and its radiation hardness gives it longevity. The crystals are arranged in modules which surround the beam line in a non-projective geometry, angled at $3°$ with respect to the interaction point to minimise the risk of particles escaping down the cracks between the crystals.

The ECAL is primarily composed of two sections, the Electromagnetic CALorimeter Barrel (EB) which extends in pseudo-rapidity to $|\eta| < 1.479$ with a crystal front cross section of 22×22 mm and a length of 230 mm corresponding to 25.8 radiation lengths, and the Electromagnetic CALorimeter Endcap (EE) covering a rapidity range of $1.479 < |\eta| < 3.0$, which consists of two identical detectors on either side of the EB. A lead-silicon sampling 'pre-shower' detector Electromagnetic CALorimeter pre-Shower (ES) is placed before the endcaps to aid in the identification of neutral pions. Their arrangement is shown in Figure 3.4.

Scintillation photons from the lead tungstate crystals are instrumented with Avalanche Photo-Diodes (APD) and Vacuum Photo-Triodes (VPT) located in the EB and EE respectively, converting the scintillating light into an electric signal which is consequently used to determine the amount of energy deposited within the crystal . These instruments are chosen for their resistance under operation to the strong magnetic field of CMS. The scintillation of the ECAL crystals as well as the response of the APDs varies as a function

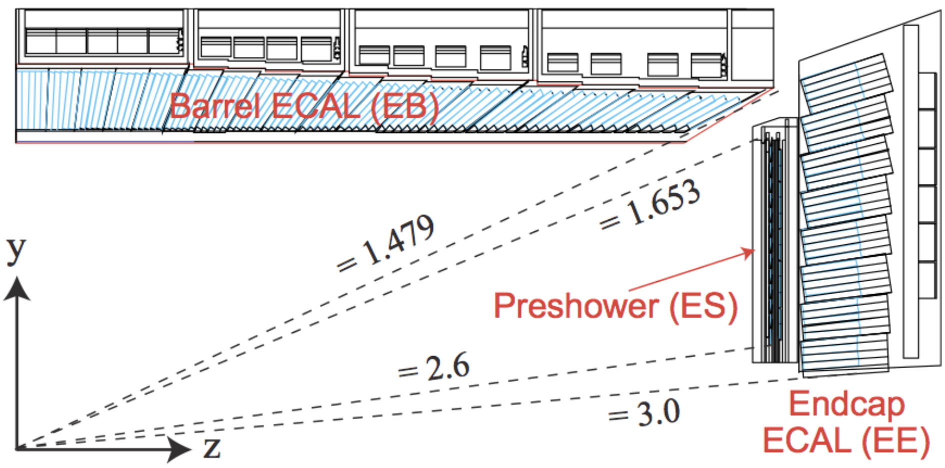

Figure 3.4.: Illustration of the CMS ECAL showing the arrangement of the lead tungstate crystals in the EB and EE. The ES is also shown and is located in front of the EE [55].

of temperature and so cooling systems continually maintain an overall constant ECAL temperature $\pm 0.05°C$.

3.2.4. Hadronic calorimeter

Beyond the ECAL lies the Hadronic CALorimeter (HCAL) which is responsible for the accurate measurement of hadronic showers, crucial for analyses involving jets or missing energy signatures. The HCAL is a sampling calorimeter which consists of alternating layers of brass absorber and plastic scintillator, except in the hadron forward $(3.0 < |\eta| < 5.0)$ region in which steel absorbers and quartz fibre scintillators are used because of their increased radiation tolerance. Hadron showers are initiated in the absorber layers inducing scintillation in the plastic scintillator tiles. These scintillation photons are converted by wavelength shifting fibres for read-out by hybrid photodiodes.

The HCAL's size is constrained to a compact size by the presence of the solenoid, requiring the placement of an additional outer calorimeter on the outside of the solenoid to increase the sampling depth of the HCAL. A schematic of the HCAL can be seen in Figure 3.5.

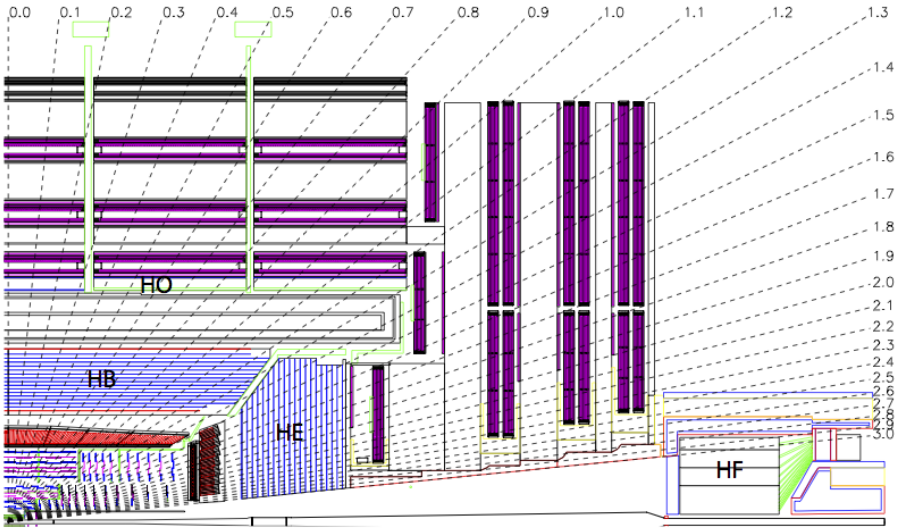

Figure 3.5.: Schematic of the hadron calorimeters in the r-z plane, showing the locations of the HCAL components and the HF. [50].

The HCAL covers the range $|\eta| < 5$ and consists of four sub-detectors: the Hadron Barrel (HB) $|\eta| < 1.3$, the Hadron Outer (HO), the Hadron Endcaps (HE) $1.3 < |\eta| < 3.0$ and the Hadron Forward (HF). The HB, contained between the outer edge of the ECAL and the inner edge of the solenoid is formed of 36 azimuthal wedges which are split between two half-barrel segments. Each wedge is segmented into four azimuthal angle (ϕ) sectors, and each half-barrel is further segmented into 16 η towers. The electronic readout chain, channels the light from the active scintillator layers from one ϕ-segment and all η-towers of a half-barrel to a Hybrid Photo Diode (HPD).

The relatively short number of interaction lengths (λ_l, the distance a hadron will travel through the absorber material before it has lost $\frac{1}{e}$ of its energy) within the HB, the lowest being $\lambda_l = 5.82$ at $|\eta| = 0$, facilitates the need for the 'tail catching' HO to increase the sampling depth in the central barrel rapidity region $|\eta| < 1.3$ to 11 interaction lengths . Significant fractions of the hadrons energy will be deposited in the ECAL as it passed through the detector. Therefore measurements of hadron energies in the central regions $|\eta| < 3.0$ use both the ECAL and HCAL to reconstruct the true energy from showering hadrons.

3.2.5. Muon systems

Muons being too massive to radiate away energy via Bremsstrahlung, interact little in the calorimeters and mostly pass through the detector until they reach the system of muon detectors which forms the outer most part of the CMS detector.

Outside of the superconducting solenoid are four muon detection layers interleaved with the iron return yokes which measure the muons energy via ionisation of gas within detector elements. Three types of gaseous chamber are used. The Drift Tube (DT), Cathode Stripe Chamber (CSC), and Resistive Plate Chamber (RPC) systems provide efficient detection of muons with pseudo-rapidity $|\eta| < 2.4$. The best reconstruction performance is obtained when the muon chamber is combined with the inner tracking information to determine muon trajectories and their momenta [56].

3.3. Event Reconstruction and Object Definition

The goal of event reconstruction is to take the raw information recorded by the detector and to compute from it higher-level quantities which can be used at an analysis level. These typically correspond to an individual particle's energy and momenta, or groups of particles which shower in a narrow cone and the overall global energy and momentum balance of the event. The reconstruction of these objects are described in great detail in [57], however covered below are brief descriptions of those which are most relevant to the analysis detailed in Chapter 4.

3.3.1. Jets

Quarks and gluons are produced copiously at the LHC in the hard scattering of partons. As these quarks and gluons fragment, they hadronize and decay into a group of strongly interactive particles and their decay products. These streams of particles travel in the same direction, as they have been "boosted" by the momentum of the primary hadron. These collections of decay products are reconstructed and identified together as a "jet".

At CMS jets are reconstructed from energy deposits in the detector using the anti-kt algorithm [58] with size parameter $\Delta R = 0.5$. The anti-kt jet algorithm clusters jets by defining a distance between hard (high p_T) and soft (low p_T) particles such that soft particles are preferentially clustered with hard particles before being clustered between themselves. This produces jets which are robust to soft particle radiation from the pile-up conditions produced by the LHC.

There are two main type of jet reconstruction used at CMS, Calorimeter (Calo) and Particle Flow (PF) jets [59]. Calorimeter jets are reconstructed using both the ECAL and HCAL cells, combined into calorimeter towers . These calorimeter towers consist of geometrically matched HCAL cells and ECAL crystals. Electronics noise is suppressed by applying a threshold to the calorimeter cells, with pile-up effects reduced by a requirement placed on the tower energy [60]. Calorimeter jets are the jets used within the analysis presented in this thesis.

PF jets are formed from combining information from all of the CMS sub-detectors systems to determine which final state particles are present in the event. Generally, any particle is expected to produce some combination of a track in the silicon tracker, a deposit in the calorimeters, or a track in the muon system. The PF jet momentum and spatial resolutions are greatly improved with respect to calorimeter jets, as the use of the tracking detectors and of the high granularity of ECAL allows resolution and measurement of charged hadrons and photons inside a jet, which together constitute $\sim$ 85% of the jet energy [61].

The jets reconstructed by the clustering algorithm in CMS typically have an energy that differs to the 'true' energy measured by a perfect detector. This stems from the non-linear and nonuniform response of the calorimeters as well as other residual effects including pile-up and underlying events, and therefore additional corrections are applied to recover a uniform relative response as a function of pseudo-rapidity. These are applied as separate sub corrections [62].

- A pile-up correction is first applied to the jet. It subtracts the average extra energy deposited in the jet that comes from other vertices present in the event and is therefore not part of the hard jet itself.
- p_T and η dependant corrections derived from Monte Carlo simulations are used to account for the non-uniform response of the detector.
- p_T and η residual corrections are applied to data only to correct for difference between data and Monte Carlo. The residual is derived from QCD di-jet samples and the p_T residual from $\gamma+$ jet and $Z+$ jets samples in data.

3.3.2. B-tagging

The decays of b quarks are suppressed by small CKM matrix elements. As a result, the lifetimes of b-flavoured hadrons, produced in the fragmentation of b quarks, are relatively long; $\mathcal{O}$ 1ps. The identification of jets originating from b quarks is very important for searches for new physics and for measurements of SM processes.

Many different algorithms developed by CMS select b-quark jets based on variables such as the impact parameters of the charged-particle tracks, the properties of reconstructed decay vertices, and the presence or absence of a lepton, or combinations thereof [63]. One of the most efficient of which is the Combined Secondary Vertex (CSV) which operates based on secondary vertex and track-based lifetime information, benchmarked in 'Loose', 'Medium' and 'Tight' working points, of which the medium point is the tagger used within the α_T search presented in Section (4.1). All figures within this sub-section, demonstrating the performance of this b-tagging algorithm are taken from [64].

Using the CSV tagger, a likelihood-based discriminator distinguishes between jets from b-quarks, and those from charm or light quarks and gluons, which is shown in Figure 3.6. The minimum thresholds on the discriminator for each working point correspond to the mis-identication probability for light-parton jets of 10%, 1%, and 0.1%, respectively, in jets with an average p_T of about 80 GeV.

The b-tagging performance is evaluated to measure the b-jet tagging efficiency ϵ_b, and the misidentification probability of charm ϵ_c and light-parton jets ϵ_s. The tagging efficiencies for each of these three jet flavours are compared between data and MC simulation, from which a series of p_T and $|\eta|$ binned jet corrections are determined,

$$SF_{b,c,s} = \frac{\epsilon_{b,c,s}^{data}}{\epsilon_{b,c,s}^{MC}}. \tag{3.2}$$

These are collectively named 'Btag Scale Factors' and allow MC simulation to accurately reflect the running conditions and performance of the tagging algorithm in data. Understanding of the b-tagging efficiency is essential in order to minimise systematic uncertainties in physics analyses that employ b-tagging.

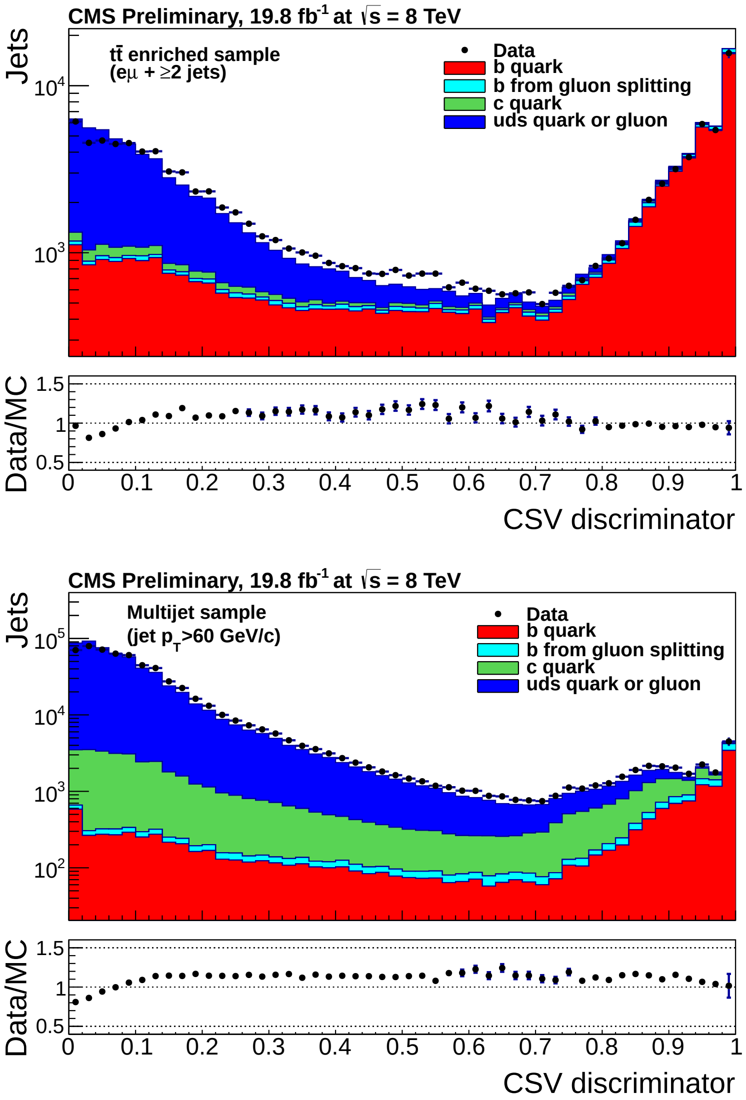

Figure 3.6.: CSValgorithm discriminator values in enriched ttbar (top) and inclusive multi jet samples (bottom) for b,c and light flavoured jets. The discriminator value used for each working points are determined from the misidentification probability for light-parton jets to be tagged as a b-jet, which are given as 0.244 (10%), 0.679 (1%) and 0.898 (0.1%) for the L, M and T working points respectively.

The b-tagging efficiency is measured in data using several methods applied to multi jet events, primarily based on a sample of jets enriched in heavy flavour content. One method requires the collection of events with a soft muon within a cone $\Delta R < 0.4$ around the jet axis. Because the semi-leptonic branching fraction of b hadrons is significantly larger than that for other hadrons, these jets are more likely to arise from b quarks than from another flavour, with the resultant momentum component of the muon transverse to the jet axis larger for muons from b-hadron decays than from light or charm jets.

Additionally the performance of the tagger can also be benchmarked in $t\bar{t}$ events where in the SM, the top quark is expected to decay to a W boson and a b quark about 99.8% of the time [1]. Further selection criteria is applied to these events to further enrich the b quark content of these events. The methods to identify b-jets in data are discussed in great detail at [65]. The jet flavours are determined in simulation using truth level information and are compared to data to determine the correction scale factors (SF_b), which are displayed for the CSVM tagger in Figure 3.7.

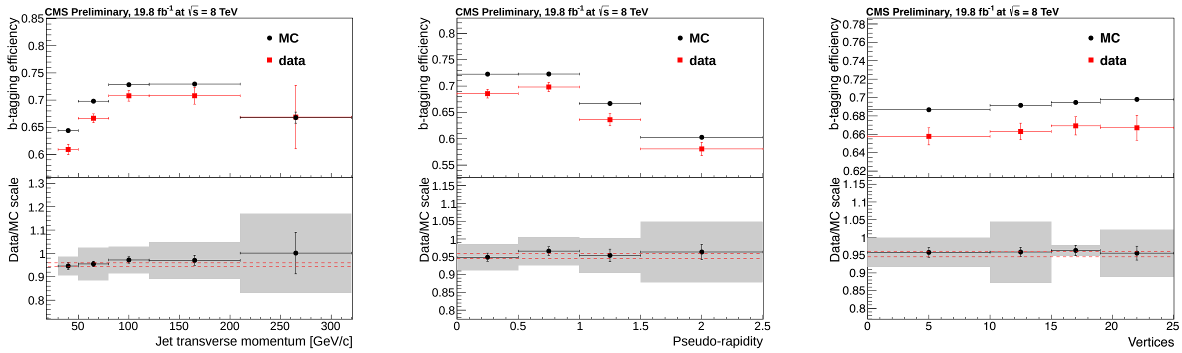

Figure 3.7.: Measured in $t\bar{t} \rightarrow$ di-lepton events using the CSVM tagger: (upper panels) b-tagging efficiencies and (lower panels) data/MC scale factor SF_b as a function of (left) jet p_T, (middle) jet $|\eta|$ and (right) number of primary vertices. In the lower panels, the grey filled areas represent the total statistical and systematic uncertainties, whereas the dotted lines are the average SF_b values within statistical uncertainties.

The measurement of the misidentication probability for light-parton jets relies on the inversion of tagging algorithms, selecting non-b jets using the same variables and techniques used in benchmarking the b-tagging efficiency. The scale factors (SF_s) to be applied to MC are shown in Figure 3.8 for the CSVM tagger.

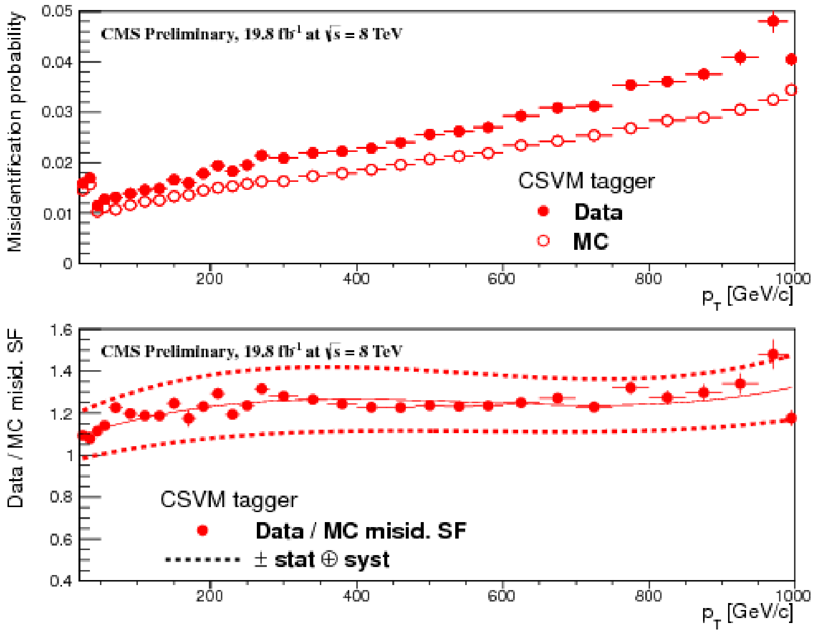

Figure 3.8.: For the CSVM tagging criterion: (top) misidentication probability in data (filled circles) and simulation (open circles); (bottom) scale factor for the misidentication probability. The last p_T bin in each plot includes all jets with $p_T > 1000$ GeV. The solid curve is the result of a polynomial fit to the data points. The dashed curves represent the overall statistical and systematic uncertainties on the measurements.

3.4. Triggering System

With bunch crossings separated by just 25 ns, the rate at which data from all collisions would have to be written out and processed would be unfeasible. A two-tiered triggering system is applied at CMS in order to cope with the high collision rate of protons. The CMS trigger is designed to use limited information from each event to determine whether to record the event, reducing the rate of data taking to manageable levels whilst ensuring a high efficiency of interesting physics object events are selected.

The L1 is a pipelined, dead-timeless system based on custom-built electronics [66], and is a combination of several sub systems which is shown pictorially in Figure 3.9. The L1 system is covered in more detail within the following section along with a description of the service work undertaken by the author to benchmark the performance of the L1 calorimeter trigger during the 2012 8 TeV run period.

The Higher Level Trigger (HLT) is a large farm of commercial computers [67]. The HLT processes events with software reconstruction algorithms that are more detailed, giving performance more similar to the reconstruction used offline. The HLT reduces the event

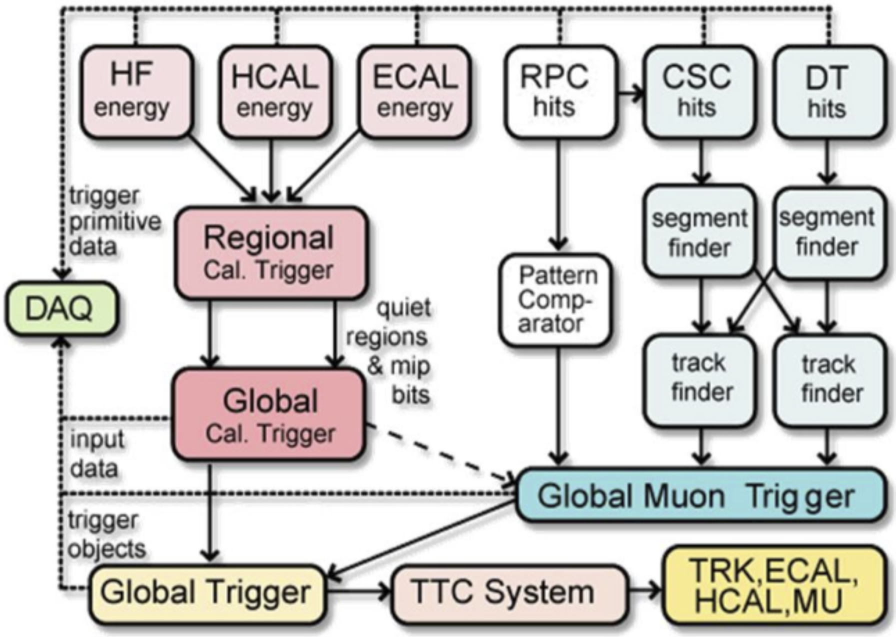

Figure 3.9.: The CMS L1 Trigger system.

rate written to disk by a factor of $\sim$ 500 ($\sim$200Hz). The recorded events are transferred from CMS to the CERN computing centre, where event reconstruction is performed, and then distributed to CMS computing sites around the globe for storage and analysis.

3.4.1. The Level-1 trigger

The L1 trigger reduces the rate of events collected from 40 MHz to $\sim$100 kHz using information from the calorimeters and muon chambers, but not the tracker. A tree system of triggers is used to decide wether to pass on an event to the HLT for further reconstruction. Firstly the calorimeter and muon event information is kept separate, with local reconstruction of objects (μ, e, γ, and jets) performed by the Regional Calorimeter Trigger (RCT) and Regional Muon Trigger (RMT) respectively. The RCT generates up to 72 isolated and non-isolated electromagnetic objects. These are sorted by rank, which is equivalent to transverse energy E_T, with the four highest ranked electromagnetic objects being passed via the Global Calorimeter Trigger (GCT) and Global MuonTrigger (GMT) to the Global Trigger (GT).

In the L1 GCT, coarse measurements of the energy deposited in the electromagnetic and hadronic calorimeters are combined, and by using sophisticated algorithms the following physics objects are formed:

- isolated and non-isolated electromagnetic objects (e and γ);
- hadronic jets in the central and forward sections of the hadronic calorimeters;
- hadronically decaying tau leptons;
- total transverse energy (E_T), the scalar sum of the energy measured at L1, and missing transverse energy ($\not{E}_T$), defined as the vector sum of the energy of L1 objects;
- total transverse jet energy (H_T), the scalar sum of the energy of all L1 jet objects, and missing transverse jet energy ($\not{H}_T$), defined as the vector sum of the energy of L1 jets, are calculated from uncorrected L1 jets.

In addition quantities suitable for triggering minimum bias events, forward physics and beam background events are calculated. Additionally relevant muon isolation information is also passed on to the GMT for decisions involving the muon triggers where it is combined with information from across the three muon sub-systems. The resultant final accept/reject decision at L1 is then performed by the GT based on the objects received from the GCT and GMT (e/γ, μ, jets, E_T, $\not{E}_T$, H_T).

The L1 trigger is therefore of upmost importance to the functioning of the detector. Without a high-performing trigger and a good understanding of it's performance, there would be no data to analyse. Observations of how the L1 trigger performance is affected by changing LHC running conditions over the 2012 run period and also the introduction of a jet seed threshold to the L1 jet trigger algorithm is presented in the following Sections (3.4.2 - 3.4.6).

3.4.2. The L1 trigger jet algorithm

The L1 jet trigger uses the transverse energy sums computed in the calorimeter (both hadronic and electromagnetic) trigger regions. Each region consists of 4×4 trigger tower windows, spanning a region of $\Delta\eta \times \Delta\phi = 0.087 \times 0.087$ in pseudorapidity-azimuth. The jet trigger uses a 3×3 calorimeter region (112 trigger towers) sliding window technique which spans the full (η, ϕ) coverage of the CMS calorimeter as shown in Figure 3.10.

In forming a L1 jet is it required that the central region to be higher than the eight neighbouring regions $E_{\mathrm{T\ central}} > E_{\mathrm{T\ surround}}$. Additionally a minimum threshold of 5 GeV on $E_{\mathrm{T\ central}}$ was introduced during the 2012 run period to suppress noise from pile-up. A comparison between these two configurations is shown in Section (3.4.4).

The L1 jets are characterised by the E_T, summed over the 3×3 calorimeter regions, which corresponds to 12×12 trigger towers in barrel and endcap or 3×3 larger HF towers in the HF. The ϕ size of the jet window is the same everywhere, whilst the η binning gets somewhat larger at high η due to calorimeter and trigger tower segmentation. The jets are labelled by the (η, ϕ) indicies of the central calorimeter region.

Jets with $|\eta| > 3.0$ are classified as forward jets, whereas those with $|\eta| < 3.0$ are classified as central. The four highest energy central, forward and τ jets in the calorimeter are passed through Look Up Table (LUT)'s, which apply a programmable η−dependent jet energy scale correction. These are then used to make L1 trigger decisions.

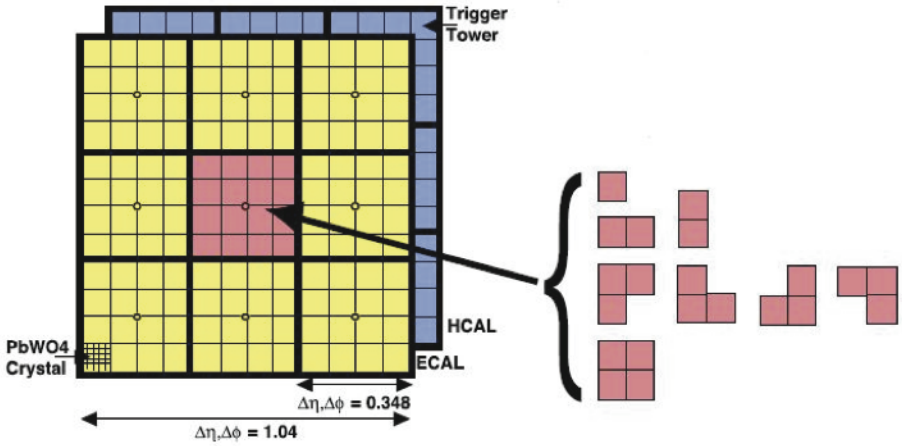

Figure 3.10.: Illustration of the Level-1 jet finding algorithm.

The performance of the L1 jets is evaluated with respect to offline jets, which are taken from the standard Calo jet and the PF jet reconstruction algorithms of CMS. Jets are corrected for pile-up and detector effects as described in 3.3.1. A moderate level of noise rejection is applied to the offline jets by selecting jets passing the "loose" identification criteria for both Calo and PF. These jet criteria are listed in Appendix (A.1).

3.4.3. Measuring L1 jet trigger efficiencies

The L1 jet efficiency is defined as the fraction of leading offline jets which were matched with a L1 tau or central jet above a certain trigger threshold, divided by all the leading offline jets in the event. This quantity is then plotted as a function of the offline jet E_T, η and ϕ.

The efficiency is determined by matching the L1 and reconstructed offline jets spatially in $\eta - \phi$ space. This is done by calculating the minimum separation in ΔR between the highest offline reconstructed jet in E_T ($E_T > 10$ GeV,$|\eta| < 3$) and any L1 jet. A jet will be matched if this value is found to be < 0.5. Should more than one jet satisfy this, the jet closest in ΔR is taken as the matched jet. The matching efficiency is close to 100%, above 30(45) GeV for run 2012B(C) data (see Appendix B.1).

Each efficiency curve is fitted with a function which is the cumulative distribution function of an Exponentially Modified Gaussian (EMG) distribution:

$$f(x;\mu,\sigma,\lambda) = \frac{\lambda}{2} \cdot e^{\frac{\lambda}{2}(2\mu+\lambda\sigma^2-2x)} \cdot \mathrm{erfc}\left(\frac{\mu+\lambda\sigma^2-x}{\sqrt{2}\sigma}\right) \tag{3.3}$$

where erfc is the complementary error function defined as:

$$\mathrm{erfc}(x) = 1 - \mathrm{erf}(x) = \frac{2}{\sqrt{\pi}}\int_x^\infty e^{-t^2}dt.$$

In this functional form, the parameter μ determines the point of 50% of the plateau efficiency and the σ gives the resolution. This parametrisation is used to benchmark the efficiency at the plateau, the turn-on points and resolution for each L1 Jet trigger. The choice of function is purely empirical. Previous studies used the error function alone, which described the data well at high threshold values but could not describe the efficiencies well at lower thresholds [68].

The efficiency turn-on curves for various L1 jet thresholds are evaluated as a function of the offline reconstructed jet E_T for central jets with $|\eta| < 3$. These are measured using single isolated μ triggers which have high statistics, and are orthogonal and therefore unbiased to the hadronic triggers under study. The efficiency is calculated with respect to offline Calo and PF Jets in Figure 3.11. Table 3.1 shows the values of these parameters, calculated for three example L1 single jet triggers taken from 2012 8 TeV data.

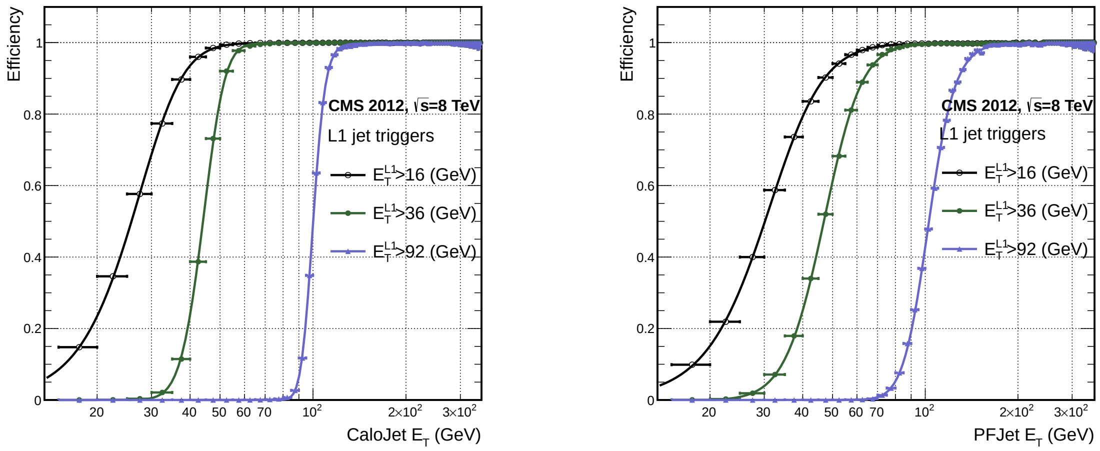

Figure 3.11.: L1 jet efficiency turn-on curves as a function of the offline CaloJet E_T (left) and PFJet E_T (right), measured in 2012 Run Period C data and collected with an isolated single μ data sample.

	Calo		PF	
Trigger	μ	σ	μ	σ
L1_SingleJet16	21.09 $\pm$ 0.03	7.01 $\pm$ 0.02	22.17 $\pm$ 0.04	7.83 $\pm$ 0.03
L1_SingleJet36	41.15 $\pm$ 0.05	5.11 $\pm$ 0.02	39.16 $\pm$ 0.06	8.04 $\pm$ 0.03
L1_SingleJet92	95.36 $\pm$ 0.13	5.62 $\pm$ 0.03	90.85 $\pm$ 0.19	11.30 $\pm$ 0.10

Table 3.1.: Results of a cumulative EMG function fit to the turn-on curves for L1 single jet triggers in run 2012 Run Period C, measured in an isolated μ data sample. The turn-on point, μ, and resolution, σ, of the L1 jet triggers are measured with respect to offline Calo Jets (left) and PF Jets (right).

The results from the L1 single jet triggers shows good performance for both Calo and PF jets. A better resolution for Calo jets with respect to L1 jets quantities is observed. This effect is due to Calo jet reconstruction using the same detector systems as in L1 jets, whereas with PF jet construction using tracker and muon information, a more smeared resolution when compared to L1 is expected.

3.4.4. Effects of the L1 jet seed

Between run period B and C of the 2012 data taking period, a jet seed threshold was introduced into the L1 trigger jet algorithm. There was previously no direct requirement made on the energy deposited in the central region. The introduction of a jet seed threshold required that the central region have $E_T \geq 5$GeV, and was introduced to counteract the effects of high pile up running conditions which create a large number of soft non-collimated jets, that are then added to the jets from the primary interaction or other soft jets from other secondary interactions [69]. This in turn causes a large increase in trigger rate due to the increase in the likelihood that the event causes the L1 trigger to fire. This was implemented to maintain trigger thresholds by cutting the rate of events recorded without significant reduction in the efficiency of physics events of interest.

The effect of the introduction of this jet seed threshold between these two run periods is benchmarked through a comparison of the efficiency of the L1 jet triggers with respect to offline Calo jets shown in Figure 3.12, and the L1 H_T trigger efficiency in Figure 3.14 which is compared to offline H_T constructed from Calo jets with $E_T \geq 40$GeV.

To negate any effects from different pile-up conditions in the run periods, the efficiencies are measured in events which contain between 15 and 20 primary vertices as defined in Appendix (A.2).

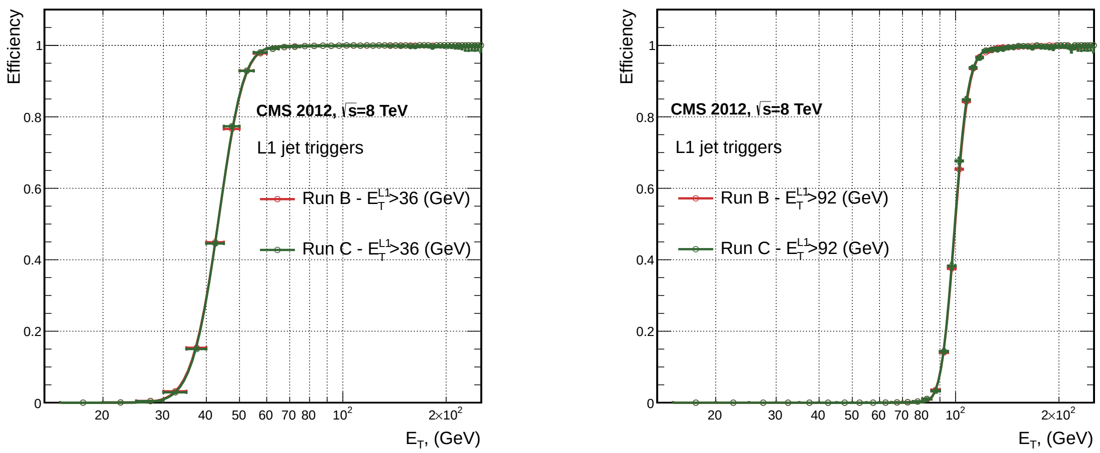

Figure 3.12.: L1 jet efficiency turn-on curves as a function of the offline CaloJet E_T, measured for the L1 SingleJet 36 and 92 trigger in 2012 run period B and C collected with an isolated single μ' sample.

It can be seen that the performance of the $E_T > 36, 92$ single jet are almost identical, with the jet seed having no measurable effect on these triggers as shown in Table 3.2 .

For the H_T triggers, a large increase in rate during high pile-up conditions is expected. This is due to the low energy threshold required for a jet to be added to the L1 H_T sum, which is compiled from all uncorrected L1 jets formed in the RCT. The introduction of the jet seed threshold removes the creation of many of these soft low E_T jets, thus

	2012B		2012C	
Trigger	μ	σ	μ	σ
L1_SingleJet36	40.29 ± 0.04	5.34 ± 0.02	40.29 ± 0.11	5.21 ± 0.05
L1_SingleJet92	94.99 ± 0.09	5.93 ± 0.06	94.82 ± 0.29	5.74 ± 0.18

Table 3.2.: Results of a cumulative EMG function fit to the turn-on curves for L1 single jet triggers in the 2012 run period B and C, preselected on an isolated muon trigger. The turn-on point μ and resolution σ of the L1 jet triggers are measured with respect to offline Calo Jets in run B (left) and run C (right).

lowering the H_T calculation at L1. The effect on the trigger cross section for L1 H_T 150 trigger can be seen in Figure 3.13.

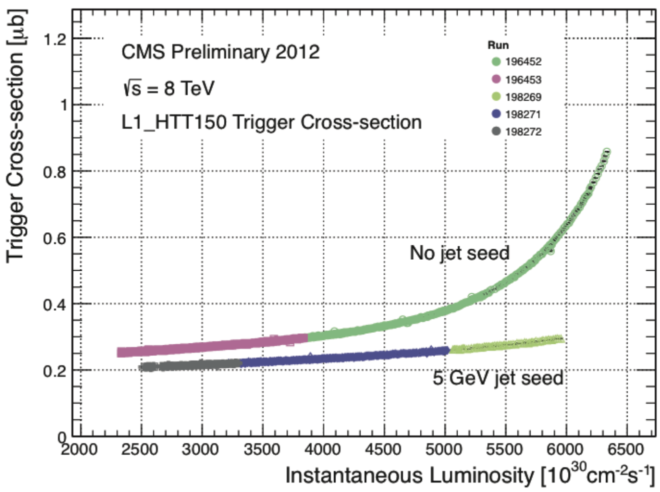

Figure 3.13.: Trigger cross section for the L1HTT150 trigger path. Showing that a 5 GeV jet seed threshold dramatically reduces the dependance of cross section on the instantaneous luminosity for L1 H_T triggers [70].

Different behaviours for the trigger turn ons between these run periods are therefore expected. The turn on point is observed to shift to higher H_T values after the introduction of the jet seed threshold, whilst having a sharper resolution due to less pile-up jets being included the H_T sum. This effect is demonstrated in Table 3.3.

3.4.5. Robustness of L1 jet performance against pile-up

The performance of the L1 single jet triggers is evaluated in different pile-up conditions to benchmark any dependence on pile-up. Three different pile-up bins of 0-10, 10-20 and >20 vertices are defined, reflecting the low, medium and high pile-up running conditions

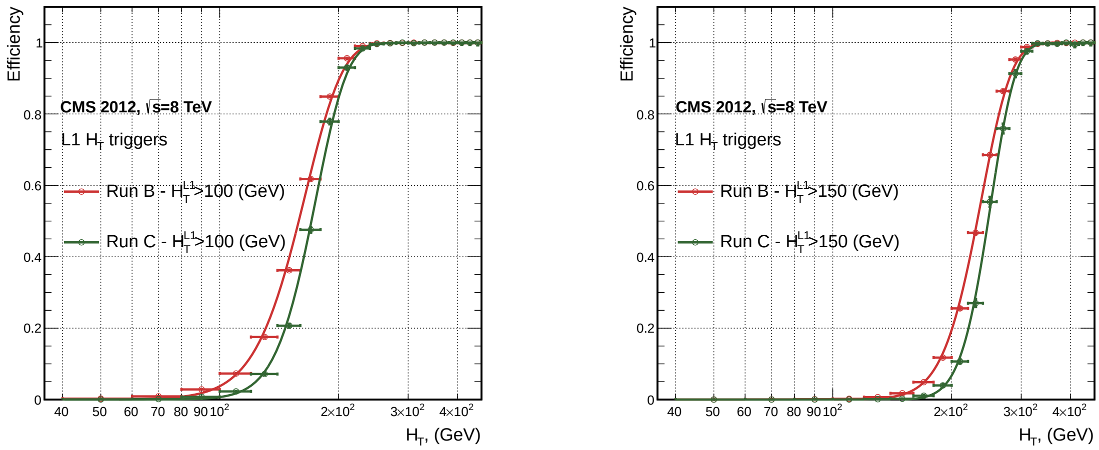

Figure 3.14.: L1 H_T efficiency turn-on curves as a function of the offline CaloJet H_T, measured for the L1 H_T 100 and 150 trigger during the run 2012 B and C collected using an isolated single μ triggered sample.

	2012B		2012C	
Trigger	μ	σ	μ	σ
L1 HT-100	157.5 $\pm$ 0.08	32.9 $\pm$ 0.08	169.8 $\pm$ 0.08	28.7 $\pm$ 0.03
L1 H1-150	230.9 $\pm$ 0.02	37.3 $\pm$ 0.01	246.4 $\pm$ 0.16	31.8 $\pm$ 0.05

Table 3.3.: Results of a cumulative EMG function fit to the turn-on curves for H_T in run 2012 B and C, preselected on an isolated single μ trigger. The turn-on point μ, resolution σ of the L1 H_T triggers are measured with respect to offline H_T formed from CaloJets with a $E_T \geq 40$ in run period B (left) and C (right).

at CMS in 2012. This is benchmarked relative to Calo and PF jets for the run 2012 C period where the jet seed threshold is applied, with L1 single jet thresholds of 16, 36 and 92 GeV, shown in Figure 3.15. The results of fits to these efficiency turn-on curves are given in Table 3.4 and Table 3.5 for Calo and PF jets respectively.

Vertices	0-10		11-20		> 20	
	μ	σ	μ	σ	μ	σ
L1_SingleJet16	19.9 $\pm$ 0.1	6.1 $\pm$ 0.3	20.8 $\pm$ 0.1	6.5 $\pm$ 0.1	22.3 $\pm$ 0.2	7.5 $\pm$ 0.1
L1_SingleJet36	41.8 $\pm$ 0.1	4.6 $\pm$ 0.1	40.9 $\pm$ 0.1	5.1 $\pm$ 0.1	40.6 $\pm$ 0.6	5.9 $\pm$ 0.2
L1_SingleJet92	95.9 $\pm$ 0.2	5.4 $\pm$ 0.1	95.2 $\pm$ 0.2	5.6 $\pm$ 0.1	94.5 $\pm$ 0.6	6.2 $\pm$ 0.3

Table 3.4.: Results of a cumulative EMG function fit to the efficiency turn-on curves for L1 single jet triggers in the 2012 run period C, measured from isolated μ triggered data. The turn-on point, μ, and resolution, σ, of the L1 jet triggers are measured with respect to offline Calo jets in low (left), medium (middle) and high (right) pile-up conditions.

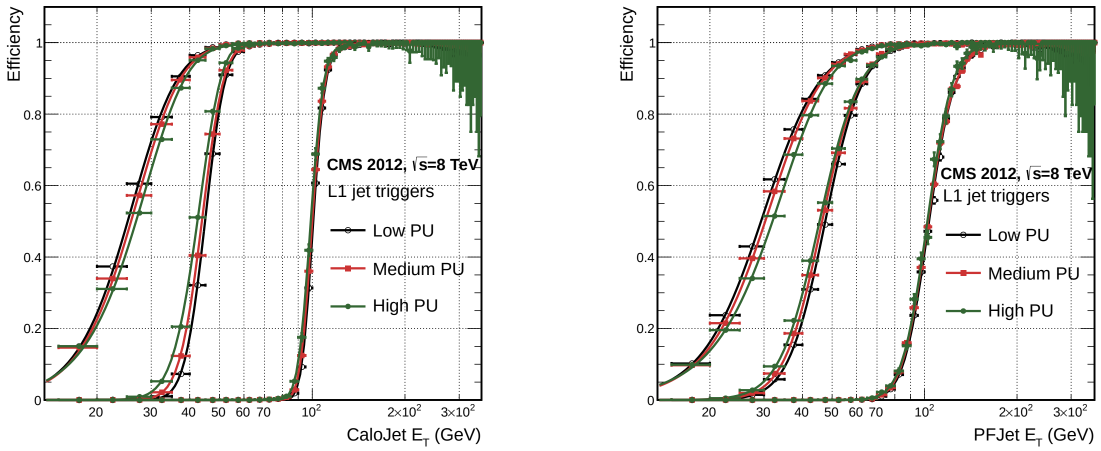

Figure 3.15.: L1 jet efficiency turn-on curves as a function of the leading offline E_TCalo (left) and PF (right) jet, for low, medium and high pile-up conditions.

Vertices	0-10		11-20		> 20	
	μ	σ	μ	σ	μ	σ
L1_SingleJet16	21.1 $\pm$ 0.1	7.16 $\pm$ 0.05	22.34 $\pm$ 0.1	7.9 $\pm$ 0.1	24.6 $\pm$ 0.2	9.5 $\pm$ 0.1
L1_SingleJet36	39.6 $\pm$ 0.1	7.4 $\pm$ 0.1	38.4 $\pm$ 0.1	7.4 $\pm$ 0.1	37.1 $\pm$ 0.2	7.5 $\pm$ 0.1
L1_SingleJet92	91.6 $\pm$ 0.3	11.3 $\pm$ 0.2	90.4 $\pm$ 0.3	11.2 $\pm$ 0.1	92.0 $\pm$ 0.9	12.1 $\pm$ 0.4

Table 3.5.: Results of a cumulative EMG function fit to the efficiency turn-on curves for Level-1 single jet triggers in the 2012 run period C, measured from isolated μ triggered data. The turn-on point, μ, and resolution, σ, of the L1 jet triggers are measured with respect to offline PF jets in low (left), medium (middle) and high (right) pile-up conditions.

No significant drop in efficiency is observed in the presence of a high number of primary vertices. The increase in hadronic activity in higher pile-up conditions, combined with the absence of pile-up subtraction for L1 jets, results in the expected observation of a decrease in the μ value of the efficiency turn-ons as a function of pile-up, while the resolution, σ of the turn-ons are found to gradually worsen as expected with increasing pile-up.

These features are further emphasised when shown as a function of

$$\frac{(\text{L1 E}_T - \text{Offline E}_T)}{\text{Offline E}_T} \tag{3.4}$$

in bins of matched leading offline jet E_T, of which the individual fits can be found in Appendix (B.2). Each of these distributions are fitted with an EMG function as defined in Equation (3.3).

The μ, σ and λ values extracted for the low, medium and high pile-up conditions are shown for Calo and PF jets in Figure 3.16 and Figure 3.17 respectively. The central value of $\frac{(\text{L1 E}_T - \text{Offline E}_T)}{\text{Offline E}_T}$ is observed to increases as a function of jet E_T, whilst the resolution is also observed to improve at higher offline jet E_T.

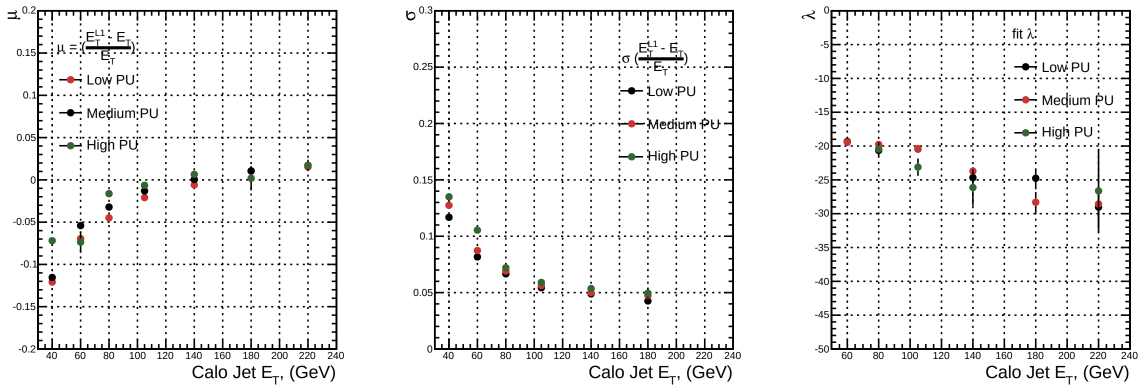

Figure 3.16.: Fit values from an EMG function fitted to the resolution plots of leading Calo jet E_T measured as a function of $\frac{(\text{L1 E}_T - \text{Offline E}_T)}{\text{Offline E}_T}$ for low, medium and high pile-up conditions. The plots show the mean μ (left), resolution σ (middle) of the Gaussian as well as the decay term λ (right) of the exponential.

The resolution of other L1 jet based energy sum quantities, $\not{H}_T$ and H_T parameterised as in Equation (3.4), can be found in Appendix (B.3). The same behaviour observed for the single jet triggers is also found for these quantities, where in the presence of higher pile-up the μ values are shifted to higher values, with a worsening resolution, σ again due to the increase in soft pile-up jets and the absence of pile-up subtraction at L1.

3.4.6. Summary

The performance of the CMS Level-1 Trigger has been studied and evaluated for jets and energy sum quantities using data collected during the 2012 LHC 8 TeV run. These studies include the effect of introduction of a 5 GeV jet seed threshold into the jet algorithm configuration, the purpose of which is to mitigate the effects of pile-up on the rate of L1 triggers whilst not adversely affecting the efficiency of these triggers. No significant

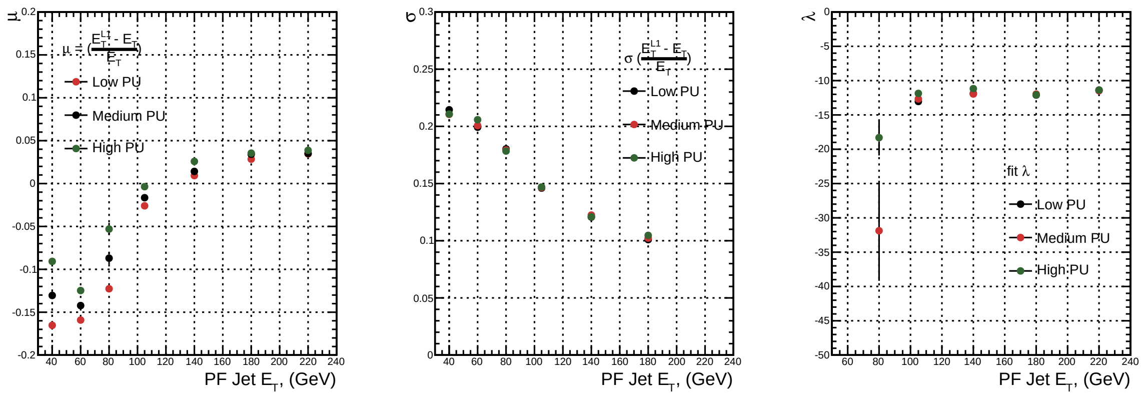

Figure 3.17.: Fit values from an EMG function fitted to the resolution plots of leading PF jet E_T measured as a function of $\frac{(\text{L1 E}_T - \text{Offline E}_T)}{\text{Offline E}_T}$ for low and medium pile-up conditions. The plots show the mean μ (left), resolution σ (middle) of the Gaussian as well as the decay term λ (right) of the exponential.

change in performance is observed with this change and good performance is observed for a range of L1 quantities.

Chapter 4.

SUSY Searches In Hadronic Final States

In this chapter a model independent search for SUSY in hadronic final states with $\not\!\!E_T$ using the α_T variable at different b-quark and jet multiplicities is introduced and described in detail. The results presented are based on a data sample of pp collisions collected in 2012 at $\sqrt{s}$ =8 TeV, corresponding to an integrated luminosity of 11.7 ± 0.5 fb^{-1} [5].

The kinematic variable α_T is motivated as a variable to provide strong rejection of the overwhelming QCD background, prevalent to jets $+\not\!\!E_T$ final states at the LHC. This is achieved whilst maintaining sensitivity to a possible SUSY signal and described in Section (4.1). The search and trigger strategy in addition to the event reconstruction and selection are outlined within Sections (4.2 - 4.3).

The method in which the SM background is estimated using an analytical technique to improve statistical precision at higher b-tag multiplicities is detailed within Section (4.5). Included in this section is a discussion on the impact of b-tagging and mis-tagging scale factors between data and simulation on any background predictions. Improved precision in estimating background yields at large number of b-tagged jets, is important in the context of interpreting natural SUSY models, first outlined in Section (2.4.1).

A description of the formulation of appropriate systematic uncertainties applied to the background predictions to account for theoretical uncertainties and limitations in the simulation modelling of event kinematics and instrumental effects is covered in Section (4.6). Similarly the systematic determination for the SMS signal samples used to interpret the physics reach of the analysis are examined in Section (4.7).

Finally the statistical likelihood model to interpret the observations in the signal and control samples is described in Section (4.8). The experimental reach of the analysis discussed within this thesis is interpreted in two classes of SMS models, both first introduced in Section (2.4.1). The SMS models considered in this analysis are summarised in Table 4.1. For each model, the LSP is assumed to be the lightest neutralino.

Within the table are also defined reference points, parameterised in terms of parent gluino/squark and LSP sparticle masses, $\mathrm{m}_{\mathrm{parent}}$ and $\mathrm{m}_{\mathrm{LSP}}$, respectively, which are used within the following two chapters to demonstrate potential yields within the signal region of the search.

The masses are chosen to reflect parameter space which is within the expected sensitivity reach of the search, and also in the case of `T1tttt` and `T1bbbb`, reflect examples of potential natural SUSY topologies.

Model	Production/decay mode	Reference model	
		$\mathrm{m}_{\mathrm{parent}}$	$\mathrm{m}_{\mathrm{LSP}}$
G1 (`T1`)	$pp \to \widetilde{g}\widetilde{g}^* \to q\bar{q}\widetilde{\chi}_1^0 q\bar{q}\widetilde{\chi}_1^0$	700	300
G2 (`T1bbbb`)	$pp \to \widetilde{g}\widetilde{g}^* \to b\bar{b}\widetilde{\chi}_1^0 b\bar{b}\widetilde{\chi}_1^0$	900	500
G3 (`T1tttt`)	$pp \to \widetilde{g}\widetilde{g}^* \to t\bar{t}\widetilde{\chi}_1^0 t\bar{t}\widetilde{\chi}_1^0$	850	250
D1 (`T2`)	$pp \to \widetilde{q}\widetilde{q}^* \to q\widetilde{\chi}_1^0 \bar{q}\widetilde{\chi}_1^0$	600	250
D2 (`T2bb`)	$pp \to \widetilde{b}\widetilde{b}^* \to b\widetilde{\chi}_1^0 \bar{b}\widetilde{\chi}_1^0$	500	150
D3 (`T2tt`)	$pp \to \widetilde{t}\widetilde{t}^* \to t\widetilde{\chi}_1^0 \bar{t}\widetilde{\chi}_1^0$	400	0

Table 4.1.: A summary of the SMS models interpreted in this analysis, involving both direct (D) and glunio-induced (G) production of squarks and their decays. Reference models are also defined in terms of parent and LSP sparticle mass

4.1. An Introduction to the α_T Search

A proton-proton collision resulting in the production and decay of supersymmetric particles, would manifest as a final state containing energetic jets and $\not{E}_T$ in the hadronic channel. The search focuses on topologies where new heavy supersymmetric, R-parity conserving particles are pair-produced in pp collisions. These particles decaying to a LSP escape the detector undetected, leading to significant missing energy and missing hadronic transverse energy,

$$\not\!\!H_T = |\sum_{i=1}^{n} \vec{p_T}^{jet_i}|, \tag{4.1}$$

defined as the vector sum of the transverse energies of jets selected in an event. Energetic jets produced in the decay of these supersymmetric particles also can produce significant visible transverse energy,

$$H_T = \sum_{i=1}^{n} E_T^{jet_i}, \tag{4.2}$$

defined as the scalar sum of the transverse energies of jets selected in an event.

A search within this channel is greatly complicated in a hadron collider environment, where the overwhelming background comes from inherently balanced multi-jet ("QCD") events which are produced with an extremely large cross section as demonstrated within Figure 4.1. $\not\!\!E_T$ can appear in such events with a substantial mis-measurement or stochastic fluctuations of jet energy or missed objects due to detector mis-calibration or noise effects.

Additional SM background from EWK processes with genuine $\not\!\!E_T$ from escaping neutrinos comprise the irreducible background within this search and come mainly from:

- $Z \to \nu\bar{\nu}+$ jets,
- $W \to l\nu$ + jets in which a lepton falls outside of detector acceptance, is not reconstructed, is mis-identified, or the lepton decays hadronically $\tau \to$ had ,
- $t\bar{t}$ with at least one leptonically decaying W, which is missed in the detector as detailed above,
- small background contributions from DY, single top and Diboson (WW,ZZ,WZ) processes.

The search is designed to have a strong separation between events with genuine and "fake" $\not\!\!E_T$ which is achieved primarily though the dimensionless kinematic variable, α_T [71][72].

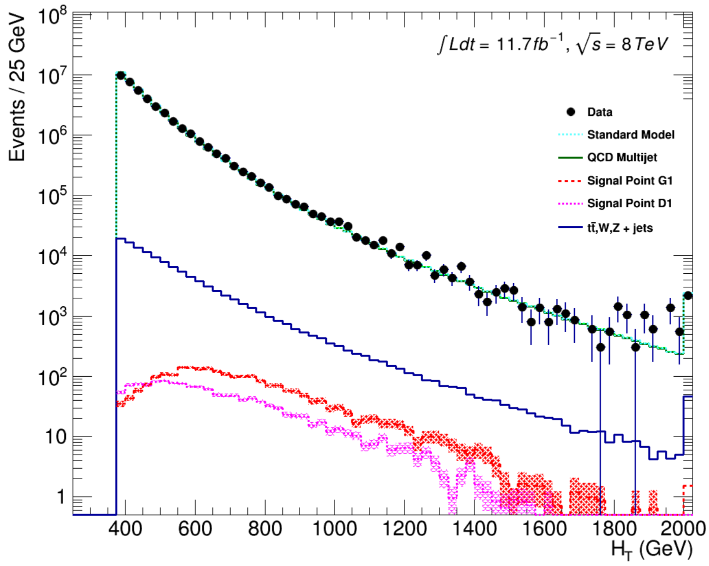

Figure 4.1.: Reconstructed offline H_T distribution in the hadronic signal selection, from 11.7fb^{-1} of data, in which no α_T requirement is made. Sample is collected from prescaled H_T triggers. Overlaid are expectations from MC simulation of EWK processes as well as two reference signal models (labelled G1 and D1 from Table 4.1).

4.1.1. The α_T variable

For a perfectly measured di-jet QCD event, conservation laws dictate that both jets must be of equal magnitude and produced in opposite directions. However in the case of di-jet events with genuine $\not\!\!E_T$ (as detailed above), no such requirement is made of the two jets, as depicted in Figure 4.2.

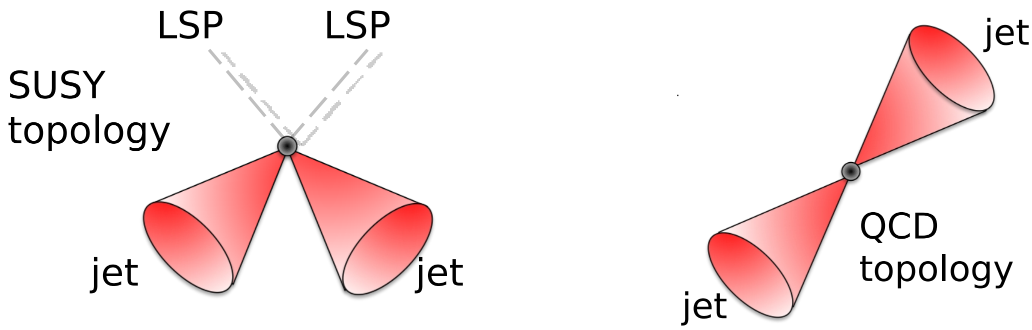

Figure 4.2.: The event topologies of background QCD diet events (right) and a generic SUSY signature with genuine $\not\!\!E_T$ (left).

Exploiting this feature leads to the formulation of α_T (first inspired by [73]) in di-jet systems defined as,

$$\alpha_T = \frac{E_T^{j_2}}{M_T}, \tag{4.3}$$

where $E_T^{j_2}$ is the transverse energy of the least energetic of the two jets and M_T defined as:

$$M_T = \sqrt{\left(\sum_{i=1}^{2} E_T^{j_i}\right)^2 - \left(\sum_{i=1}^{2} p_x^{j_i}\right)^2 - \left(\sum_{i=1}^{2} p_y^{j_i}\right)^2} \equiv \sqrt{H_T^2 - \not{H}_T{}^2}. \tag{4.4}$$

A perfectly balanced di-jet event i.e. $E_T^{j_1} = E_T^{j_2}$ would yield an α_T value of 0.5, where as events with jets which are not back-to-back, for example in events in which a W or Z recoils off a system of jets, α_T can achieve values in excess of 0.5. Most importantly balanced QCD events in which jets are mis-measured, will generally result in an α_T of less than 0.5, thus giving the α_T variable discriminating power between these processes.

α_T can be extended to apply to any arbitrary number of jets, undertaken by modelling a system of n jets as a di-jet system, through the formation of two pseudo-jets [74]. The two pseudo-jets are built by merging the jets present in the event such that the 2 pseudo-jets are chosen to be as balanced as possible, i.e the $\Delta H_T \equiv |E_T^{pj_1} - E_T^{pj_2}|$ is minimised between the two pseudo jets. Using Equation (4.4), α_T can be rewritten as,

$$\alpha_T = \frac{1}{2}\frac{H_T - \Delta H_T}{\sqrt{H_T{}^2 - \not{H}_T{}^2}} = \frac{1}{2}\frac{1 - \Delta H_T/H_T}{\sqrt{1 - (\not{H}_T/H_T)^2}}. \tag{4.5}$$

The distribution of α_T for the two jet categories used within this analysis, $2 \leq n_{jet} \leq 3$ and $n_{jet} \geq 4$ jets, is shown in the Figure.4.3. It can be seen that the distributions peak at an α_T of 0.5, before falling away sharply and being free of multi-jet background at larger α_T values. These distributions serve to demonstrate the ability of the α_T variable to discriminate between multi-jet events and EWK processes with genuine $\not{E}_T$ in the final state.

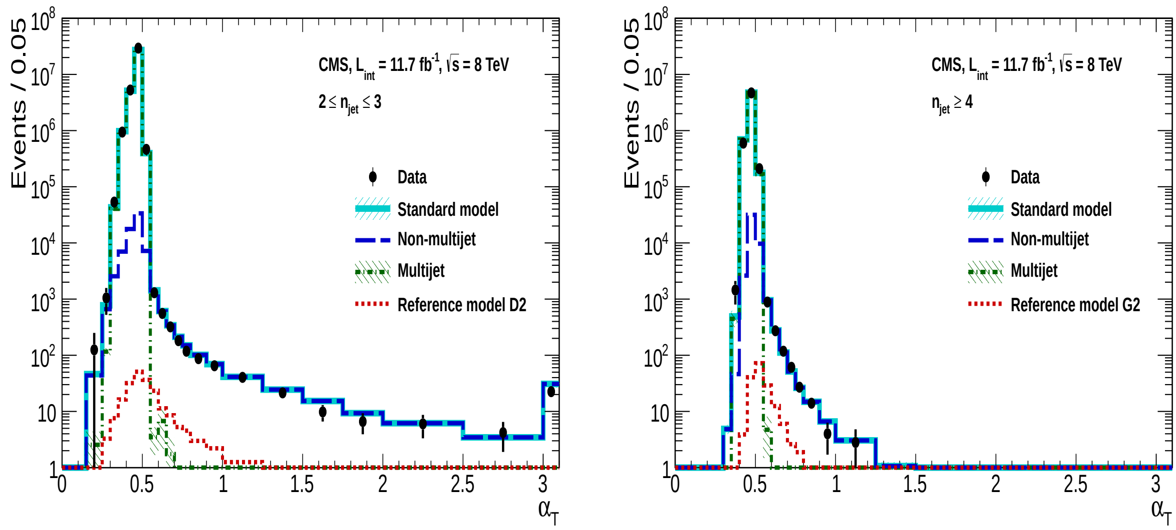

Figure 4.3.: The α_T distributions for the low 2-3 (left) and high ≥ 4 (right) jet multiplicities after a full analysis selection and shown for $H_T > 375$. Data is collected using both prescaled H_T triggers and dedicated α_T triggers for below and above $\alpha_T = 0.55$ respectively. . Expected yields as given by simulation are also shown for multi-jet events (green dash-dotted line), EWK backgrounds with genuine $\not{E}_T$ (blue long-dashed line), the sum of all SM processes (cyan solid line) and the reference signal model D2 (left, red dotted line) or G2 (right, red dotted line).

The α_T requirement used within the search is chosen to be $\alpha_T > 0.55$ to ensure that the QCD multi-jet background is negligible even in the presence of moderate jet mis-measurement. There still remains other effects which can cause multi-jet events to artificially have a large α_T value, which are discussed in detail in Section (4.2.2).

4.2. Search Strategy

The aim of the analysis presented in this thesis is to identify an excess of events in data over the SM background expectation in multi-jet final states and significant $\not{E}_T$. The essential suppression of the dominant QCD background for such a search is addressed by the α_T variable described in the previous section. For estimation of the remaining EWK backgrounds, three independent data control samples are used to predict the different processes that compose the background :

- μ + jets control sample to determine W + jets, $t\bar{t}$ and single top backgrounds,
- γ + jets control sample to determine the irreducible Z $\rightarrow \nu\bar{\nu}$ + jets background,

- $\mu\mu$ + jets control sample to also determine the irreducible Z $\rightarrow \nu\bar{\nu}$ + jets background.

These control samples are chosen to both be rich in specific EWK processes, be free of QCD multi-jet events and to also be kinematically similar to the hadronic signal region that they are estimating the backgrounds of, see Section (4.2.3). The redundancy of using the γ + jets and $\mu\mu$ + jets sample to predict the same background within the signal region, brings an opportunity to reliably cross check and validate the background estimation method and is utilised in both the determination of background estimation systematics (Section(4.6)), and in the maximum likelihood fit (Section(4.8)).

To remain inclusive to a large range of possible SUSY models, the signal region is split into the following categories to allow for increased sensitivity in the interpretation of results for different SUSY topologies:

Sensitivity to a range of SUSY mass splittings

The hadronic signal region is defined by $H_T > 275$, divided into eight bins in H_T.

- Two bins of width 50 GeV in the range $275 < H_T < 375$ GeV,
- five bins of width 100 GeV in the range $375 < H_T < 875$ GeV,
- and a final open bin, $H_T > 875$ GeV.

The choice of the lowest H_T bin in the analysis is driven primarily by trigger constraints. The mass difference between the LSP and the particle that it decays from is an important factor in the amount of hadronic activity in the event.

A large mass splitting will lead to hard high p_T jets which contribute to the H_T sum. From Figure 4.1 it can be seen that the SM background falls sharply at high H_T values, therefore binning in H_T will lead to easier of identification of such signals. Conversely smaller mass splittings lead to softer jet p_T's which will subsequently fall into the lower H_T range.

Sensitivity to production method of SUSY particles

The production mechanism of any potential SUSY signal can lead to different event topologies. One such way to discriminate between gluino ($g\widetilde{g}$ - "high multiplicity"), and direct squark ($q\widetilde{q}$ - "low multiplicity") induced production of SUSY particles is realised through the number of reconstructed jets in the final state.

The analysis is thus split into two jet categories : 2-3 jets , ≥ 4 jets to give sensitivity to both of these mechanisms.

Sensitivity to "Natural SUSY" via tagging jets from b-quarks

Jets originating from bottom quarks (b-jets) are identified through vertices that are displaced with respect to the primary interaction. The algorithm used to tag b-jets is the Combined Secondary Vertex Medium Working Point (CSVM) tagger, described within Section (3.3.2). A cut is placed on the discriminator variable of > 0.679, leading to a gluon/light-quark mis-tag rate of approximately 1% and a jet p_T dependant b-tagging efficiency of 60-70% [?].

Natural SUSY models would be characterised through final-state signatures rich in bottom quarks. A search relying on methods to identify jets originating from bottom quarks through b-tagging, will significantly improve the sensitivity to this class of signature. This gain in sensitivity stems from a vast reduction in the vector boson + jet backgrounds (W,Z) at higher b-tag jet multiplicities, which typically have no b-flavoured quarks in their decays.

Therefore events are categorised according to the number of b-tagged jets reconstructed in each event, in the following: 0,1,2,3,≥ 4 b-tag categories . In the highest ≥ 4 b-tag category due to a limited number of expected signal and background, just three H_T bins are employed: 275-325 GeV, 325-375 GeV, ≥ 375 GeV.

This characterisation is identically mirrored in all control samples, with the information from all samples and b-tag categories used simultaneously in the likelihood model, see Section (4.8).

The combination of the H_T, jet multiplicity and b-tag categorisation of the signal region as described above, resultantly leads to 67 different bins in which the analysis is interpreted in, and is depicted in Figure 4.4.

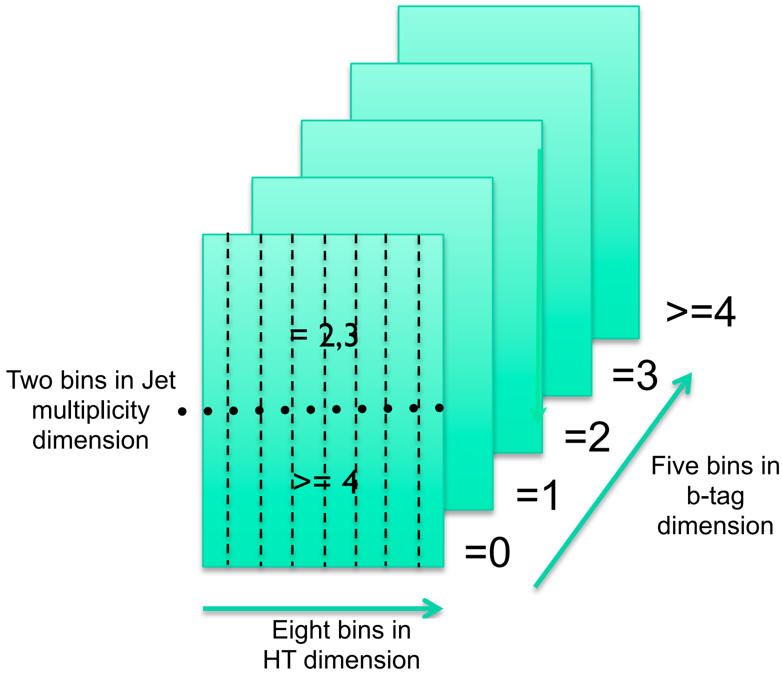

Figure 4.4.: Pictorial depiction of the analysis strategy employed by the α_T search to increase sensitivity to a wide spectra of SUSY models.

4.2.1. Physics objects

The physics objects used in the analysis defined below, follow the recommendation of the various CMS Physics Object Groups (POGs).

- **Jets**

  The jets used in this analysis are CaloJets, reconstructed as described in Section (3.3.1) using the anti-k$_T$ jet clustering algorithm.

  To ensure the jet object falls within the calorimeter systems a pseudo-rapidity requirement of $|\eta| < 3$ is applied. Each jet must pass a "loose" identification criteria to reject jets resulting from unphysical energy, the criteria of which are detailed in Table A.1 [75].

- **Muons**

  Muons are selected in the μ + jets and $\mu\mu$ + jets control samples, and vetoed in the signal region. The same cut based identification criteria is applied to muons in both search regions and is summarised in Table 4.2 [76].

Variable	Definition
Is Global Muon	Muon contains both a hit in the muon chamber and a matched track in the inner tracking system .
$\chi^2 < 10$	χ^2 of global muon track fit. Used to suppress hadronic punch-through and muons from decays in flight.
Muon chamber hits > 0	At least one muon chamber hit included in global muon track fit.
Muon station hits > 1	Muon segment hits in at least two muon stations, which suppresses hadronic punch-through and accidental track-to-segment matches.
$d_{xy} < 0.2$mm	The tracker track transverse impact parameter w.r.t the primary vertex. Suppresses cosmic muons and muons from decays in flight.
$d_z < 0.5$mm	The longitudinal distance of the tracker track w.r.t the primary vertex. Loose cut to further suppress cosmic muons, muons from decays in flight and tracks from pileup.
Pixel hits > 0	Suppresses muons from decays in flight by requiring at least one pixel hit in the tracker.
Track layer hits > 5	Number of tracker layers with hits, to guarantee a good p_T measurement. Also suppresses muons from decays in flight.
PF Iso <0.12	Isolation based upon the sum of the charged and neutral hadrons and photon objects within a ΔR 0.4 cone of the muon object, corrected for pile up effects on the isolation sum.

Table 4.2.: Muon Identification criteria used within the analysis for selection/veto purposes in the muon control/signal selections.

Additionally muons are required to be within the acceptance of the muon tracking systems. For the muon control samples, trigger requirements necessitate a $|\eta| < 2.1$ for the selection of muons. In the signal region where muons are vetoed these conditions are relaxed to $|\eta| < 2.5$ and a minimum threshold of $p_T > 10$ GeV is required of muon objects.

- **Photons**

Photons are selected within the γ + jets control sample and vetoed in all other selections. Photons are identified in both cases according to the cut based criteria listed in Table 4.3 [77].

Variable	Definition
H/E < 0.05	The ratio of hadronic energy in the HCAL tower directly behind the ECAL super-cluster and the ECAL super-cluster itself.
$\sigma_{i\eta i\eta} < 0.011$	The log energy weighted width (σ), of the extent of the shower in the η dimension.
R9 < 1.0	The ratio of the energy of the 3×3 crystal core of the super-cluster compared to the total energy stored in the 5×5 super-cluster.
Combined Isolation < 6 GeV	The photons are required to be isolated with no electromagnetic or hadronic activity within a radius ΔR $= 0.3$ of the photon object. A combination of the pileup subtracted [78], ECAL, HCAL and tracking isolation sums are used to determine the combined total isolation value.

Table 4.3.: Photon Identification criteria used within the analysis for selection/veto purposes in the γ + jets control/signal selections.

Photon objects are also required to have a minimum momentum of $p_T > 25$ GeV.

- **Electrons**

Electron identification is defined for veto purposes. They are selected according to the following cut-based criteria listed in Table 4.4, utilising PF-based isolation.

Electrons are required to be identified at $|\eta| < 2.5$, with a minimum $p_T > 10$ GeV threshold to ensure that the electron falls within the tracking system of the detector.

Variable	Barrel	EndCap	Definition
$\Delta\eta_{In}$	<0.007	<0.009	$\Delta\eta$ between SuperCluster position and the coordinate of the associated track at the interaction vertex, assuming no radiation.
$\Delta\phi_{In}$	<0.15	<0.10	$\Delta\phi$ between SuperCluster position and track direction at interaction vertex extrapolated to ECAL assuming no radiation.
$\sigma_{i\eta i\eta}$	<0.01	<0.03	Cluster shape covariance, measure the η dispersion of the electrons electromagnetic shower over the ECAL supercluster.
H/E	<0.12	<0.10	The ratio of hadronic energy in the HCAL tower directly behind the ECAL super-cluster and the ECAL super-cluster itself.
d0 (vtx)	<0.02	<0.02	The tracker track transverse impact parameter w.r.t the primary vertex.
dZ (vtx)	<0.20	<0.20	The longitudinal distance of the tracker track w.r.t the primary vertex.
$\lvert(\frac{1}{E_{ECAL}} - \frac{1}{p_{track}})\rvert$	<0.05	<0.05	Comparison of energy at supercluster $1/E_{ECAL}$ and that of the track momentum at the vertex $1/p_{track}$. Causes suppression of fake electrons at low p_T.
PF Iso	<0.15	<0.15	Combined PF isolation of charged hadrons, photons, neutral hadrons within a $\Delta R < 0.3$ cone size. Isolation sum is corrected for pileup using effective area corrections for neutral particles.

Table 4.4.: Electron Identification criteria used within the analysis for veto purposes.

- **Noise and $\not{E}_T$ Filters**

  A series of Noise filters are applied to veto events which contain spurious non-physical jets that are not picked up by the jet id, and events which give large unphysical $\not{E}_T$ values. These filters are listed within Table 4.5.

Noise Filters Variable	Definition
CSC tight beam halo filter	As proton beams circle the LHC, proton interactions with the residual gas particles or the beam collimators can occur, producing showers of secondary particles which can interact with the CMS detector.
HBHE noise filter with isolated noise rejection	Anomalous noise in the HCAL not due to electronics noise, but rather due to instrumentation issues associated with the HPD's and Readout Boxes (RBXs).
HCAL laser filter	The HCAL uses laser pulses for monitoring the detector response. Some laser pulses have accidentally been fired in the physics orbit, and ended up polluting events recorded for physics analysis.
ECAL dead cell trigger primitive (TP) filter	EB and EE have single noisy crystals which are masked in reconstruction. Use the Trigger Primative (TP) information to assess how much energy was lost in masked cells.
Bad EE Supercrystal filter	Two supercrystals in EE are found to occasionally produce high amplitude anomalous pulses in several channels at once, causing a large $\not{E}_T$ spike.
ECAL Laser correction filter	A laser calibration multiplicative factor is applied to correct for transparency loss in each crystal during irradiation. A small number of crystals receive unphysically large values of this correction and become very energetic, resulting in $\not{E}_T$.

Table 4.5.: Noise filters that are applied to remove spurious and non-physical $\not{E}_T$ signatures within the CMS detector.

4.2.2. Event selection

The selection criteria for events within the analysis are detailed below. A set of common cuts are applied to both signal (maximise acceptance to a range of SUSY signatures), and control samples (retain similar jet kinematics for background predictions), with additional selection cuts applied to each control sample to enrich the sample in a particular EWK processes, see Section (4.2.3).

The jets considered in the analysis are required to have a transverse momentum $p_T > 50$ GeV, with a minimum of two jets required in the event. The highest E_T jet is required to lie within the central tracker acceptance $|\eta| < 2.5$, and the two leading p_T jets must each have $p_T > 100$ GeV. Any event which has a jet with $p_T > 50$ GeV that either fails the "loose" identification criteria described in Section(4.2.1) or has $|\eta| > 3.0$, is rejected. Similarly events in which an electron, muon or photon fails object identification but pass η and p_T restrictions, are identified as an "odd" lepton/photon and the event is vetoed.

At low H_T, the jet threshold requirements applied to be considered as part of the analysis and enter the H_T sum are scaled downwards. These are scaled down in order to extend phase space at low H_T, preserving similar jet multiplicities and background admixture seen at higher H_T, as listed in Table 4.6.

H_T bin	minimum jet p_T	second leading jet p_T
$275 < H_T < 325$	36.7	73.3
$325 < H_T < 375$	43.3	86.6
$375 < H_T$	50.0	100.0

Table 4.6.: Jet thresholds used in the three H_T regions of the analysis.

Within the signal region to suppress SM processes with genuine $\not\!\!E_T$ from neutrinos, events containing isolated electrons or muons are vetoed. Furthermore to ensure a pure multi-jet topology, events are vetoed if an isolated photon is found with $p_T > 25$ GeV.

An α_T requirement of > 0.55 is required to reduce the QCD multi-jet background to a negligible amount. Finally additional cleaning cuts are applied to protect against pathological deficiencies such as reconstruction failures or severe energy mis-measurements due to detector inefficiencies:

- Significant $\not\!\!H_T$ can arise in events with no real $\not\!\!E_T$ due to multiple jets falling below the p_T threshold for selecting jets. This in turn leads to events which can then incorrectly pass the α_T requirements of the analysis. This effect can be negated by requiring that the missing transverse momentum reconstructed from jets alone does not greatly exceed the missing transverse momentum reconstructed from all of the detector's calorimeter towers,

$$R_{miss} = \not\!\!H_T / \not\!\!E_T < 1.25.$$

- Fake $\not\!\!E_T$ and $\not\!\!H_T$ can arise due to significant jet mis-measurements cause by a small number of non-functioning ECAL regions. These regions absorb electromagnetic showers which are subsequently not added to the jet energy sum. To circumvent this problem the following procedure is employed : For each jet in the event, the angular separation

$$\Delta\phi_j^* \equiv \Delta\phi(p_j^{\rightarrow} - \sum_{i \neq j} p_i^{\rightarrow}), \tag{4.6}$$

is calculated where that jet is itself removed from the event. Here $\Delta\phi^*$ is a measure of how aligned the $\not{H}_T$ of an event is with a jet. A small value (i.e. the $\not{H}_T$ vector lies along the jet axis) is indicative of an inherently balanced event in which a jet has been mis-measured. For every jet in a event with $\Delta\phi^* < 0.5$, if the ΔR distance between the selected jet and the closest dead ECAL region is also < 0.3, then the event is rejected. Similarly events are rejected if the jet points within $\Delta R < 0.3$ of the ECAL barrel-endcap gap at $|\eta| = 1.5$.

Some of the key distributions of the data used in this analysis compared to MC simulation are shown in Figure 4.5. The MC samples are normalised to a luminosity of 11.7 fb^{-1}, with no requirement placed upon the number of b-tagged jets or number of jets in the events. In the case of this inclusive selection the dominant backgrounds in the signal regions are, Z $\rightarrow \nu\bar{\nu}$ and W + jet processes, with a smaller $t\bar{t}$ background accompanied by other residual backgrounds.

The distributions shown are presented for purely illustrative purposes, with the MC simulation itself not used in absolute term to estimate the yields from background processes, see Sections (4.2.3, 4.5). However it is nevertheless important to demonstrate that good agreement exists between simulation and observation in data.

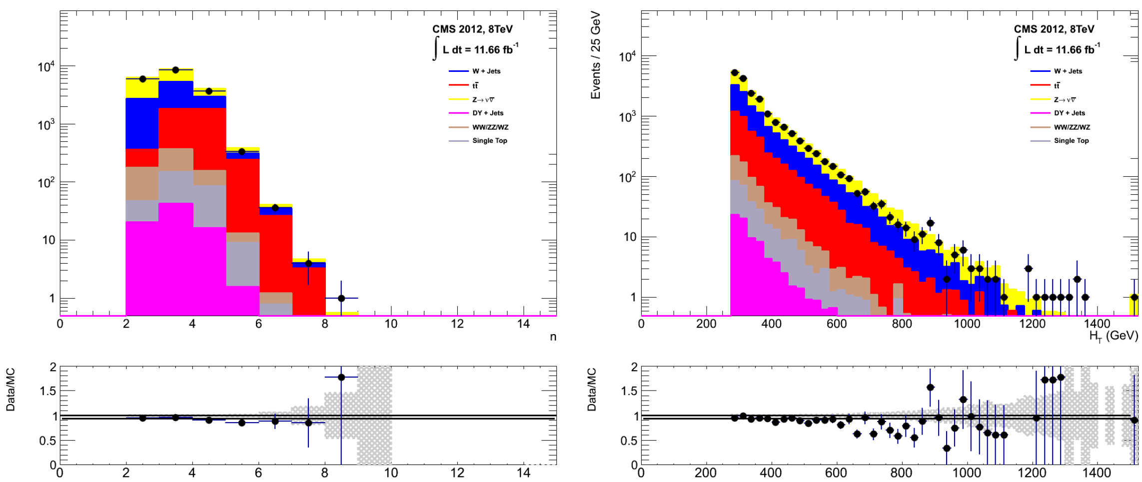

(a) Jet Multiplicity (b) H_T

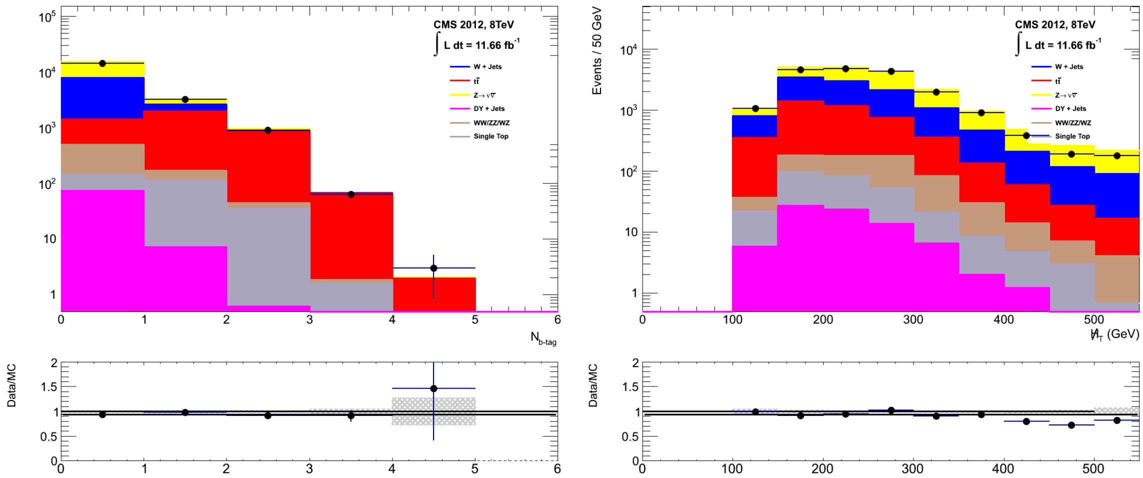

(c) Btag Multiplicity

(d) $\not{H}_T$

Figure 4.5.: Data/MC comparisons of key variables for the hadronic signal region,following the application of the hadronic selection criteria and the requirements of $H_T > 275$ GeV and $\alpha_T > 0.55$. Bands represent the uncertainties due to the statistical size of the MC samples. No requirement is made upon the number of b-tagged jets or jet multiplicity in these distributions.

4.2.3. Control sample definition and background estimation

The method used to estimate the background contributions in the hadronic signal region relies on the use of a Transfer Factor (TF). This is determined from MC simulation in both the control, $\mathrm{N}_{\mathrm{MC}}^{\mathrm{control}}$, and signal, $\mathrm{N}_{\mathrm{MC}}^{\mathrm{signal}}$, region to transform the observed yield measured in data for a control sample, $\mathrm{N}_{\mathrm{obs}}^{\mathrm{control}}$, into a background prediction, $\mathrm{N}_{\mathrm{pred}}^{\mathrm{signal}}$, via Equation (4.7),

$$\mathrm{N}_{\mathrm{pred}}^{\mathrm{signal}} = \frac{\mathrm{N}_{\mathrm{MC}}^{\mathrm{signal}}}{\mathrm{N}_{\mathrm{MC}}^{\mathrm{control}}} \times \mathrm{N}_{\mathrm{obs}}^{\mathrm{control}}. \tag{4.7}$$

All MC samples are normalised to the luminosity of the data samples, 11.7 fb^{-1}. Through this method, "vanilla" predictions for the SM background in the signal region can be made by considering separately the sum of the prediction from either the μ + jets and γ + jets, or μ + jets and $\mu\mu$ + jets samples. However the final background estimation from which results are interpreted, is calculated via a fitting procedure defined formally by the likelihood model described in Section (4.8).

The sum of the expected yields from all MC processes, in each control sample enter the denominator, $\mathrm{N}_{\mathrm{MC}}^{\mathrm{control}}$, of the TF defined in Eq (4.7). However for the numerator , $\mathrm{N}_{\mathrm{MC}}^{\mathrm{signal}}$, only the relevant processes that are being estimated, enter into the TF.

For the μ + jets sample the simulated MC processes which enter the numerator of the TF are,

$$\mathrm{N}_{\mathrm{MC}}^{\mathrm{signal}}(H_T, n_{\mathrm{jet}}) = N_W + N_{t\bar{t}} + N_{DY} + N_t + N_{di-boson}, \tag{4.8}$$

whilst for both the $\mu\mu$ + jets and γ + jets samples the only MC process used in the numerator is,

$$\mathrm{N}_{\mathrm{MC}}^{\mathrm{signal}}(H_T, n_{\mathrm{jet}}) = N_{Z\rightarrow\nu\bar{\nu}}. \tag{4.9}$$

The control samples and the EWK processes they are specifically tuned to select are defined below, with distributions of key variables for each of the control samples shown for illustrative purposes in Figures 4.6, 4.7 and 4.8. No requirement is placed upon the number of b-tagged jets or jet multiplicity in the distributions shown. The MC distributions highlight the background compositions of each control sample, where in general, good agreement is observed between data and simulation, giving confidence that the samples are well understood. The contribution from QCD multi-jet events is expected to be negligible :

The μ + jets control sample

Events from W + jets and $t\bar{t}$ processes enter into the hadronic signal sample due to unidentified leptons from acceptance effects or reconstruction inefficiencies and hadronic tau decays. These leptons originate from the decay of high p_T W bosons.

The control samples specifically identifies $W \rightarrow \mu\bar{\nu}$ decays within a similar phase-space of the signal region, where the muon is subsequently ignored in the calculation of event level variables, i.e. H_T, $\not{H}_T$, α_T. All kinematic jet-based cuts are identical to those applied in the hadronic search region (with the exception of α_T, discussed below) detailed in Section (4.2.2), with the same H_T, jet multiplicity and b-jet multiplicity binning described above.

– Muons originating from W boson decays are selected by requiring one tightly isolated muon defined in Table 4.2, with a $p_T > 30$ GeV and $|\eta| < 2.1$. Both of these threshold arise from trigger restrictions.

– The transverse mass of the W candidate must satisfy M_T $(\mu, \not\!\!E_T) > 30$ GeV (to suppress QCD multi-jet events).

– Events which contain a jet overlapping with a muon $\Delta\mathrm{R}(\mu, \mathrm{jet}) < 0.5$ are vetoed to remove events from muons produced as part of a jet's hadronisation process.

– Events containing a second muon candidate which has failed id, but passing p_T and $|\eta|$ requirements, are checked to have an invariant mass that satisfies $|M_{\mu\mu} - m_Z| > 25$, thus removing $Z \to \mu\mu$ contamination.

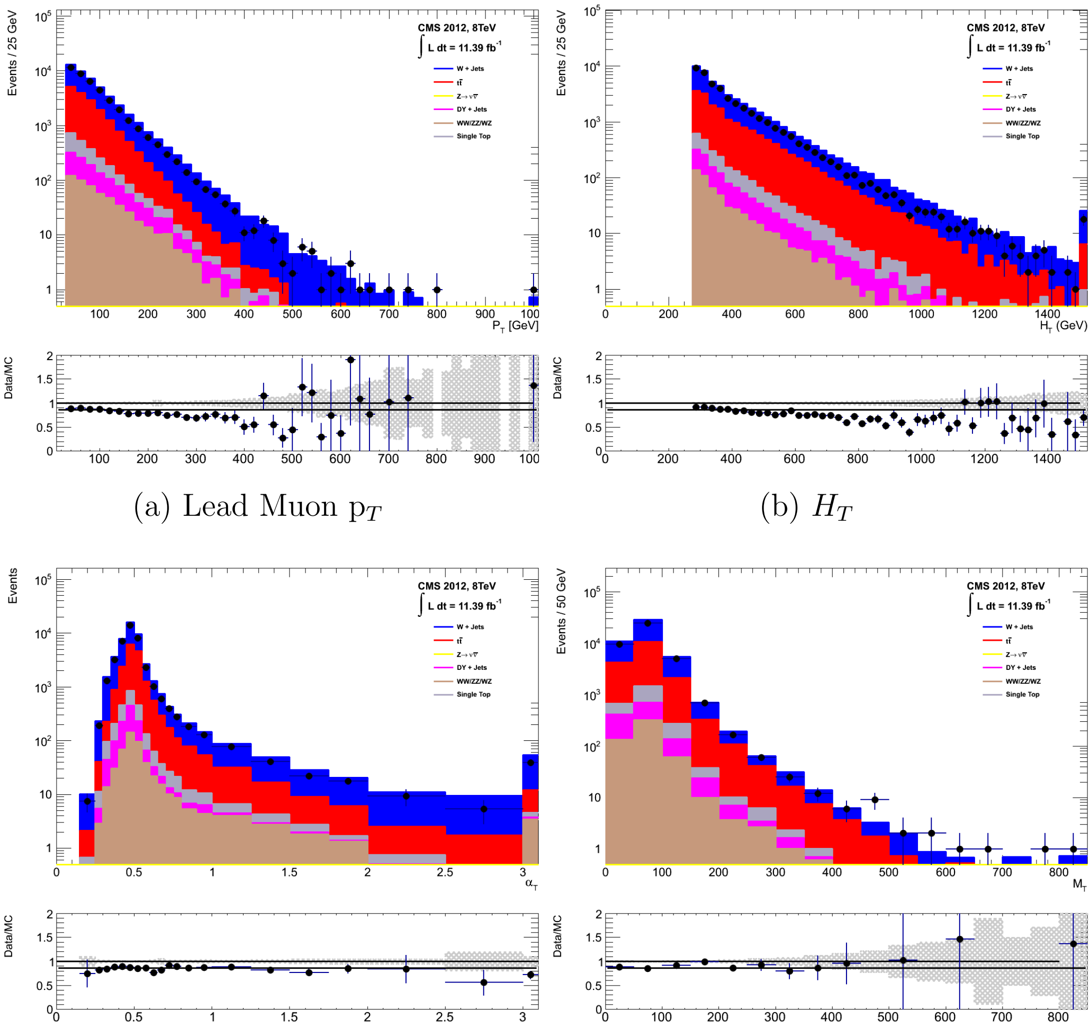

(a) Lead Muon p_T (b) H_T

(c) α_T (d) Transverse mass M_T

Figure 4.6.: Data/MC comparisons of key variables for the μ + jets selection,following the application of selection criteria and the requirements that $H_T > 275$ GeV. Bands represent the uncertainties due to the statistical size of the MC samples. No requirement is made upon the number of b-tagged jets or jet multiplicity in these distributions.

The $\mu\mu$ + jets control sample

The Z $\to \nu\bar{\nu}$ + jets background enters into the signal region from genuine $\not{E}_T$ from the escaping neutrinos. This background is estimated using two control samples, the first of which is the Z$\to$ $\mu\bar{\mu}$ + jets process, which posses identical kinematic properties, but with different acceptance and branching ratio [1].

The same acceptance requirements as the μ + jets selection for muons is applied, as defined in Table 4.2. Muons in the event are ignored for the purpose of the calculation of event level variables. Kinematic jet-based cuts and phase space binning identical to the hadronic search region are also applied.

- Muons origination from a Z boson decay are selected requiring exactly two tightly isolated muons. Due to trigger requirements the leading muon is required to have $p_T > 30$ GeV and $|\eta| < 2.1$. The requirement of the p_T on the second muon is relaxed to 10 GeV.
- Events are vetoed if containing a jet overlapping with a muon $\Delta R(\mu, \text{jet}) < 0.5$.
- In order to specifically select two muons both originating from a single Z boson decay, the invariant mass of the two muons must satisfy $|M_{\mu\mu} - m_Z| < 25$.

The $\mu\mu$ + jets sample is used to make predictions in the signal region in the two lowest H_T bins, providing coverage where the γ + jets sample is unable to, due to trigger requirements. In higher H_T bins, the higher statistics of the γ + jets sample is also used in determining the Z $\rightarrow \nu\bar{\nu}$ estimation.

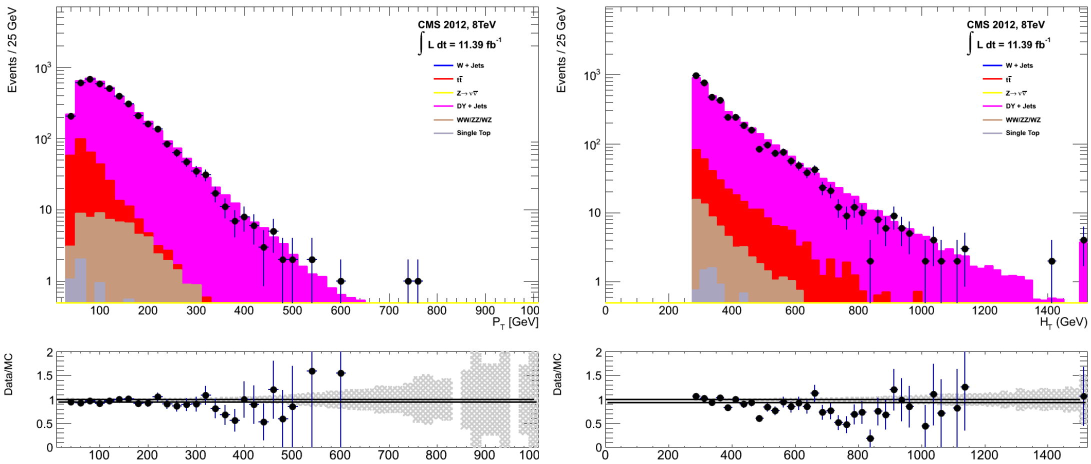

(a) Lead Muon p_T (b) H_T

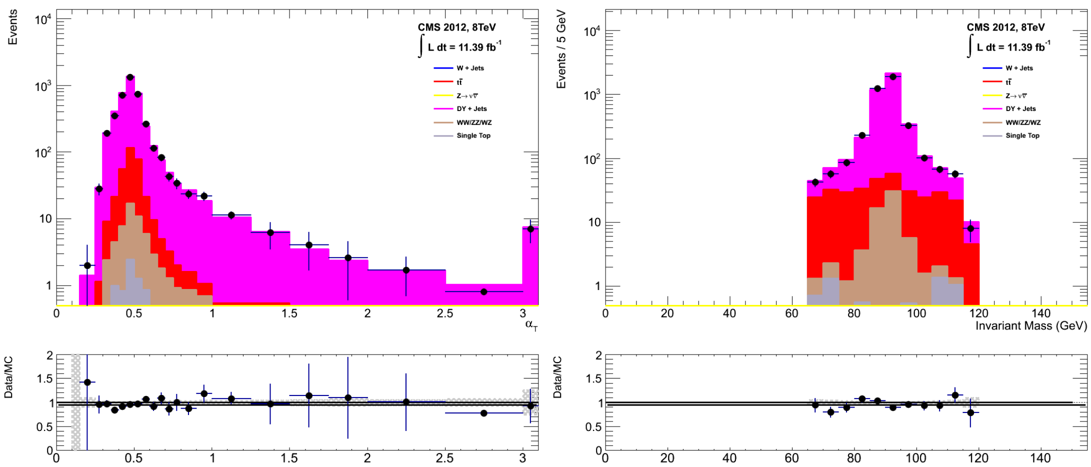

(c) α_T (d) $\mu\mu$ invariant mass

Figure 4.7.: Data/MC comparisons of key variables for the $\mu\mu$ + jets selection,following the application of selection criteria and the requirements that $H_T > 275$ GeV. Bands represent the uncertainties due to the statistical size of the MC samples. No requirement is made upon the number of b-tagged jets or jet multiplicity in these distributions.

The γ + jets control sample

The Z $\rightarrow \nu\bar{\nu}$ + jets background is also estimated from a γ + jets control sample. When the E_T of the photon is greater than the mass of the Z, it possesses a larger cross section and kinematic properties similar to those of Z$\rightarrow \mu\bar{\mu}$ events where the photon is ignored [79]. The photon is ignored for the purpose of the calculation of event level variables, and identical selection cuts to the hadronic signal region are applied.

- Exactly one photon is selected, satisfying identification criteria as detailed in Table 4.3, with a minimum p_T >165 GeV to satisfy trigger thresholds and $|\eta|$ < 1.45 to ensure the photon remains in the barrel of the detector.

- A selection criteria of $\Delta R(\gamma, jet) < 1.0$, between the photon and all jets is applied to ensure the acceptance of only well isolated γ + jets events.

- Given that the photon is ignored, this control sample can only be applied in the H_T region > 375 GeV, due to the trigger thresholds on the minimum p_T of the photon, and the $\not{H}_T$ requirement of an $\alpha_T > 0.55$ cut from Equation (4.5), which is maintained in this control sample due to contamination from QCD in the absence of an α_T cut.

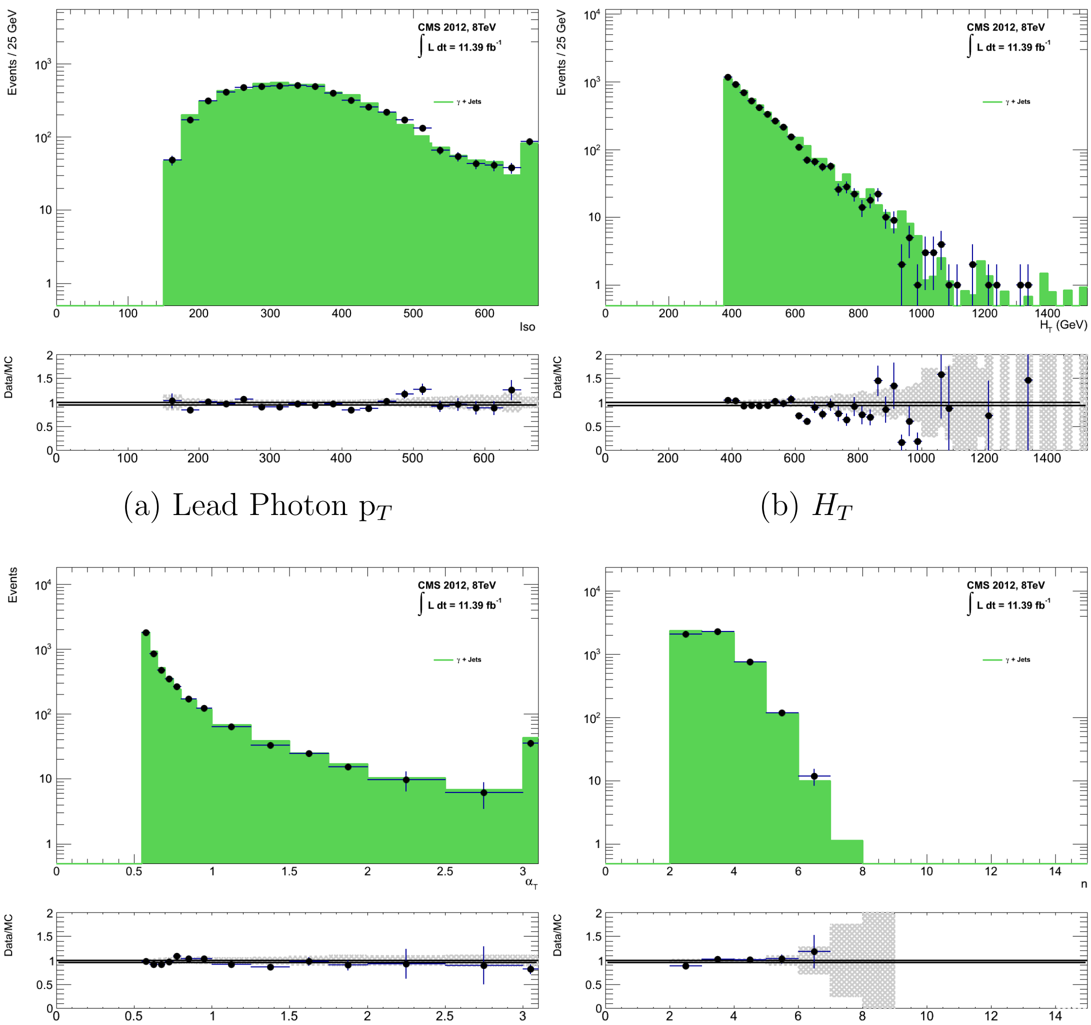

(a) Lead Photon p_T (b) H_T

(c) α_T (d) Jet multiplicity

Figure 4.8.: Data/MC comparisons of key variables for the γ + jets selection,following the application of selection criteria and the requirements that $H_T > 375$ GeV and $\alpha_T > 0.55$. Bands represent the uncertainties due to the statistical size of the MC samples. No requirement is made upon the number of b-tagged jets or jet multiplicity in these distributions.

The selection criteria of the three control samples are defined to ensure background composition and event kinematics mirror closely the signal region. This is done in order to minimise the reliance on MC simulation to model correctly the backgrounds and event kinematics in the control and signal samples.

However in the case of the μ + jets and $\mu\mu$ + jets samples, the α_T requirement is relaxed in the selection criteria of these samples. This is made possible as contamination from QCD multi-jet events is suppressed to a negligible level by the other kinematic selection criteria within the two control samples, to select pure EWK processes. Thus in this way, the acceptance of the two muon control samples can be significantly increased, which simultaneously improves their predictive power and further reduces the effect of any potential signal contamination.

The modelling of the α_T variable is probed through a dedicated set of closure tests, described in Section (4.6), which demonstrate that the different α_T acceptances for the control and signal samples have no significant systematic bias on the prediction.

4.2.4. Estimating the QCD multi-jet background

A negligible background from QCD multi-jet events within the hadronic signal region is expected due to the selection requirement, and additional cleaning filters applied. However a conservative approach is still adopted and the likelihood model, see Section (4.8.2), is given the freedom to accommodate any potential QCD multi-jet contamination.

Any potential contamination can be identified through the variable R_{α_T}, defined as the ratio of events above and below the α_T threshold value used in the analysis. This is modelled by a H_T dependant falling exponential function which takes the form,

$$R_{\alpha_T}(H_T) = A_{\text{QCD}} \exp^{-k_{QCD} H_T}, \tag{4.10}$$

where the parameters A_{QCD} and k_{QCD} are the normalisation and exponential decay constants respectively.

For QCD event topologies this exponential behaviour is expected as a function of H_T for several reasons. The improvement of jet energy resolution at higher H_T due to higher p_T jets leads to a narrower peaked distribution, causing R_{α_T} to fall. Similarly at higher H_T values > 375 GeV, the jet multiplicity rises slowly with H_T. As shown in Figure 4.3, at higher jet multiplicities, the result of the combinatorics used in the determination of α_T, then leads to a narrower distribution.

The value of the decay constant k_{QCD} is constrained via measurements within data sidebands to the signal region. This is also done to validate the falling exponential assumption for QCD multi-jet topologies. The sidebands are enriched in QCD multi-jet background and defined as regions where α_T is relaxed or that the R_{miss} cut is inverted.

Figure 4.9 depicts the definition of these data sidebands used to constrain the value of k_{QCD}.

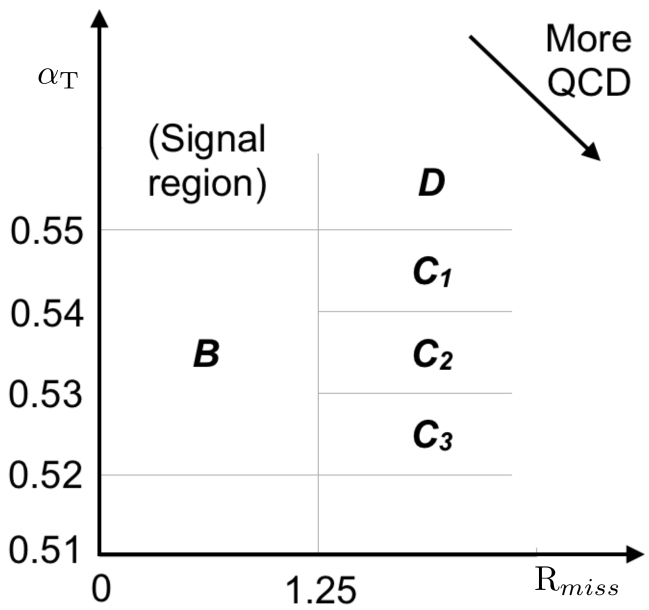

Figure 4.9.: QCD sideband regions, used for determination of k_{QCD}.

The fits to determine the value of k_{QCD} are shown in Appendix (C.1), for which the best fit value obtained from sideband region B is determined to be $k_{\mathrm{QCD}} = 2.96 \pm 0.64 \times 10^{-2}$ GeV $^{-1}$.

The best fit values of the remaining three C sideband regions are used to estimate the systematic uncertainty on the central value obtained from sideband region B. The variation of these measured values is used to determine the error on the determined central value, and is calculated to be $1.31 \pm 0.26 \times 10^{-2}$ GeV^{-1}. This relative error of $\sim$ 20% gives an estimate of the systematic uncertainty of the measurement to be applied to k_{QCD}.

Finally the same procedure is performed for sideband region D as an independent cross check, to establish that the value of k_{QCD} extracted from a lower α_T slice, can be applied to the signal region $\alpha_T > 0.55$. The likelihood fit is performed across all H_T bins within the QCD enriched region with no constraint applied to k_{QCD}. The resulting best fit value for k_{QCD} shows good agreement between that and the weighted mean determined from the three C sidebands regions. This demonstrates that the assumption of using the central value determined from sideband region B, to provide an unbiased estimator for k_{QCD} in the signal region ($\alpha_T > 0.55$) is valid.

Table 4.7, summarises the best fit k_{QCD} values determined for each of the sideband regions to the signal region.

Sideband region	$k_{\mathrm{QCD}}(\times 10^{-2} GeV^{-1})$	$p-$value
B	2.96 $\pm$ 0.64	0.24
C_1	1.19 $\pm$ 0.45	0.93
C_2	1.47 $\pm$ 0.37	0.42
C_3	1.17 $\pm$ 0.55	0.98
C(weighted mean)	1.31 $\pm$ 0.26	-
D(likelihood fit)	1.31 $\pm$ 0.09	0.57

Table 4.7.: Best fit values for the parameters k_{QCD} obtained from sideband regions B,C_1,C_2,C_3. The weighted mean is determined from the three measurements made within sideband region C. The maximum likelihood value of k_{QCD} given by the simultaneous fit using sideband region D. Quotes errors are statistical only.

4.3. Trigger Strategy

A cross trigger based on the H_T and α_T values of an event, is used with varying thresholds across H_T bins to record the events used in the hadronic signal region. The α_T legs of the `HT_alphaT` triggers used in the analysis are chosen to suppress QCD multi-jet events and control trigger rate, whilst maintaining signal acceptance. To further maintain an acceptable rate for these analysis specific triggers, only calorimeter information is used in the reconstruction of the H_T sum, leading to the necessity for Calo jets to be used within the analysis.

A single object prescaled `HT` trigger is used to collect events for the hadronic control region described above in Section (4.2.4).

The performance of the α_T and H_T triggers used to collect data for the signal and hadronic control region is measured with respect to a reference sample collected using the muon system. This allows measurement of both the Level 1 seed and higher level triggers simultaneously, as the reference sample is collected independent of any jet requirements.

The selection for the trigger efficiency measurement is identical to that described in Section (4.2.2), with the requirement of exactly one well identified muon with $p_T > 30$ GeV which is subsequently ignored.

The efficiencies measured for the `HT_alphaT` triggers in bins individual H_T and α_T legs, is summarised in Table 4.8.

H_T range (GeV)	ϵ on H_T leg (%)	ϵ on α_T leg (%)
275-325	$87.7^{+1.9}_{-1.9}$	$82.8^{+1.0}_{-1.1}$
325-375	$90.6^{+2.9}_{-2.9}$	$95.9^{+0.7}_{-0.9}$
375-475	$95.7^{+0.1}_{-0.1}$	$98.5^{+0.5}_{-0.9}$
475-∞	$100.0^{+0.0}_{-0.0}$	$100.0^{+0.0}_{-4.8}$

Table 4.8.: Measured efficiencies of the H_T and α_T legs of the `HT` and `HT_alphaT` triggers in independent analysis bins. The product of the two legs gives the total efficiency of the trigger in a given offline H_T bin.

Data for the control samples of the analysis, detailed in Section (4.2.3), are collected using single object photon trigger for the γ + jets sample, and a single object muon trigger for both the μ + jets and $\mu\mu$ + jets control samples.

The photon trigger is measured to be full efficient for the threshold ${p_T}^{\text{photon}} > 150$ GeV, whilst the single muon efficiency satisfying ${p_T}^{\text{muon}} > 30$ GeV is measured to have an efficiency of $(88 \pm 2)\%$ that is independent of H_T. In the case of the $\mu\mu$ + jets control sample, the efficiency is measured to be $(95 \pm 2)\%$ for the lowest H_T bin, rising (due to the average p_T of the second muon in the event increasing at larger H_T) to $(98 \pm 2)\%$ for the highest H_T bin.

4.4. Measuring MC Normalisation Factors via H_T Sidebands

The theoretical cross sections of different SM processes at Next to Next Leading Order (NNLO) and the number of MC simulated events generated for that particular process, is typically used to determine the appropriate normalisation for a MC sample. However within the particular high-H_T and high-$\not\!\!E_T$ corners of kinematic phase space probed within this search, the theoretical cross sections for various processes are far less well understood.

To mitigate the problem of theoretical uncertainties and arbitrary choices of cross sections, the normalisation of MC samples used in the analysis are determined through the use data sidebands. The sidebands are used to calculated sample specific correction factors (k-factors) that are appropriate for the H_T-$\not\!\!E_T$ phase space covered by this analysis.

They are defined within the μ + jets and $\mu\mu$ + jets control sample, by the region $200 < H_T < 275$, using the same jet p_T thresholds as the adjacent first analysis bin. Individual

EWK processes are isolated within each of these control samples via requirements on jet multiplicity and the requirement on b-tags, summarised in Table 4.9. The purity of the samples are typically > 90% with any residual contamination corrected for. The resultant k-factor for each process is determined by then taking ratio of the data yield over the MC expectation in the sideband. Subsequently these k-factors are then applied to the processes within the phase space of the analysis.

Process	Selection	Observation	MC expectation	k-factor
W + jets	μ + jets, n_b=0, n_{jet} = 2,3	26950	29993.2 $\pm$ 650.1	0.90 $\pm$ 0.02
$Z \rightarrow \mu\mu$ + jets	$\mu\mu$ + jets, n_b=0, n_{jet} = 2,3	3141	3402.0 $\pm$ 43.9	0.92 $\pm$ 0.02
$t\bar{t}$	μ + jets, n_b=2, n_{jet} = $\geq$4	2190	1967.8 $\pm$ 25.1	1.11 $\pm$ 0.02

Table 4.9.: k-factors calculated for different EWK processes. All k-factors are derived relative to theoretical cross sections calculated in NNLO. The k-factors measured for the Z$\rightarrow \mu\mu$ + jets processes, are also applied to the Z $\rightarrow \nu\bar{\nu}$ + jets and γ + jets MC samples.

It is worth pointing out that these correction factors have a negligible effect when providing a background estimation for the signal region. The TF's used in the analysis are found to be unaffected by application of these k-factors due to the similarity in the background composition of the control and signal regions. However when systematic uncertainties are determined in Section (4.6), the closure tests performed are sensitive to these corrections when extrapolations between different n_b^{reco} and n_{jet} categories are performed.

4.5. Determining MC Simulation Yields with Higher Statistical Precision

Reconstructing events from EWK processes with many b-tagged jets ($\geq$3), $n_{\mathrm{b}}^{\mathrm{reco}}$,is largely driven by the mis-tagging of light jets within the event. This is clear when considering the main EWK backgrounds in the analysis, such as $t\bar{t}$ + jets events, which typically contain two b-flavoured jets from the decay of the top quarks, whilst W + jets and Z$\rightarrow \mu\mu$ + jets events will typically contain no b-flavoured jets.

When the expectation for the number of $n_{\mathrm{b}}^{\mathrm{reco}}$ is taken directly from simulation, the statistical uncertainty at large b-tag multiplicities becomes relatively large. In order to reduce this uncertainty one approach is to use the information encoded throughout all events in the simulation sample, to measure each of the four ingredients:

1. the b-tagging efficiency in the event selection,
2. the charm-tagging efficiency in the event selection
3. the mis-tagging rate in the event selection,
4. the underlying flavour distribution of the jets in the events,

that determine the $n_{\mathrm{b}}^{\mathrm{reco}}$ distribution of the process being measured. This method allows the determination of higher b-tag multiplicities to a higher degree of accuracy reducing the statistical uncertainties of the MC which enter into the TF's. For the discussion that follows, these predictions are determined on average (i.e not on an event-by-event basis), and is known as the formula method.

4.5.1. The formula method

The assigning of jet flavours to reconstruction level jets in simulation is achieved via an algorithmic method defined as:

- Try to find the parton that most likely determines the properties of the jet and assign that flavour as true flavour,
- "final state" partons (after showering, radiation) are analysed (also within $\Delta R <$ 0.3 of reconstructed jet cone),
- If there is a b/c flavoured parton within the jet cone: label as b/c flavoured jet,
- Otherwise: assign flavour of the hardest parton.

This process is employed within each individual MC process and independently for each H_T- n_{jet} bin in the analysis. The $n_{\mathrm{b}}^{\mathrm{reco}}$ distribution is then constructed in the following way:

Let $N(n_b^{gen}, n_c^{gen}, n_q^{gen})$ represent the yield in simulation, of events with b underlying b-quarks, c underlying c-quarks and q underlying light quarks which are matched to reconstructed jets as detailed above. Light quarks defined as those which originate from a u, d, s, g and τ jets, which having similar mis-tagging rates are grouped together. Similarly ϵ, β and m represent the measured b-tagging, c-tagging and mis-tagging efficiency averaged over all the jets within that particular analysis bin.

Using this information the expected n_b^{reco} distribution can be analytically calculated using the formula :

$$N(n) = \sum_{n_b^{gen}+n_c^{gen}+n_q^{gen}=n_{\mathrm{jet}}^{cat}} \; \sum_{n_b^{tag}+n_c^{tag}+n_q^{tag}=n} N(n_b^{gen}, n_c^{gen}, n_q^{gen}) \times P(n_b^{tag}, n_b^{gen}, \epsilon) \times$$
$$P(n_c^{tag}, n_c^{gen}, \beta) \times P(n_q^{tag}, n_q^{gen}, m), \tag{4.11}$$

with N(n) representing the number of n b-tagged jets in a particular analysis bin as determined by the formula method.

The variables $n_{b/c/q}^{tag}$ signify the number of times that a particular jet flavour results in a b-tagged jet, of which the sum of the three terms must equal the number of n b-tagged jets being estimated. Similarly $n_{b/c/q}^{gen}$ represent the flavour admixture of the jets, which having been identified using the above technique as b, c or light flavoured jets, are required by definition that the sum of the three to fall within the n_{jet} category being analysed.

Finally $P(n_b^{tag}, n_b^{gen}, \epsilon)$, $P(n_c^{tag}, n_c^{gen}, \beta)$ and $P(n_q^{tag}, n_q^{gen}, m)$ correspond to the binomial probabilities for that particular jet flavour and tagging configuration to occur based on the measured tagging efficiencies (ϵ, β and m) for each jet flavour. This formula is enacted over all five of the analysis b-tag categories to build up the resultant $n_{\mathrm{b}}^{\mathrm{reco}}$ distribution for each process in turn.

This approach ultimately results in a more precise $n_{\mathrm{b}}^{\mathrm{reco}}$ distribution prediction, due to the utilisation of the entire MC sample in extracting the estimated underlying n_b^{reco} distribution, particularly at higher $n_{\mathrm{b}}^{\mathrm{reco}}$ multiplicities where a lack of events in simulation can lead to relatively large statistical uncertainties.

4.5.2. Establishing proof of principle

In order to validate the procedure, the predictions obtained from the formula method summarised in Equation (4.11), are compared directly to those obtained directly from simulation. Resultantly no simulation to data correction factors are applied when making this comparison

This sanity check for the μ + jets control sample is presented in Table 4.10, for all n_b^{reco} and H_T bins with no requirement placed upon the jet multiplicity of the events.

H_T Bin (GeV)	275–325	325–375	375–475	475–575
Formula $n_b = 0$	12632.66 ± 195.48	6696.08 ± 82.59	6368.96 ± 75.34	2906.27 ± 39.65
Vanilla $n_b = 0$	12612.95 ± 198.68	6687.97 ± 83.78	6359.27 ± 76.50	2898.27 ± 36.89
Formula $n_b = 1$	4068.09 ± 45.71	2272.76 ± 26.14	2181.32 ± 25.07	1089.14 ± 13.82
Vanilla $n_b = 1$	4067.73 ± 60.30	2268.02 ± 30.20	2180.69 ± 28.73	1094.37 ± 24.14
Formula $n_b = 2$	1963.71 ± 22.44	1087.55 ± 13.57	1055.57 ± 13.25	554.96 ± 7.95
Vanilla $n_b = 2$	1984.53 ± 26.19	1094.43 ± 16.67	1068.96 ± 16.36	558.14 ± 10.51
Formula $n_b = 3$	146.94 ± 2.07	79.97 ± 1.37	78.05 ± 1.35	49.84 ± 1.03
Vanilla $n_b = 3$	149.52 ± 4.84	85.98 ± 3.64	74.45 ± 3.29	49.54 ± 2.68
Formula $n_b \geq 4$	2.26 ± 0.12	1.29 ± 0.10	5.32 ± 0.20	-
Vanilla $n_b \geq 4$	1.84 ± 0.50	1.02 ± 0.39	4.86 ± 0.83	-

H_T Bin (GeV)	575–675	675–775	775–875	>875
Formula $n_b = 0$	1315.68 ± 19.49	640.49 ± 11.90	327.81 ± 7.91	424.27 ± 9.27
Vanilla $n_b = 0$	1315.23 ± 20.20	641.96 ± 12.48	329.09 ± 8.36	424.02 ± 9.73
Formula $n_b = 1$	490.41 ± 7.45	226.95 ± 4.42	109.91 ± 2.84	129.97 ± 3.07
Vanilla $n_b = 1$	490.52 ± 9.92	222.22 ± 6.21	107.46 ± 4.15	129.64 ± 4.64
Formula $n_b = 2$	256.75 ± 4.58	113.45 ± 2.70	52.10 ± 1.69	59.29 ± 1.78
Vanilla $n_b = 2$	253.43 ± 6.52	117.17 ± 4.27	52.70 ± 2.80	59.45 ± 3.00
Formula $n_b = 3$	25.66 ± 0.69	12.48 ± 0.46	5.52 ± 0.31	6.83 ± 0.33
Vanilla $n_b = 3$	29.18 ± 2.06	11.77 ± 1.26	6.18 ± 0.95	7.53 ± 1.05

Table 4.10.: Comparing yields in simulation within the μ + jets selection determined from the formula method described in Equation (4.11), and that taken directly from simulation . The numbers are normalised to 11.4fb^{-1}. No simulation to data corrections are applied.

It can be seen as expected, that there is good consistency between the results determined via the formula method and 'raw' simulation yields. Similarly the power of this approach can be seen in the reduction of this statistical error in the prediction across all H_T and n_b^{reco} bins. In particular the statistical uncertainty is reduced by several factors in the highest $n_b^{reco} \geq 4$ category.

4.5.3. Correcting measured efficiencies in simulation to data

As detailed in Section (3.3.2), it is necessary for certain p_T and η dependant corrections, to be applied to both the b-tagging efficiency and mis-tagging rates in order correct the efficiencies from simulation to the distributions seen in data. These corrections factors are considered when determining the simulation yields for each selection, which are used to construct the TF's of the analysis.

Each of the corrections factors for the b, c and light flavoured jets come with an associated systematic uncertainty. The uncertainties across different jet p_T and η bins, are considered as fully correlated. When computing the magnitude of the effect of this systematic uncertainty on the TF's of the analysis, the scale factors are therefore scaled up/down simultaneously within each H_T bin of the analysis for all of the $SF_{\mathrm{b,\,c,\,light}}$ scale factors. The magnitude of this correction is shown for each H_T bin within Figure 4.10.

Varying the scale factor corrections by their systematic uncertainty will change the absolute yields within each n_b^{reco} bin of all selections. However, ultimately it is the change in the TF's which influences the final background prediction from each of the control samples. The magnitude of the absolute change in each TF, constructed from when the μ + jets control sample is used to predict the entire hadronic signal region background, is shown in Table 4.11,.

It can be seen that the TF's are found to be relatively insensitive to the systematic uncertainty of the b-tag scale factors (showing typically less than $\sim$2% change). This can be accounted for by the similar composition of the signal and control sample backgrounds, such that any change in the underlying n_b^{reco} distribution will be reflected in both signal and control regions and cancel out in the TF.

Any overall systematic effect on the overall background prediction of the analysis from these b-tag scale factor uncertainties is incorporated within the data driven systematics introduced in the following section.

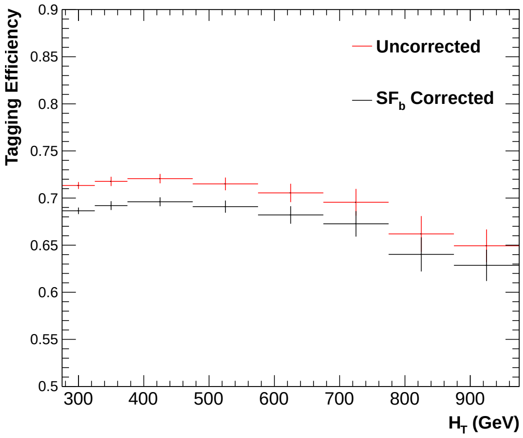

(a) b-jets

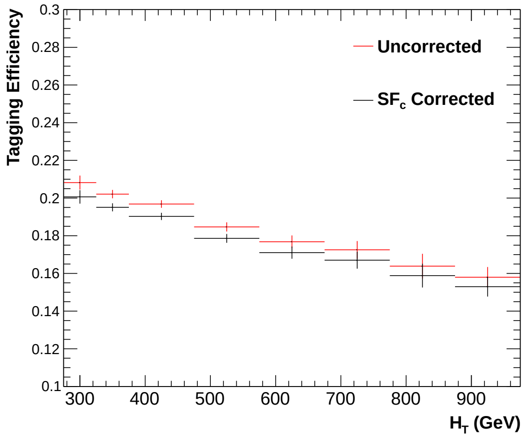

(b) c-jets

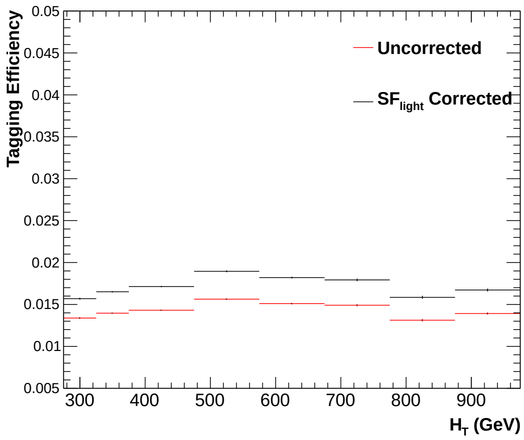

(c) light-jets

Figure 4.10.: Tagging efficiencies of (a) b-jets, (b) c-jets, and (c) light-jets as a function all jets within each individual analysis H_T bin. Efficiencies measured directly from simulation (black) and with data to simulation $SF_{b,c,light}$ correction factors (red) are applied.

n_b^{reco}	275–325	325–375	375–475	475–575
$= 0$	$0.557\ ^{+0.001}_{-0.001}\ \pm\ 0.012$	$0.495\ ^{+0.001}_{-0.001}\ \pm\ 0.009$	$0.383\ ^{+0.001}_{-0.001}\ \pm\ 0.005$	$0.307\ ^{+0.001}_{-0.002}\ \pm\ 0.006$
$= 1$	$0.374\ ^{+0.006}_{-0.006}\ \pm\ 0.006$	$0.320\ ^{+0.006}_{-0.005}\ \pm\ 0.005$	$0.251\ ^{+0.005}_{-0.005}\ \pm\ 0.004$	$0.185\ ^{+0.003}_{-0.003}\ \pm\ 0.004$
$= 2$	$0.226\ ^{+0.002}_{-0.002}\ \pm\ 0.004$	$0.201\ ^{+0.001}_{-0.002}\ \pm\ 0.004$	$0.159\ ^{+0.001}_{-0.001}\ \pm\ 0.004$	$0.134\ ^{+0.000}_{-0.001}\ \pm\ 0.004$
$= 3$	$0.221\ ^{+0.002}_{-0.002}\ \pm\ 0.005$	$0.208\ ^{+0.002}_{-0.001}\ \pm\ 0.007$	$0.164\ ^{+0.001}_{-0.000}\ \pm\ 0.006$	$0.144\ ^{+0.001}_{-0.001}\ \pm\ 0.007$
≥ 4	$0.222\ ^{+0.004}_{-0.005}\ \pm\ 0.015$	$0.248\ ^{+0.003}_{-0.003}\ \pm\ 0.035$	$0.123\ ^{+0.002}_{-0.003}\ \pm\ 0.009$	-

	575–675	675–775	775–875	≥875
$= 0$	$0.263\ ^{+0.001}_{-0.002}\ \pm\ 0.006$	$0.215\ ^{+0.000}_{-0.001}\ \pm\ 0.007$	$0.171\ ^{+0.000}_{-0.001}\ \pm\ 0.009$	$0.111\ ^{+0.000}_{-0.001}\ \pm\ 0.006$
$= 1$	$0.154\ ^{+0.003}_{-0.003}\ \pm\ 0.005$	$0.138\ ^{+0.003}_{-0.004}\ \pm\ 0.006$	$0.121\ ^{+0.005}_{-0.005}\ \pm\ 0.007$	$0.091\ ^{+0.002}_{-0.002}\ \pm\ 0.006$
$= 2$	$0.104\ ^{+0.000}_{-0.001}\ \pm\ 0.005$	$0.079\ ^{+0.001}_{-0.001}\ \pm\ 0.006$	$0.063\ ^{+0.001}_{-0.002}\ \pm\ 0.007$	$0.071\ ^{+0.000}_{-0.000}\ \pm\ 0.008$
$= 3$	$0.116\ ^{+0.001}_{-0.001}\ \pm\ 0.009$	$0.069\ ^{+0.001}_{-0.001}\ \pm\ 0.007$	$0.079\ ^{+0.001}_{-0.001}\ \pm\ 0.017$	$0.095\ ^{+0.003}_{-0.002}\ \pm\ 0.020$

Table 4.11.: The absolute change in the TF's used to predict the entire signal region SM background, using the μ + jets control sample when the systematic uncertainties of the data to simulation scale factors are varied by $\pm 1\sigma$. The impact of the change is shown for each H_T and n_b^{reco} bin with no requirement made on the jet multiplicity of the events. (Also quoted are the statistical uncertainties)

4.6. Systematic Uncertainties on Transfer Factors

Since the TF's used to establish the background prediction are obtained from simulation, an appropriate systematic uncertainty is assigned to each factor to account for theoretical uncertainties [80] and limitations in the simulation modelling of event kinematics and instrumental effects.

The magnitudes of these systematic uncertainties are established through a set of data driven method, in which the three independent control samples of the analysis (μ + jets, $\mu\mu$ + jets, γ + jets) are used to in a series of closure tests. The yields from one of these control samples, along with the corresponding TF obtained from simulation, are used to predict the yields in another control sample, using the same method of establishing a background prediction for the signal region as described in Section (4.2.3).

The level of agreement between the predicted and observed yields is expressed as the ratio

$$\frac{(N_{\text{obs}} - N_{\text{pred}})}{N_{\text{pred}}}, \tag{4.12}$$

while considering only the statistical uncertainties on N_{pred}, the prediction, and N_{obs}, the observation. No systematic uncertainty is assigned to the prediction, and resultantly the level of closure is defined by the statistical significance of a deviation from the ratio from zero.

This ratio is measured for each H_T bin in the analysis, allowing these closure tests to be sensitive to both the presence of any significant biases or any possible H_T dependence on the level of closure.

Eight sets of closure tests are defined between the three data control samples, conducted independently between the two jet multiplicity ($2 \leq n_{\text{jet}} \leq 3$, $n_{\text{jet}} \geq 4$) bins. Each of these tests are specifically chosen to probe each of the different key ingredients of the simulation modelling that can affect the background prediction.

Each of the different modelling components and the relevant closure tests are described below :

α_T modelling

The modelling of the α_T distribution in genuine $\not{E}_T$ events is probed with the μ + jets control sample. This test is important to verify the approach of remove the α_T > 0.55 requirement from the μ + jets and $\mu\mu$ + jets samples to increase the precision of the background prediction. The test uses the μ + jets sample without an α_T cut to make a prediction into the μ + jets sample defined with the requirement $\alpha_T >$ 0.55.

Background admixture

The sensitivity of the translation factors to the relative admixture of events from $W+$ jets and $t\bar{t}$ processes is probed by two closure tests. These tests represent an extremely conservative approach as the admixture of the background remains similar between the μ + jets sample and the signal region, contrary to the defined closure tests which make predictions between two very different admixtures of $W+$ jets and $t\bar{t}$ events.

Within the μ + jets sample, a W boson enriched sub-sample ($n_b = 0$) is used to predict yields in a $t\bar{t}$ enriched sub-sample ($n_b = 1$). Similarly the $t\bar{t}$ enriched sub-sample (n_b =1) is also used to predict yields for a further enriched $t\bar{t}$ sub-sample ($n_b = 2$), further probing the modelling of the $n_{\mathrm{b}}^{\mathrm{reco}}$ distribution.

Similarly a further closure test probes the relative contribution of $Z+$ jets to $W+$jets and $t\bar{t}$ events, through the use of the μ + jets sample to predict yields for the $\mu\mu$ + jets control sample. This closure test, also at some level probes the muon trigger and reconstruction efficiencies, given that exactly one or two muons are required by the different selections.

Consistency check between Z $\to \nu\bar{\nu}$ predictions

An important consistency check between the $\mu\mu$ + jets jets and γ + jets, which are both used in the prediction of the Z $\to \nu\bar{\nu}$ in the signal region. This is conducted by using the γ + jets sample to predict yields for the $\mu\mu$ + jets control sample. Using γ + jets processes as a method to predict Z + jet processes is subject to theory uncertainties [81], which can be probed by this data driven closure test within a $Z \to \mu\mu$ control sample.

Modelling of jet multiplicity

The simulation modelling of the jet multiplicity within each control sample is important due to the exclusive jet multiplicity binning within the analysis. This is probed via the use of each of the three control samples to independently predict from the lower jet multiplicity category $2 \leq n_{\mathrm{jet}} \leq 3$, to the high jet category $n_{\mathrm{jet}} \geq 4$.

For the case of the μ + jets and $\mu\mu$ + jets control samples this test this is also a further probe of the admixture between $W+$ jets/$Z+$ jets and $t\bar{t}$.

To test for the assumption that no H_T dependences exist within the background predictions of the analysis, the first five closure tests defined above are used, with zeroeth and first order polynomial fits are applied to each test individually. This is summarised in Table 4.12 and Table 4.13 which show the results for both the $2 \leq n_{jet} \leq 3$ and ≥ 4 jet multiplicity bins respectively.

		Constant fit		Linear fit	
Closure test	Symbol	Best fit value	p-value	Slope (10^{-4})	p-value
$\alpha_T < 0.55 \rightarrow \alpha_T > 0.55$ (μ + jets)	Circle	-0.06 ± 0.02	0.93	-1.3 ± 2.2	0.91
0 b-jets $\rightarrow$ 1 b-jet (μ + jets)	Square	0.07 ± 0.02	0.98	-1.6 ± 1.6	1.00
1 b-jets $\rightarrow$ 2 b-jet (μ + jets)	Triangle	-0.07 ± 0.03	0.76	-2.7 ± 3.0	0.76
μ + jets $\rightarrow$ $\mu\mu$ + jets	Cross	0.10 ± 0.03	0.58	-1.1 ± 2.3	0.49
$\mu\mu$ + jets $\rightarrow$ γ + jets	Star	-0.06 ± 0.04	0.31	4.2 ± 4.3	0.29

Table 4.12.: A summary of the results obtained from zeroeth order polynomial (i.e. a constant) and linear fits to five sets of closure tests performed in the $2 \geq n_{\mathrm{jet}} \geq 3$ category. The two columns show the best fit value for the slope obtained when performing a constant (left) and linear (right) fit and the p-value for that fit.

		Constant fit		Linear fit	
Closure test	Symbol	Best fit value	p-value	Slope (10^{-4})	p-value
$\alpha_T < 0.55 \rightarrow \alpha_T > 0.55$ (μ + jets)	Circle	-0.05 ± 0.03	0.21	3.0 ± 2.9	0.21
0 b-jets $\rightarrow$ 1 b-jet (μ + jets)	Square	-0.03 ± 0.03	0.55	-1.0 ± 1.9	0.47
1 b-jets $\rightarrow$ 2 b-jet (μ + jets)	Triangle	-0.02 ± 0.03	0.39	1.1 ± 2.2	0.31
μ + jets $\rightarrow$ $\mu\mu$ + jets	Cross	0.08 ± 0.07	0.08	4.8 ± 4.3	0.07
$\mu\mu$ + jets $\rightarrow$ γ + jets	Star	-0.03 ± 0.10	0.72	-4.0 ± 7.0	0.64

Table 4.13.: A summary of the results obtained from zeroeth order polynomial (i.e. a constant) and linear fits to five sets of closure tests performed in the $n_{\mathrm{jet}} \geq 4$ category. The two columns show the best fit value for the slope obtained when performing a constant (left) and linear (right) fit and the p-value for that fit.

Table 4.14 shows the same fits applied to the three closure tests that probe the modelling between the different n_{jet} bins. The best fit value and its uncertainty is listed for each set of closure tests in all three tables, along with the p-value of the constant and linear fits applied.

The best fit value for the constant parameter is indicative of the level of closure, averaged across the full range of H_T bins in the analysis, and the p-value an indicator of any

		Constant fit		Linear fit	
Closure test	Symbol	Best fit value	p-value	Slope (10^{-4})	p-value
μ + jets	Inverted triangle	-0.03 ± 0.02	0.02	0.0 ± 1.0	0.01
μ + jets (outlier removed)	Inverted triangle	-0.04 ± 0.01	0.42	-1.4 ± 1.1	0.49
γ + jets	Diamond	0.12 ± 0.05	0.79	6.0 ± 4.7	0.94
$\mu\mu$ + jets	Asterisk	-0.04 ± 0.07	0.20	4.9 ± 4.4	0.20

Table 4.14.: A summary of the results obtained from zeroeth order polynomial (i.e. a constant) and linear fits to three sets of closure tests performed between the $2 \leq n_{\mathrm{jet}} \leq 3$ and $n_{\mathrm{jet}} \geq 4$ categories. The two columns show the best fit value for the slope obtained when performing a constant (left) and linear (right) fit and the p-value for that fit.

significant dependence on H_T within the closure tests. The best fit values of all the tests are either statistically compatible with zero bias (i.e, less than 2σ from zero) or at the level of 10% or less, with the exception of one closure test discussed below.

Within Table 4.14, there exists one test that does not satisfy the above statement, which is the $2 \leq n_{jet} \leq 3 \rightarrow n_{jet} \geq 4$ test using the μ + jets control sample. The low p-value can be largely attributed to an outlier in the $675 < H_T < 775$ GeV bin, rather than any significant trend in H_T. Removing this single outlier from the constant fit performed, gives a best fit value of -0.04 ± 0.01, $\chi^2/$ d.o.f $= 6.07/6$. and a p-value of 0.42. These modified fit results are included within Table 4.14 .

In addition the best fit values for the slope terms of the linear fits in all three tables are of the order 10^{-4}, which corresponds to a percent level change per 100 GeV. However in all cases, the best fit values are fully compatible with zero (within 1σ) once again with the exception detailed above, indicating that the level of closure is H_T independent.

4.6.1. Determining systematic uncertainties from closure tests

Once it has been established that no significant bias or trend has been exist within the closure tests, systematic uncertainties are determined. The statistical precision of the closure tests is considered a suitable benchmark for determining the systematic uncertainties that are assigned to the TF's, which are propagated through to the likelihood fit.

The systematic uncertainty band is split into five separate regions of H_T. Within each region the square root of the sample variance, σ^2, is taken over the eight closure tests to determine the systematic uncertainties to be applied within that region.

Using this procedure the systematic uncertainties for each region are calculated and are shown in Table 4.15, with the systematic uncertainty to be used in the likelihood model conservatively rounded up to the nearest decile and applied across all $n_{\mathrm{b}}^{\mathrm{reco}}$ categories.

H_T band (GeV)	$2 \leq n_{jet} \leq 3$	$n_{jet} \geq 4$
$275 < H_T < 325$	10%	10%
$325 < H_T < 375$	10%	10%
$375 < H_T < 575$	10%	10%
$575 < H_T < 775$	20%	20%
$H_T > 775$	20%	30%

Table 4.15.: Calculated systematic uncertainties for the five H_T regions, determined from the closure tests. Uncertainties shown for both jet multiplicity categories. Values used within the likelihood model are conservatively rounded up to the nearest decile.

Figure 4.11 shows the sets of closure tests overlaid on top of grey bands that represent the H_T dependent systematic uncertainties. These systematic uncertainties are assumed to fully uncorrelated between the different n_b multiplicity categories and across the five H_T regions. This can be considered a more conservative approach given that some correlations between adjacent H_T bins could be expected due to comparable kinematics.

These closure tests represent a conservative estimate of the systematic uncertainty in making a background prediction for the signal region, which is due to significant differences in the background composition and event kinematics between the two sub-samples used in the closure tests. This is contrary to the signal region prediction where the two sub-samples are both have a comparable background admixture and similar kinematics owing to the fact that the predictions are always made using the same (n_{jet}, $n_{\mathrm{b}}^{\mathrm{reco}}$, H_T) bin.

This point is emphasised when we examine the sensitivity of the TF's to a change in the admixture of W + jets and $t\bar{t}$ with the control and signal samples. This is accomplished by varying the cross sections of the W +jets and $t\bar{t}$ by +20% and -20%, respectively. Figures C.2 and C.3 within Appendix C, show the effect upon the closure tests for both jet multiplicity categories. Given these variations in cross sections, the level of closure is found to be significantly worse, with biases as large as $\sim$ 30%, most apparent in the lowest H_T bins. However the TF's used to extrapolate from control to signal are seen to change only at the percent level by this large change in cross section, shown in Table C.1.

Given the robust behaviour of the translation factors with respect to large (and opposite) variations in the W + jets and $t\bar{t}$ cross sections, one can assume with confidence that

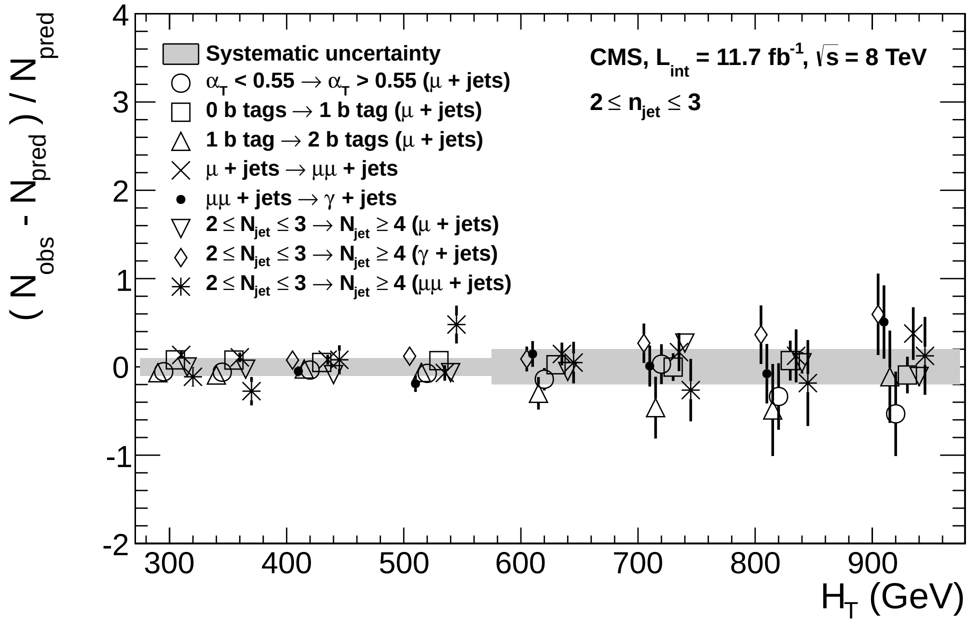

(a)

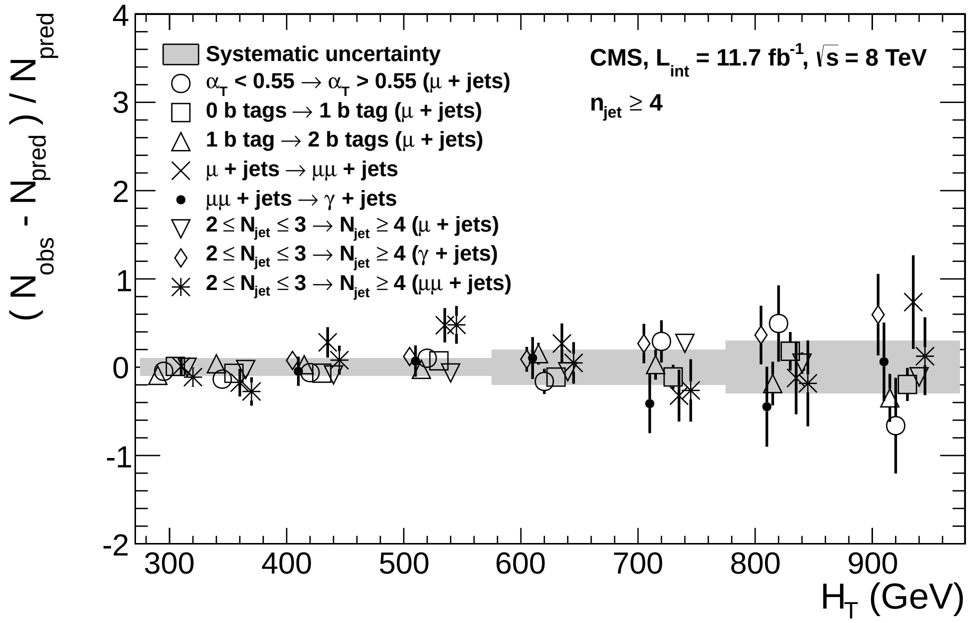

(b)

Figure 4.11.: Sets of closure tests (open symbols) overlaid on top of the systematic uncertainty used for each of the five H_T regions (shaded bands) and for the two different jet multiplicity categories: (a) $2 \leq n_{\text{jet}} \leq 3$ and (b) $n_{\text{jet}} \geq 4$.

any bias in the translation factors is adequately (and conservatively) covered by the systematic uncertainties used in the analysis.

4.7. Simplified Models, Efficiencies and Systematic Uncertainties

The results of the analysis are interpreted using various SMS signal models, which as already introduced in Section (2.4.1) offer a natural starting point for quantifying and characterising SUSY signals, and a means to identify the boundaries of search sensitivity for different mass splittings, kinematic ranges, and final states.

Each model is parameterised in a two dimensional parameter space, ($m_{\widetilde{q}/\widetilde{g}}$, m_{LSP}), from which upper limits on the production cross sections of the various SMS models can be set.

Each signal sample is generated at Leading Order (LO) with Pythia [82], and cross sections calculated for Next to Leading Order (NLO) and Next to Leading Logorithmic Order (NLL) [83], with events simulated using the `Fastsim` framework. This framework represents a simplified simulation of the CMS detector, but allows for faster production of various signal topologies with different mass parameters. A series of correction factors are applied to account for differences between `Fastsim` [84] and `Fullsim` [85] simulation, which can affect the resultant $n_{\mathrm{b}}^{\mathrm{reco}}$ distribution and which are detailed in Section (4.7.2).

4.7.1. Signal efficiency

The analysis selection efficiency, ϵ, is measured for each mass point of the interpreted model, this serves as a measure of the sensitivity of the signal selection for that particular sparticle and LSP mass. The signal yield is then given by

$$Y(m_{\widetilde{q}/\widetilde{g}}, m_{LSP}) = \epsilon \times \sigma \times \mathcal{L}, \tag{4.13}$$

where σ represents the model's cross section and $\mathcal{L}$ the luminosity. An upper limit on σ taken from theory can then allow for the setting of limits in terms of the particle mass.

Figure 4.12 shows the expected signal efficiency of the signal selection for the `T1` and `T2` SMS models interpreted in this analysis. The efficiency maps are produced with the requirement $H_T > 275$ GeV (i.e., no binning in H_T) and requirements on n_{jet} and n_b^{reco} that are appropriate for the model in question.

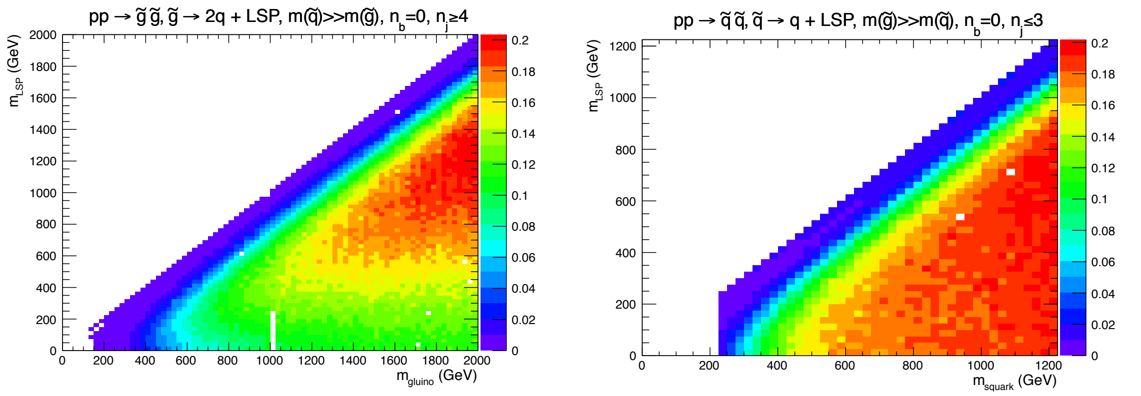

(a) Model T1, $n_{jet} \geq 4$, $n_b^{reco} = 0$

(b) Model T2, $n_{jet} \leq 3$, $n_b^{reco} = 0$

Figure 4.12.: Signal efficiencies for the SMS models (a) T1 ($\widetilde{g}\widetilde{g}^* \to q\bar{q}\widetilde{\chi}_1^0 q\bar{q}\widetilde{\chi}_1^0$) and (b) T2 ($\widetilde{q}\widetilde{q}^* \to q\widetilde{\chi}_1^0 \bar{q}\widetilde{\chi}_1^0$) when requiring $n_{jet} \geq 4$ and ≤ 3 respectively, and $n_b^{reco} = 0$.

The same procedure is conducted in the analysis control samples. It is found in the μ + jets control samples, that the S/B ratios for the expected signal yields in each of the SMS models are many time smaller than in the hadronic signal region. The relative contamination for the $\mu\mu$ + jets sample is smaller still due to the requirement of a second muon. The relative contamination for the γ + jets sample is expected to be zero for the models under consideration. These small, relative levels of contamination are accounted for in the fitting procedure, as described in Section (4.8.4).

4.7.2. Applying b-tag scale factor corrections in signal samples

High-statistic `FastSim` signal simulation samples are unavailable for each signal signal point, which means that a different procedure to the formula method described in Section (4.5) is employed. Furthermore, the use of the `FastSim` framework in the reconstruction introduces an extra set of scale-factor corrections, to be applied simultaneously with those correcting the full-simulation to the data.

For these signal models, an event-by-event re-weighting procedure is applied. This applied weight depends on both the flavour content and the b-tagging status of the reconstruction level jets in the event.

The re-weighting procedure can be described by first considering a single jet in an signal sample event. The flavour of the jet is determined using the method described in Section (4.5.1).

Maps of tagging efficiencies determined from `FullSim` simulation samples for each of the b, c and light jet flavours are produced, binned as a function of jet p_T and η after the application of the hadronic signal selection. The binning of the maps are chosen to reflect the set of p_T and η dependant corrections of simulation to data defined by [86]. Taking the flavour, p_T and η values of each jet in the event, the expected tagging efficiency, $\epsilon_{MC}(p_T, \eta, f)$ is extracted from these maps.

The actual tagging efficiency of the `FastSim` jet, $\epsilon_{\texttt{FastSim}}(p_T, \eta, f)$, differs from that measured in `FullSim`, $\epsilon_{MC}(p_T, \eta, f)$ and is related via an additional correction factor,

$$\epsilon_{\texttt{FastSim}}(p_T, \eta, f) = \frac{\epsilon_{MC}(p_T, \eta, f)}{SF_{\texttt{Fast}\rightarrow\texttt{Full}}(p_T, \eta, f)}, \tag{4.14}$$

where $SF_{\texttt{Fast}\rightarrow\texttt{Full}}(p_T, \eta, f)$ represents a set of p_T and η dependant corrections, that are specific for each SMS model. These are calculated from the ratio of b-tagging rates between a `FullSim` $t\bar{t}$ sample, and a selection of mass points for that particular `FastSim` SMS model, again measured individually for b, c and light-flavoured jets.

Similarly the tagging efficiencies measured in data [?], $\epsilon_{Data}(p_T, \eta, f)$, are further related to $\epsilon_{\texttt{FastSim}}(p_T, \eta, f)$ by the equation,

$$\begin{aligned} \epsilon_{Data}(p_T, \eta, f) &= \epsilon_{MC}(p_T, \eta, f) \times SF_{MC\rightarrow Data}(p_T, \eta, f) \\ &= \epsilon_{\texttt{FastSim}}(p_T, \eta, f) \times \underbrace{SF_{\texttt{Fast}\rightarrow\texttt{Full}}(p_T, \eta, f) \times SF_{MC\rightarrow Data}(p_T, \eta, f)}_{\mathrm{SF}_{\texttt{Fast}} \rightarrow Data}. \end{aligned} \tag{4.15}$$

For each jet, the weight of the event is re-weighted according to wether the jet fires the b-tagger. In the instance that the jet *is* b-tagged, the event weight will be modified by,

$$\text{weight} = SF_{\texttt{Fast}\rightarrow Data} \times \text{weight}, \tag{4.16}$$

and in the case that the jet does *not* fire the b-tagger,

$$\text{weight} = \frac{1 - \epsilon_{Data}(p_T, \eta, f)}{1 - \epsilon_{\texttt{FastSim}}(p_T, \eta, f)} \times \text{weight}. \tag{4.17}$$

All events that pass the selection criteria are reweighted in this way, and represent the yields in each n_b^{reco} bin corrected from `Fastsim` to data.

4.7.3. Experimental uncertainties

The systematic uncertainty on the expected signal acceptance times analysis efficiency is determined independently for the each SMS model considered. These systematics stem stem from uncertainties on the parton distribution functions, the luminosity measurement, jet energy scale, b-tag scale factor measurements and the efficiencies of various cuts used in the signal selection, including the $\not{H}_T / \not{E}_T$, dead ECAL cleaning filter and lepton / photon event vetoes.

Rather than trying to estimate the level of systematic that is applicable point-by-point in a model space, general behaviours are considered and instead constant systematics are estimated in two regions of the SMS models parameter space.

These two regions are defined as, near (small mass splittings) and far (large mass splittings) from the mass degenerate diagonal, where the far region is bounded by the condition

$$m_{\tilde{q}/\tilde{g}} - m_{LSP} > 350GeV \qquad\qquad m_{\tilde{q}/\tilde{g}} > 475GeV.$$

The total systematics in each region are evaluated in the following ways:

Jet energy scale : The relative change in the signal efficiency is gauged by varying the energy of all jets in an event up or down according to a p_T and η dependent jet energy scale uncertainty. Within the two systematic regions, the resulting systematic uncertainties for each SMS model are determined by taking the value of the 68^{th} percentile for the distributions of the relative change in the signal efficiency.

Luminosity measurement : The measurement of luminosity taken propagates through to an uncertainty on the signal event yield when considering any new physics model, which is currently 4.4% [87].

Parton density function : Each signal sample is produced using the CTEQ6L1 parton density function. The effect on the signal acceptance when re-weighting to the central value of three different parton distribution functions, CT10, MSTW08 and NNPDF2.1 are examined [88]. It is found that the change of the signal efficiency in different SMS models, due to the alternate PDF sets are typically a few percent, and approaches 10% at higher squark/gluon and LSP masses.

$\not{H}_T/\not{E}_T$ cleaning cut : The ratio of the efficiencies of the cleaning cut are compared in simulation and data after application of the μ + jets control sample selection. No α_T cut or further event cleaning filters are applied. The ratio of the efficiencies observed in data and simulation for a cut value of $\not{H}_T/\not{E}_T < 1.25$ and the two jet multiplicity bins, $2 \leq n_{\text{jet}} \leq 3$ and $n_{\text{jet}} \geq 4$ are 1.028 $\pm$ 0.007 and 1.038 $\pm$ 0.015 respectively. These deviations are taken to represent the systematic uncertainty on the simulation modelling of this variable.

Deal ECAL cleaning filter : The ratio of the efficiencies observed in data and simulation for this filter in the two jet multiplicity bins, $2 \leq n_{\text{jet}} \leq 3$ and $n_{\text{jet}} \geq 4$, are 0.961 $\pm$ 0.008 and 0.961 $\pm$ 0.009, respectively. These deviations from unity are taken to represent the systematic uncertainties in the modelling in simulation of this filter.

Lepton and photon vetoes : The uncertainty on the efficiency of the lepton and photon vetoes is determined by considering truth information. The efficiency of the vetoes is measured after applying relevant object filters with identical logic, but based on truth instead of reconstructed objects. Where the efficiency is found to not be 100%, it is taken to represent the fraction of signal events that are incorrectly vetoed. This deviation is taken directly as the systematic uncertainty on the efficiency. The systematic uncertainty is only non-zero for models which contain third-generation quarks in the final state, where the uncertainties are at the order of 1% level.

B-tag scale factor uncertainties : The relative change in the signal efficiency is observed when relevant flavour, p_T and η dependant b-tag correction factors, are varied up or down by their uncertainty. Within the two systematic regions, the resulting systematic uncertainties for each SMS model are determined by taking the value of the 68$^{\text{th}}$ percentile for the distributions of the relative change in the signal efficiency, over all mass points.

Tables 4.16 and 4.17 summarise all the aforementioned systematic uncertainties on the signal efficiencies for each individual SMS model interpreted in the analysis. In the case of the `T1tttt` model, in which pair produced gluinos decay to $t\bar{t}$ pairs and the LSP, the near region of SMS space is not considered, and so no systematic uncertainties are included.

In both of the defined regions it is found that the systematic uncertainties are relatively flat justifying the approach taken. The systematic uncertainties used for the region near to the diagonal fall in the range 13-15%; similarly, for the region far from the diagonal, the uncertainties used fall in the range 12-23%. These uncertainties are all propagated through to the limit calculation.

Model	Luminosity	p.d.f	JES	$\not{H}_T/\not{E}_T$	Dead ECAL	Lepton Vetoes	b-tagging	Total
`T1`	4.4	10.0	5.6	3.8	4.1	n/a	3.1	13.9
`T2`	4.4	10.0	4.1	2.8	4.1	n/a	2.4	12.9
`T2tt`	4.4	10.0	6.5	3.8	4.1	0.8	0.8	13.9
`T2bb`	4.4	10.0	4.8	2.8	4.1	0.3	2.2	13.1
`T1tttt`	n/a	n/a	n/a	n/a	n/a	n/a	n/a	n/a
`T1bbbb`	4.4	10.0	7.3	3.8	4.1	0.5	2.7	14.5

Table 4.16.: Estimates of systematic uncertainties on the signal efficiency (%) for various SMS models when considering points in the region near to the diagonal (i.e. small mass splitting and compressed spectra). The uncertainties are added in quadrature to obtain the total.

Model	Luminosity	p.d.f	JES	$\not{H}_T/\not{E}_T$	Dead ECAL	Lepton Vetoes	b-tagging	Total
`T1`	4.4	10.0	0.8	3.8	4.1	n/a	6.6	14.0
`T2`	4.4	10.0	1.1	2.8	4.1	n/a	5.8	13.4
`T2tt`	4.4	10.0	3.5	3.8	4.1	0.6	1.6	12.9
`T2bb`	4.4	10.0	0.9	2.8	4.1	0.3	2.7	12.3
`T1tttt`	4.4	10.0	0.5	3.8	4.1	1.4	19.4	23.0
`T1bbbb`	4.4	10.0	1.5	3.8	4.1	0.4	10.1	16.0

Table 4.17.: Estimates of systematic uncertainties on the signal efficiency (%) for various SMS models when considering points in the region far from the diagonal (i.e. large mass splitting). The uncertainties are added in quadrature to obtain the total.

4.8. Statistical Interpretation

For a given category of events satisfying requirements on both n_{jet} and n_b^{reco}, a likelihood model of the observations in multiple data samples is used to gauge agreement between the observed yields in the hadronic signal region, and the predicted yields obtained from the control samples. In addition to checking wether the predictions are compatible with a SM only hypothesis, the likelihood model is also used to test for the presence of a variety of signal models. The statistical framework outlined within this section is presented in greater detail within [89].

4.8.1. Hadronic sample

Let N be the number of bins on H_T, with n^i the number of events observed satisfying all selection requirements in each H_T bin i. The likelihood of the observations can then be written :

$$L_{had} = \prod_i \text{Pois}(n^i | b^i + s^i), \tag{4.18}$$

where b^i represents the expected SM background

$$b^i = EWK_i + QCD_i, \tag{4.19}$$

and s^i the expected number of signal events from the different SMS models interpreted. Pois refers to the Poisson distribution of these values and is defined as :

$$\text{Pois}(\chi|\lambda) = \frac{\lambda^\chi \exp^{-\lambda}}{k!}. \tag{4.20}$$

4.8.2. H_T evolution model

The hypothesis, that for a process the α_T ratio falls exponentially (see Section (4.2.4)) in H_T is defined by Equation (4.10), where k_{QCD} is constrained by measurements in a signal sideband region.

The expected QCD background, QCD^i, within a bin i is then modelled as,

$$QCD^i = m^i A_{QCD} e^{-k_{QCD}\langle H_T \rangle}, \tag{4.21}$$

where m_i represent the number of events observed with $\alpha_T \leq 0.55$ in each H_T bin i, and $\langle H_T \rangle$ represents the mean H_T of each bin. Expressed as functions of just the zeroth bin, QCD^0, and k_{QCD}, the QCD expectation is given by

$$QCD^i = QCD^0 (\frac{m^i}{m^0}) e^{-k_{QCD}(\langle H_T \rangle^i - \langle H_T \rangle^0}. \tag{4.22}$$

4.8.3. EWK control samples

The EWK background estimation within each bin, i, is broken into two components, the expected yield from Z $\rightarrow \nu\bar{\nu}$ and $t\bar{t}$-W (plus other residual backgrounds) events. This is written as, Z^i_{inv} and $t\bar{t}W^i$, and it follows that

$$EWK^i = Z^i_{inv} + t\bar{t}W^i. \tag{4.23}$$

This can be further expressed as

$$Z^i_{inv} \equiv f^i_{Zinv} \times EWK^i, \tag{4.24}$$
$$t\bar{t}W^i \equiv (1 - f^i_{Zinv}) \times EWK^i, \tag{4.25}$$

where f^i_{Zinv} represents the expected yield from Z $\rightarrow \nu\bar{\nu}$ in bin i divided by the expected EWK background EWK^i. This fraction is modelled as a linear component

$$f^i_{Zinv} = f^0_{Zinv} + \frac{\langle H_T \rangle^i - \langle H_T \rangle^0}{\langle H_T \rangle^{N-1} - \langle H_T \rangle^0}(f^{N-1}_{Zinv} - f^i_{Zinv}), \tag{4.26}$$

where N again represents the number of H_T bins, and f^i_{Zinv} and f^{N-1}_{Zinv} are float parameters whose final values are limited between zero and one.

Within each H_T bin there are three background measurements for the different control samples, n^i_γ, n^i_μ and $n^i_{\mu\mu}$, representing the event yields from the γ + jets, μ + jets and $\mu\mu$ + jets control samples respectively. Each of these have a corresponding yield in simulation, MC^i_γ, MC^i_μ and $MC^i_{\mu\mu}$. Within the hadronic signal region there are also corresponding simulated yields for Z $\rightarrow \nu\bar{\nu}$ (MC^i_{Zinv}) and $t\bar{t}$ + W ($MC^i_{t\bar{t}+W}$), which are used to define

$$r^i_\gamma = \frac{MC^i_\gamma}{MC^i_{Zinv}}; \qquad r^i_{\mu\mu} = \frac{MC^i_{\mu\mu}}{MC^i_{Zinv}}; \qquad r^i_\mu = \frac{MC^i_\mu}{MC^i_{t\bar{t}+W}} \qquad , \tag{4.27}$$

where r^i_p represents the inverse of the TF's used to extrapolate the yield of each background process.

The likelihoods regarding the three measured yields n^i_γ, $n^i_{\mu\mu}$, n^i_μ can then be fully expressed as

$$L_\gamma = \prod_i \text{Pois}(n^i_\gamma | \rho^j_{\gamma Z}.r^i_\gamma.Z^i_{inv}), \tag{4.28}$$

$$L_{\mu\mu} = \prod_i \text{Pois}(n^i_{\mu\mu} | \rho^j_{\mu\mu Z}.r^i_{\mu\mu}.Z^i_{inv}), \tag{4.29}$$

$$L_\mu = \prod_i \text{Pois}(n^i_\mu | \rho^j_{\mu Y}.r^i_\mu.Y^i + s^i_\mu), \tag{4.30}$$

$$\tag{4.31}$$

which contain an additional term s^i_μ, which represents the signal contamination in the μ + jets sample. The parameters $\rho^j_{\gamma Z}$, $\rho^j_{\mu\mu}$ and ρ^j_μ represent "correction factors" that accommodate the data driven systematic uncertainties derived from the control samples in Section (4.12).

Each of these equations are used to estimate the maximum likelihood value for relevant background in the signal region given the observations n_p^i in each of the control samples (see Section (4.2.3)).

The measurements in each of the control samples and the hadronic signal region, along with the ratios r_γ^i, $r_{\mu\mu}^i$, and r_μ^i, are all considered simultaneously through the relationships defined by Equations (4.19),(4.24) and (4.25).

In addition to the Poisson product, an additional log-normal term is introduced to accommodate the systematic uncertainties given by,

$$L_{EWK\ syst} = \prod_j \mathrm{Logn}(1.0|\rho^j_{\mu W}, \sigma^j_{\mu W}) \times \mathrm{Logn}(1.0|\rho^j_{\mu\mu Z}, \sigma^j_{\mu\mu Z}) \times \mathrm{Logn}(1.0|\rho^j_{\gamma Z}, \sigma^j_{\gamma Z}), \tag{4.32}$$

where $\sigma^j_{\gamma Z}$, $\sigma^j_{\mu\mu Z}$ and $\sigma^j_{\mu W}$ represent the relative systematic uncertainties for the control sample constraints and Logn is the log-normal distribution [90],

$$\mathrm{Logn}(x \mid \mu, \sigma_{rel}) = \frac{1}{x\sqrt{2\pi}\mathrm{ln\ k}} \exp\left(\frac{\mathrm{ln}^2(\frac{x}{\mu})}{2\mathrm{ln}^2\mathrm{k}}\right); \quad k = 1 + \sigma_{rel}. \tag{4.33}$$

Five parameters per control sample are used to span the eight H_T bins, with just one used for the three H_T bins in the $n_b^{reco} \geq 4$ category. These parameters span the same H_T ranges described in Section (4.6) and is shown in Table 4.18.

H_T bin (i)	0	1	2	3	4	5	6	7
syst. parameter (j)	0	1	2	2	3	3	4	4

H_T bin (i)	0	1	2
syst. parameter (j)	0	0	0

Table 4.18.: The systematic parameters used in H_T bins. Left: categories with eight bins; right: category with three bins.

Alternatively, in the higher n_b^{reco} categories ($n_b^{reco} \geq 2$), only the single muon sample is used to constrain the total EWK background. Therefore the likelihood function is greatly simplified and is represented by

$$L_{\mu}^{'} = \prod_{i} \text{Pois}(n_{\mu}^{i} | \rho_{\mu Y}^{j} . r_{\mu}^{'i} . EWK^{i} + s_{\mu}^{i}), \tag{4.34}$$

where,

$$r_{\mu}^{'i} = \frac{MC_{\mu}^{i}}{MC_{tot}^{i}}. \tag{4.35}$$

4.8.4. Contributions from signal

The cross section for each model is represented by x and l represents the total recorded luminosity considered by the analysis in the signal region. Let ϵ_{had}^{i} and ϵ_{μ}^{i} represent the analysis selection efficiency for that particular signal model in H_T bin i of the hadronic and μ + jets control sample respectively. Letting δ represent the relative uncertainty on the signal yield, assumed to be fully correlated across all bins, and ρ_{sig} the "correction factor" to the signal yield which accommodates this uncertainty. f represents an unknown multiplicative factor on the signal cross section, for which an allowed interval is computed.

The expected signal yield s^i is thus given by

$$s^{i} \equiv f \rho_{sig} x l \epsilon_{had}^{i} \tag{4.36}$$

and signal contamination with the μ + jets control sample by

$$s_{\mu}^{i} \equiv f \rho_{sig} x l \epsilon_{\mu}^{i} \tag{4.37}$$

The systematic uncertainty on the signal is additionally included by the term

$$L_{\text{sig}} = \text{Logn}(1.0 | \rho_{sig}, \delta). \tag{4.38}$$

A discussion of the SMS signal models through which the analysis is interpreted can be found in the following Chapter.

4.8.5. Total likelihood

The total likelihood function for a given signal bin k(n_b^{reco}, n_{jet}) is then given by the product of the likelihood functions introduced within the previous sections:

$$\begin{aligned} L_{\text{Tot}}^k &= L_{had}^k \times L_{\mu}^k \times L_{\gamma}^k \times L_{\mu\mu}^k \times L_{EWKsyst}^k \times L_{QCD}^k; && (0 \leq n_{\text{b}}^{\text{reco}} \leq 1) \\ L_{\text{Tot}}^k &= L_{had}^k \times L_{\mu}^{\prime k} \times L_{\mu\ syst}^k \times L_{QCD}^k && (n_{\text{b}}^{\text{reco}} \geq 2). \end{aligned} \quad (4.39)$$

In categories containing eight H_T bins and utilising the three control samples (μ + jets, $\mu\mu$ + jets, γ + jets), there are 25 nuisance parameters, whilst when just one control sample is used to estimate the EWK background, there are 15 nuisance parameters. Where three H_T bins are used (the highest n_b^{reco} category), there are 6 nuisance parameters. This information is summarised within Table 4.19.

Nuisance parameter	Total
$(EWK^i)_{\ i\ :0-7(2)}$	8 (3)
f_{Zinv}^0	1*
f_{Zinv}^7	1*
QCD^0	1
k_{QCD}	1
$(\rho_{\gamma Z}^j)_{\ j\ :2-4}$	3 *
$(\rho_{\mu\mu Z}^j)_{\ j\ :0-4}$	5 *
$(\rho_{\mu W}^j)_{\ j\ :0-4(0)}$	5 (1)

Table 4.19.: Nuisance parameters used within the different hadronic signal bins of the analysis. Parameters denoted by a * are not considered in the case of a single control sample being used to predict the EWK background. Numbers within brackets highlight the number of nuisance parameters in the case of three H_T bins being used.

When considering SUSY signal models within the likelihood, the additional L_{sig} term is included and therefore when multiple categories are fit simultaneously the total likelihood is then represented by

$$L_{\mathrm{Tot}}^{\mathrm{signal}} = L_{sig} \times \prod_{k} L_{\mathrm{Tot}}^{k}. \tag{4.40}$$

Chapter 5.

Results And Interpretation

Using the statistical framework outlined in the previous chapter, results are compared to a SM-only hypothesis (Section (5.1)) and interpreted within various SMS models (Section (5.2)).

5.1. Compatibility with the Standard Model Hypothesis

The SM background only hypothesis is tested by removing any signal contributions within the signal and control samples, and the likelihood function is maximised over all parameters using Rootfit [91] and MINUIT [92]. The results of the search consist of the observed yields in the hadronic signal sample, and the μ + jets, $\mu\mu$ + jets and γ + jets control samples.

These observed yields along with the expectations and uncertainties given by the simultaneous fit for the hadronic signal region are given in Table 5.2. The results obtained from the simultaneous fits, including that of the three control samples, are shown in Figure 5.1-5.8, as summarised in Table 5.1.

The figures show a comparison between the observed yields and the SM expectations across all H_T bins, and in all n_{jet} and n_b^{reco} multiplicity categories. In all categories the samples are well described by the SM only hypothesis. In particular no significant excess is observed above SM expectation within the hadronic signal region.

n_{jet}	n_b^{reco}	Control samples fitted	Figure
2-3	0	μ + jets,$\mu\mu$ + jets,γ + jets	5.1
2-3	1	μ + jets,$\mu\mu$ + jets,γ + jets	5.2
2-3	1	μ + jets	5.3
$\geq$4	0	μ + jets,$\mu\mu$ + jets,γ + jets	5.4
$\geq$4	1	μ + jets,$\mu\mu$ + jets,γ + jets	5.5
$\geq$4	2	μ + jets	5.6
$\geq$4	3	μ + jets	5.7
$\geq$4	4	μ + jets	5.8

Table 5.1.: Summary of control samples used by each fit results, and the Figures in which they are displayed.

			H_T bin (GeV)							
Cat	n_b^{reco}	n_{jet}	275-325	325-375	375-475	474-575	575-675	675-775	775-875	875-∞
SM	0	≤ 3	6235^{+100}_{-67}	2900^{+60}_{-54}	1955^{+34}_{-39}	558^{+14}_{-15}	186^{+11}_{-10}	$51.3^{+3.4}_{-3.8}$	$21.2^{+2.3}_{-2.2}$	$16.1^{+1.7}_{-1.7}$
Data			6232	2904	1965	552	177	58	16	25
SM	0	≥ 4	1010^{+34}_{-24}	447^{+19}_{-16}	390^{+19}_{-15}	250^{+12}_{-11}	111^{+9}_{-7}	$53.3^{+4.3}_{-4.3}$	$18.5^{+2.4}_{-2.4}$	$19.4^{+2.5}_{-2.7}$
Data			1009	452	375	274	113	56	16	27
SM	1	≤ 3	1162^{+37}_{-29}	481^{+18}_{-19}	341^{+15}_{-16}	$86.7^{+4.2}_{-5.6}$	$24.8^{+2.8}_{-2.7}$	$7.2^{+1.1}_{-1.0}$	$3.3^{+0.7}_{-0.7}$	$2.1^{+0.5}_{-0.5}$
Data			1164	473	329	95	23	8	4	1
SM	1	≥ 4	521^{+25}_{-17}	232^{+15}_{-12}	188^{+12}_{-11}	106^{+6}_{-6}	$42.1^{+4.1}_{-4.4}$	$17.9^{+2.2}_{-2.0}$	$9.8^{+1.5}_{-1.4}$	$6.8^{+1.2}_{-1.1}$
Data			515	236	204	92	51	13	13	6
SM	2	≤ 3	224^{+15}_{-14}	$98.2^{+8.4}_{-6.4}$	$59.0^{+5.2}_{-6.0}$	$12.8^{+1.6}_{-1.6}$	$3.0^{+0.9}_{-0.7}$	$0.5^{+0.2}_{-0.2}$	$0.1^{+0.1}_{-0.1}$	$0.1^{+0.1}_{-0.1}$
Data			222	107	58	12	5	1	0	0
SM	2	≥ 4	208^{+17}_{-9}	103^{+9}_{-7}	$85.9^{+7.2}_{-6.9}$	$51.7^{+4.6}_{-4.7}$	$19.9^{+3.4}_{-3.0}$	$6.8^{+1.2}_{-1.3}$	$1.7^{+0.7}_{-0.4}$	$1.3^{+0.4}_{-0.3}$
Data			204	107	84	59	24	5	1	2
SM	3	≥ 4	$25.3^{+5.0}_{-4.2}$	$11.7^{+1.7}_{-1.8}$	$6.7^{+1.4}_{-1.2}$	$3.9^{+0.8}_{-0.8}$	$2.3^{+0.6}_{-0.6}$	$1.2^{+0.3}_{-0.4}$	$0.3^{+0.2}_{-0.1}$	$0.1^{+0.1}_{-0.1}$
Data			25	13	4	2	2	3	0	0
SM	4	≥ 4	$0.9^{+0.4}_{-0.7}$	$0.3^{+0.2}_{-0.2}$	$0.6^{+0.3}_{-0.3}$					
Data			1	0	2					

Table 5.2.: Comparison of the measured yields in the each H_T, n_{jet} and n_b^{reco} jet multiplicity bins for the hadronic sample with the SM expectations and combined statistical and systematic uncertainties given by the simultaneous fit.

Given the lack of an excess in data hinting at a possible supersymmetric signature within the data, interpretations are made on the production masses and cross section of a range of SUSY decay topologies within the following section.

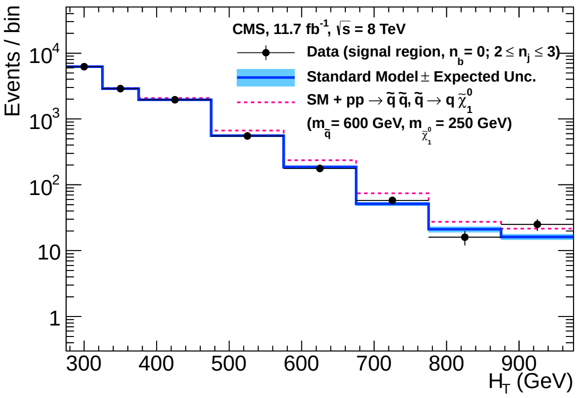

(a) Hadronic sample, $2 \leq n_{jet} \leq 3$ and $n_b^{reco} = 0$

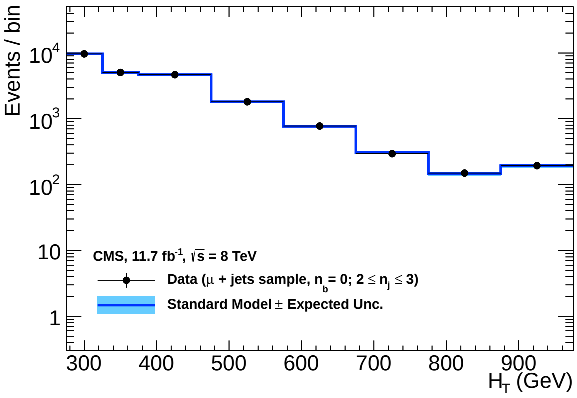

(b) μ + jets sample, $2 \leq n_{jet} \leq 3$ and $n_b^{reco} = 0$

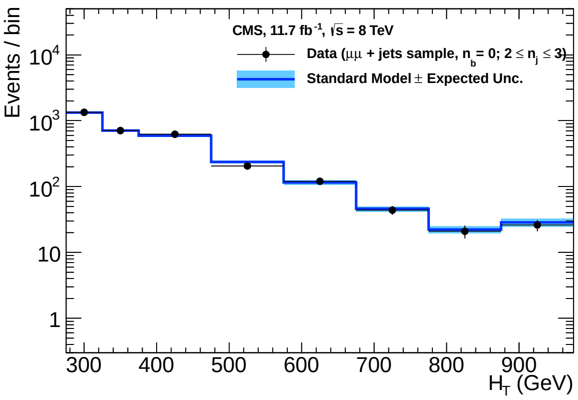

(c) $\mu\mu$ + jets sample, $2 \leq n_{jet} \leq 3$ and $n_b^{reco} = 0$

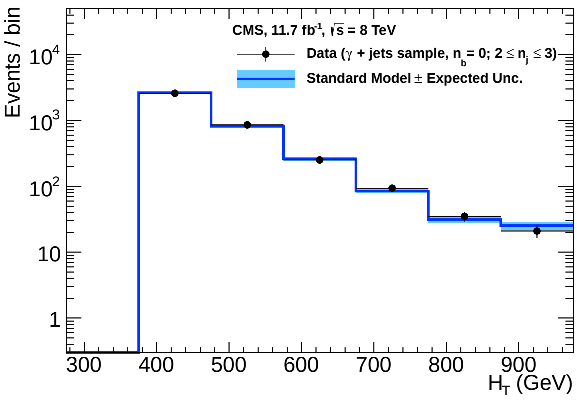

(d) γ + jets sample, $2 \leq n_{jet} \leq 3$ and $n_b^{reco} = 0$

Figure 5.1.: Comparison of the observed yields and SM expectations given by the simultaneous fit in bins of H_T for the (a) hadronic, (b) μ + jets, (c) $\mu\mu$ + jets and (d) γ + jets samples when requiring $n_b^{reco} = 0$ and $n_{jet} \leq 3$. The observed event yields in data (black dots) and the expectations and their uncertainties for all SM processes (blue line with light blue bands) are shown. An example signal expectation (red solid line) for the $D1$ SMS signal point from Table 4.1 is superimposed on the SM background expectation.

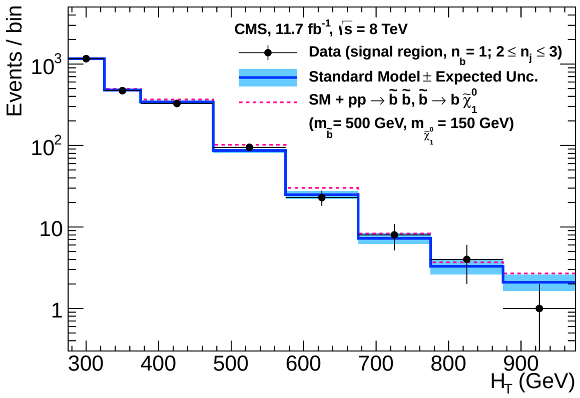

(a) Hadronic sample, $2 \leq n_{jet} \leq 3$ and $n_b^{reco} = 1$

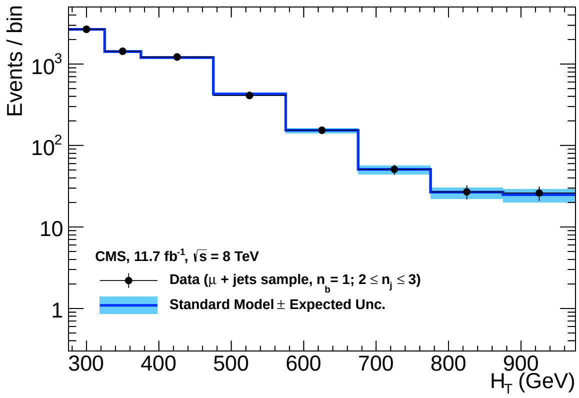

(b) μ + jets sample, $2 \leq n_{jet} \leq 3$ and $n_b^{reco} = 1$

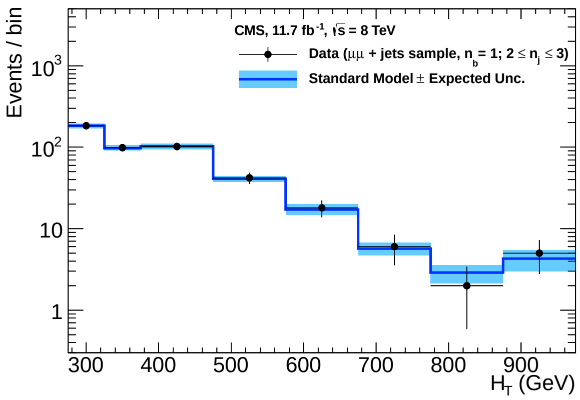

(c) $\mu\mu$ + jets sample, $2 \leq n_{jet} \leq 3$ and $n_b^{reco} = 1$

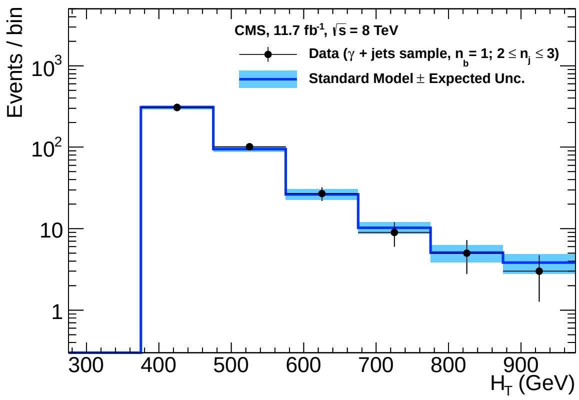

(d) γ + jets sample, $2 \leq n_{jet} \leq 3$ and $n_b^{reco} = 1$

Figure 5.2.: Comparison of the observed yields and SM expectations given by the simultaneous fit in bins of H_T for the (a) hadronic, (b) μ + jets, (c) $\mu\mu$ + jets and (d) γ + jets samples when requiring $n_b^{reco} = 1$ and $n_{jet} \leq 3$. The observed event yields in data (black dots) and the expectations and their uncertainties for all SM processes (blue line with light blue bands) are shown. An example signal expectation (red solid line) for the $D2$ SMS signal point from Table 4.1 is superimposed on the SM background expectation.

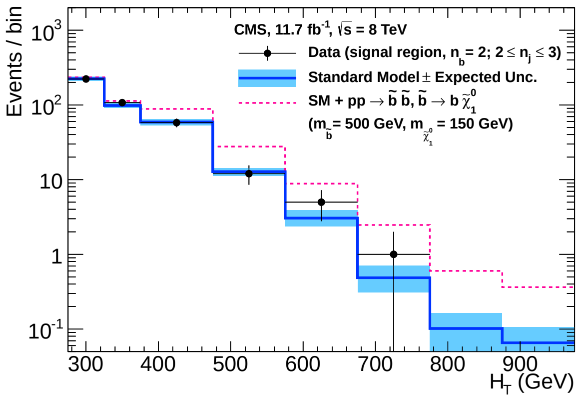

(a) Hadronic sample, $2 \le n_{jet} \le 3$ and $n_b^{reco} = 2$

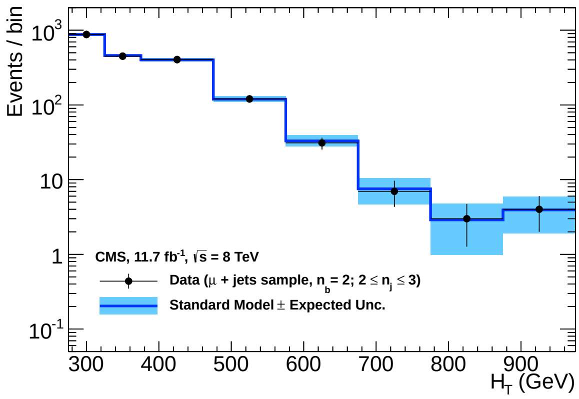

(b) μ + jets sample, $2 \le n_{jet} \le 3$ and $n_b^{reco} = 2$

Figure 5.3.: Comparison of the observed yields and SM expectations given by the simultaneous fit in bins of H_T for the (a) hadronic, (b) μ + jets, (c) $\mu\mu$ + jets and (d) γ + jets samples when requiring $n_b^{reco} = 2$ and $n_{jet} \le 3$. The observed event yields in data (black dots) and the expectations and their uncertainties for all SM processes (blue line with light blue bands) are shown. An example signal expectation (red solid line) for the $D2$ SMS signal point from Table 4.1 is superimposed on the SM background expectation.

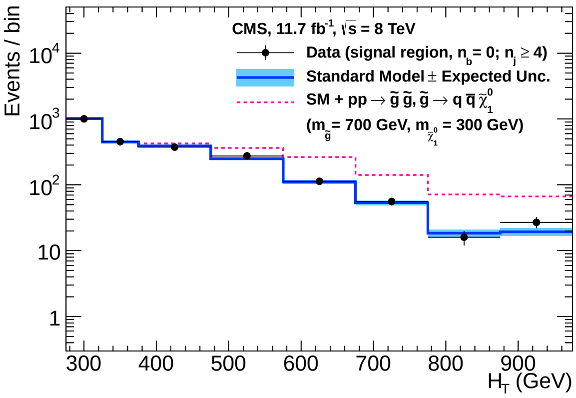

(a) Hadronic sample, $n_{jet} \geq 4$ and $n_b^{reco} = 0$

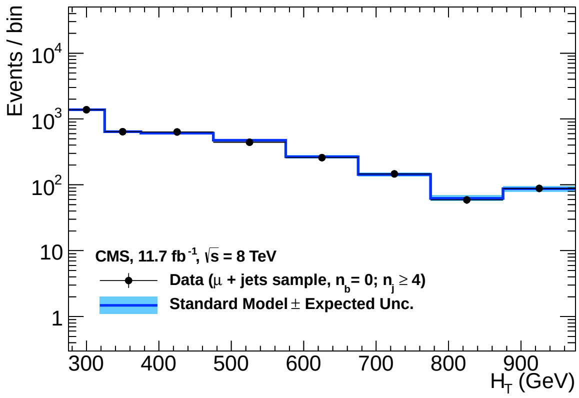

(b) μ + jets sample, $n_{jet} \geq 4$ and $n_b^{reco} = 0$

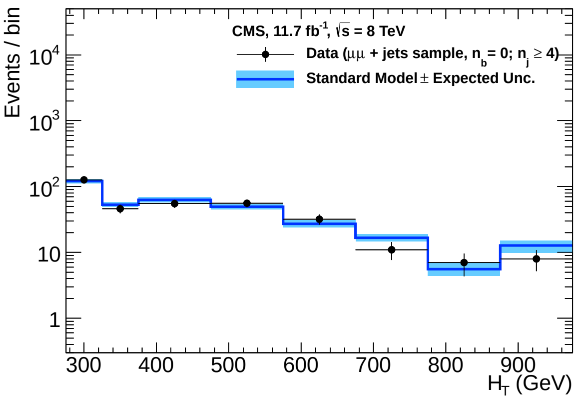

(c) $\mu\mu$ + jets sample, $n_{jet} \geq 4$ and $n_b^{reco} = 0$

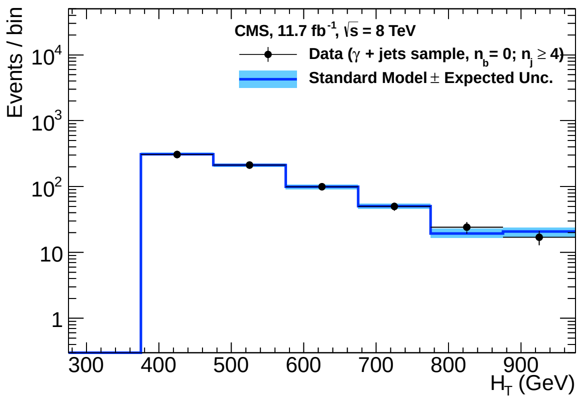

(d) γ + jets sample, $n_{jet} \geq 4$ and $n_b^{reco} = 0$

Figure 5.4.: Comparison of the observed yields and SM expectations given by the simultaneous fit in bins of H_T for the (a) hadronic, (b) μ + jets, (c) $\mu\mu$ + jets and (d) γ + jets samples when requiring $n_b^{reco} = 0$ and $n_{jet} \geq 4$. The observed event yields in data (black dots) and the expectations and their uncertainties for all SM processes (blue line with light blue bands) are shown. An example signal expectation (red solid line) for the $D2$ SMS signal point from Table 4.1 is superimposed on the SM background expectation.

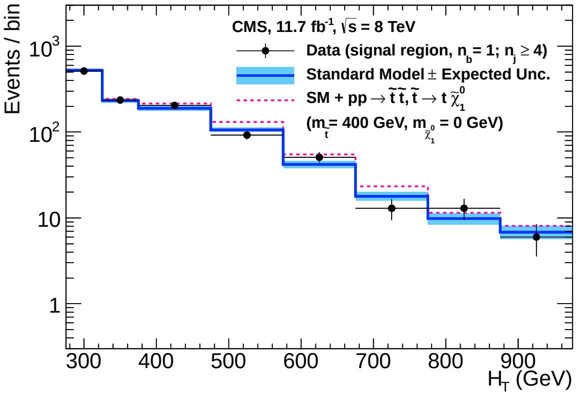

(a) Hadronic sample, $n_{jet} \geq 4$ and $n_b^{reco} = 1$

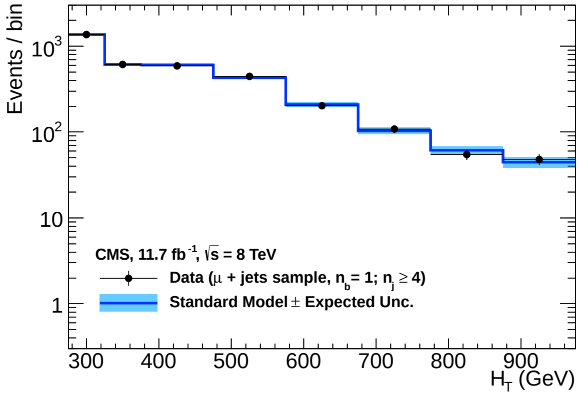

(b) μ + jets sample, $n_{jet} \geq 4$ and $n_b^{reco} = 1$

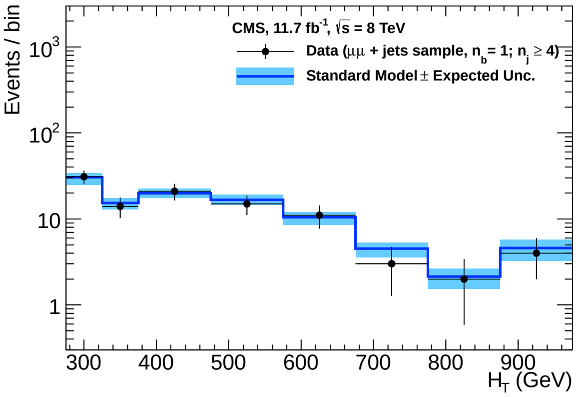

(c) $\mu\mu$ + jets sample, $n_{jet} \geq 4$ and $n_b^{reco} = 1$

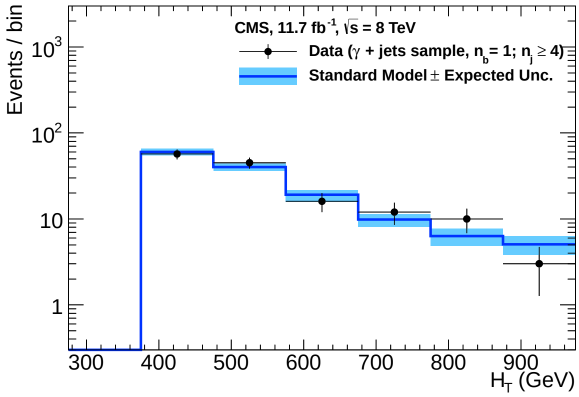

(d) γ + jets sample, $n_{jet} \geq 4$ and $n_b^{reco} = 1$

Figure 5.5.: Comparison of the observed yields and SM expectations given by the simultaneous fit in bins of H_T for the (a) hadronic, (b) μ + jets, (c) $\mu\mu$ + jets and (d) γ + jets samples when requiring $n_b^{reco} = 1$ and $n_{jet} \geq 4$. The observed event yields in data (black dots) and the expectations and their uncertainties for all SM processes (blue line with light blue bands) are shown.

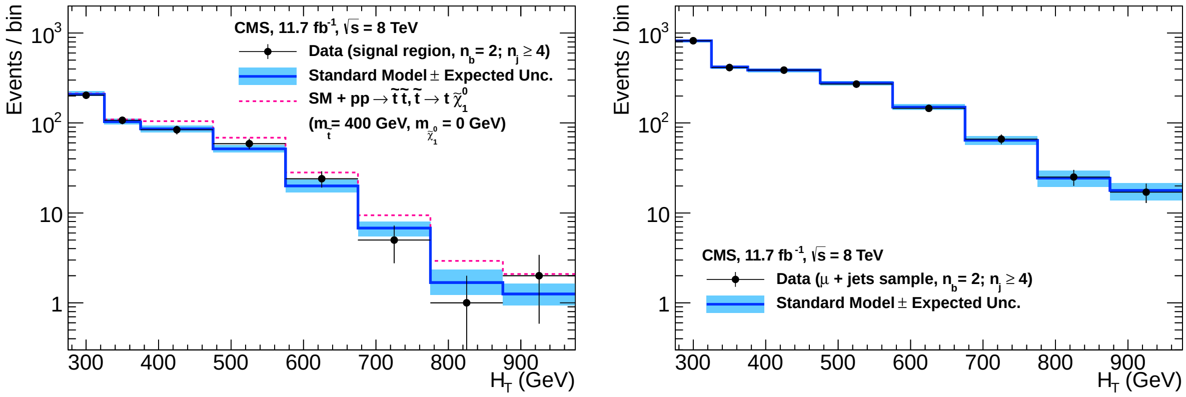

(a) Hadronic sample, $n_{jet} \geq 4$ and $n_b^{reco} = 2$ (b) μ + jets sample, $n_{jet} \geq 4$ and $n_b^{reco} = 2$

Figure 5.6.: Comparison of the observed yields and SM expectations given by the simultaneous fit in bins of H_T for the (a) hadronic, (b) μ + jets, (c) $\mu\mu$ + jets and (d) γ + jets samples when requiring $n_b^{reco} = 2$ and $n_{jet} \geq 4$. The observed event yields in data (black dots) and the expectations and their uncertainties for all SM processes (blue line with light blue bands) are shown. An example signal expectation (red solid line) for the $D3$ SMS signal point from Table 4.1 is superimposed on the SM background expectation.

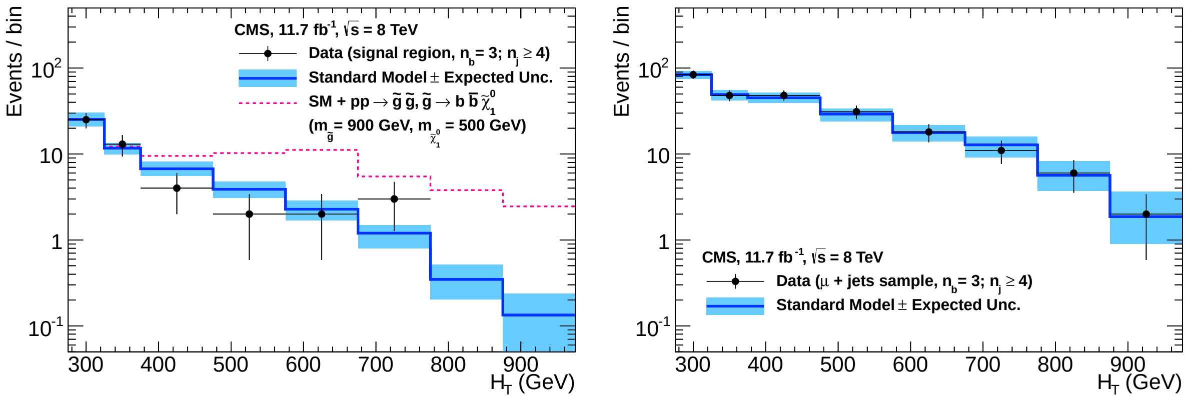

(a) Hadronic sample, $n_{jet} \geq 4$ and $n_b^{reco} = 3$ (b) μ + jets sample, $n_{jet} \geq 4$ and $n_b^{reco} = 3$

Figure 5.7.: Comparison of the observed yields and SM expectations given by the simultaneous fit in bins of H_T for the (a) hadronic, (b) μ + jets, (c) $\mu\mu$ + jets and (d) γ + jets samples when requiring $n_b^{reco} = 3$ and $n_{jet} \geq 4$. The observed event yields in data (black dots) and the expectations and their uncertainties for all SM processes (blue line with light blue bands) are shown. An example signal expectation (red solid line) for the $G2$ SMS signal point from Table 4.1 is superimposed on the SM background expectation.

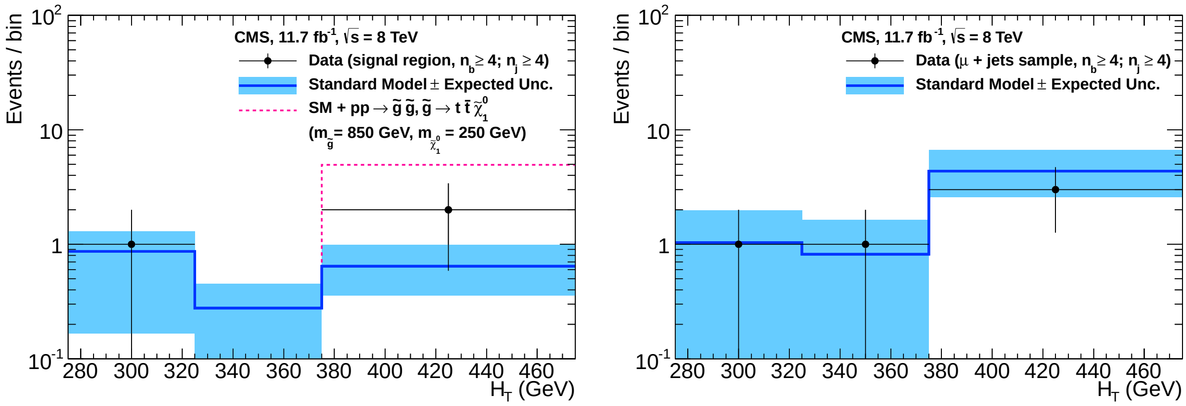

(a) Hadronic sample, $n_{jet} \geq 4$ and $n_b^{reco} \geq 4$ (b) μ + jets sample, $n_{jet} \geq 4$ and $n_b^{reco} \geq 4$

Figure 5.8.: Comparison of the observed yields and SM expectations given by the simultaneous fit in bins of H_T for the (a) hadronic, (b) μ + jets, (c) $\mu\mu$ + jets and (d) γ + jets samples when requiring $n_b^{reco} \geq 4$ and $n_{jet} \geq 4$. The observed event yields in data (black dots) and the expectations and their uncertainties for all SM processes (blue line with light blue bands) are shown. An example signal expectation (red solid line) for the $G3$ SMS signal point from Table 4.1 is superimposed on the SM background expectation.

5.2. SUSY

Limits are set in the parameter space of a set of SMS models that characterise both natural SUSY third generation squark production, and compressed spectra where the mass splitting between the particle and LSP is small, leading to soft final state jets. However as detailed in Section (2.4.1), the individual models are not representative of a real physical SUSY model as only one decay process is considered. Instead these models represent a way to test for signs of specific signatures indicating new physics.

5.2.1. The $\mathrm{CL_s}$ method

The CLs method [93][94][95] is used to compute the limits for signal models, with the one-sided profile likelihood ratio as the test statistic [96].

The test statistic is defined as

$$q(\mu) = \begin{cases} -2\log\lambda(\mu) & \text{when } \mu \geq \hat{\mu}, \\ 0 & \text{otherwise.} \end{cases} \tag{5.1}$$

where

$$\lambda(\mu) = \frac{L(\mu, \theta_\mu)}{L(\hat{\mu}, \hat{\theta})} \tag{5.2}$$

represents the profile likelihood ratio, in which $\mu \equiv f$ from Section (4.8.4), is the parameter characterising the signal strength. $\hat{\mu}$ is defined at the maximum likelihood value, $\hat{\theta}$ the set of maximum likelihood values of the nuisance parameters and θ_μ the set of maximum values of the nuisance parameters for a given value of μ.

When $\mu \equiv f = 1$, the signal model is considered at its nominal production cross section. The distribution of q_μ is built up via the generation of pseudo experiments in order to obtain two distributions for the background (B) and signal plus background (S+B) cases.

The compatibility of a signal model with observations in data is determined by the parameter CL_s,

$$\mathrm{CL}_S = \frac{\mathrm{CL}_{S+B}}{\mathrm{CL}_B}, \tag{5.3}$$

with CL_B and CL_{S+B} defined as one minus the quantiles of the observed value in the data of the two distributions. A model is considered to be excluded at 95% confidence level when $\mathrm{CL}_s \leq 0.05$ [97].

5.2.2. Interpretation in simplified signal models

Different n_{jet} and $n_{\mathrm{b}}^{\mathrm{reco}}$ bins are used in the interpretation of different SMS models. The choice of the categories used within each interpretation, are made to maximise the signal to background ratio, increasing sensitivity to that particular type of final state signature. The production and decay modes of the SMS models under consideration are summarised in Table 5.3, with limit plots of the experimental reach in these models shown in Figure 5.10.

The models `T1` and `T2` are used to characterise the pair production of gluinos and first or second generation squarks, respectively, with parameters for the sparticle mass as well as on the LSP mass. The low number of third generation quarks produced from this decay topology makes choosing to interpret within the $n_{\mathrm{b}}^{\mathrm{reco}} = 0$ category beneficial to improving sensitivity to these models

Conversely the `T2bb`, `T1tttt`, and `T1bbbb` SMS model describe various production and decay mechanisms in the context of third-generation squarks. In this situation considering only higher $n_{\mathrm{b}}^{\mathrm{reco}}$ categories, bring significant improvements to the sensitivity to these types of final state signature.

Finally the choice of jet category is made dependant upon the production mechanism, where gluino induced and direct squark production results in a large or small number of final state jets respectively.

Experimental uncertainties on the SM background predictions ($10-30\%$, described in Section (4.6.1)), the luminosity measurement (4.4%), and the total acceptance times efficiency of the selection for the considered signal model ($12-18\%$, from Section (4.7)) are included in the calculation of the limit.

Model	Production/decay	n_{jet}	n_b^{reco}	Process	Limit	$\mathrm{m}^{\mathrm{best}}_{\widetilde{q}(\widetilde{g})}$ (GeV)	$\mathrm{m}^{\mathrm{best}}_{\mathrm{LSP}}$ (GeV)
T1	$pp \to \widetilde{g}\widetilde{g}^* \to q\bar{q}\widetilde{\chi}^0_1 q\bar{q}\widetilde{\chi}^0_1$	≥ 4	0	5.9(a)	5.10(a)	~ 950	~ 450
T2	$pp \to \widetilde{q}\widetilde{q}^* \to q\widetilde{\chi}^0_1 \bar{q}\widetilde{\chi}^0_1$	≤ 3	0	5.9(b)	5.10(b)	~ 775	~ 325
T2bb	$pp \to \widetilde{b}\widetilde{b}^* \to b\widetilde{\chi}^0_1 \bar{b}\widetilde{\chi}^0_1$	≤ 3	1,2	5.9(c)	5.10(c)	~ 600	~ 200
T1tttt	$pp \to \widetilde{g}\widetilde{g}^* \to t\bar{t}\widetilde{\chi}^0_1 t\bar{t}\widetilde{\chi}^0_1$	≥ 4	2,3,≥ 4	5.9(d)	5.10(d)	~ 975	~ 325
T1bbbb	$pp \to \widetilde{g}\widetilde{g}^* \to b\bar{b}\widetilde{\chi}^0_1 b\bar{b}\widetilde{\chi}^0_1$	≥ 4	2,3,≥ 4	5.9(e)	5.10(e)	~ 1125	~ 650

Table 5.3.: A table representing the SMS models interpreted within the analysis. The model name and production and decay chain is specified in the first two columns. Each SMS model is interpreted in specific n_{jet} and n_b^{reco} categories which are detailed in the third and fourth columns. The last two columns indicate the search sensitivity for each model, representing the largest $m_{\widetilde{q}/\widetilde{g}}$ mass beyond which no limit can be set for this particular decay topology. The quotes values are conservatively determined from the observed exclusion based on the theoretical production cross section minus 1σ uncertainty.

Signal efficiency in the kinematic region defined by $0 < m_{\widetilde{g}(\widetilde{q})} < 175$ GeV or $m_{\widetilde{g}(\widetilde{q})} < 300$ GeV is strongly affected by the presence of Initial State Radiation (ISR). This region in which direct (i.e., non-ISR induced) production is kinematically forbidden due to the H_T > 275 GeV requirement, therefore a large percentage of signal acceptance is due to the effect of ISR jets. Given the large associated uncertainties, no interpretation is provided for this kinematic region.

The estimates on mass limits shown in Table 5.3, are determined conservatively from the observed exclusion based on the theoretical production cross section, minus 1σ uncertainty. The most stringent mass limits on pair-produced sparticles are obtained at low LSP masses and larger squark and gluino masses due to the high p_T jets and consequently high H_T of such signal topologies. The limits are seen to weaken for compressed spectra points closer to the diagonal, where the signal is populates the lower H_T bins in which more background resides. For all of the considered models, there is an LSP mass beyond which no limit can be set, which can observed from the figures referenced in the table.

Two small upwards fluctuations are observed within the data, and are seen at high H_T within the $n_{\mathrm{b}}^{\mathrm{reco}} = 0$ category and at mid-H_T in the $n_{\mathrm{b}}^{\mathrm{reco}} = 1$, 2 categories, see Table 5.2. As each of these fluctuations occur within at least one of the analysis categories that each SMS model interpretation is made, the observed exclusions within all SMS models are generally found to be weaker than the expected limits in the region of 1-2 standard deviations. In isolation these fluctuations are not significant and additional data would be necessary to make any further conclusions.

Despite these fluctuations, the range of parameter space that can excluded has been extended with respect to analysis based upon the $\sqrt{s} = 7$ TeV dataset [98], by up to 225 and 150 GeV for $\mathrm{m}^{\mathrm{best}}_{\tilde{q}(\tilde{g})}$ and $\mathrm{m}^{\mathrm{best}}_{LSP}$ respectively. The parameter space for light third generation squarks, the main tenet of natural SUSY models, is increasingly squeezed for larger mass splitting, with exclusions in the region of 1 TeV in these topologies.

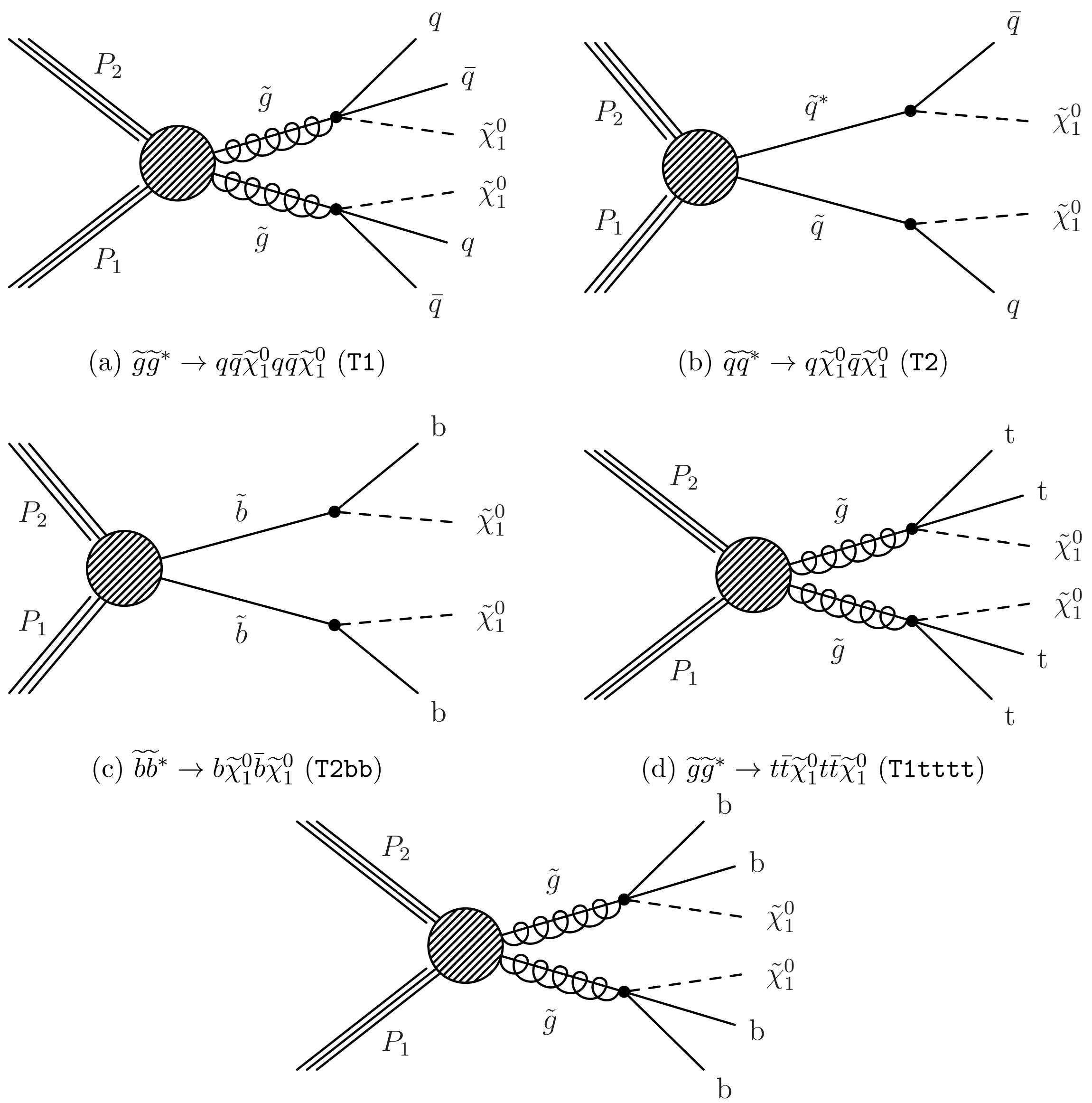

(a) $\widetilde{g}\widetilde{g}^* \to q\bar{q}\widetilde{\chi}_1^0 q\bar{q}\widetilde{\chi}_1^0$ (`T1`) (b) $\widetilde{q}\widetilde{q}^* \to q\widetilde{\chi}_1^0 \bar{q}\widetilde{\chi}_1^0$ (`T2`)

(c) $\widetilde{b}\widetilde{b}^* \to b\widetilde{\chi}_1^0 \bar{b}\widetilde{\chi}_1^0$ (`T2bb`) (d) $\widetilde{g}\widetilde{g}^* \to t\bar{t}\widetilde{\chi}_1^0 t\bar{t}\widetilde{\chi}_1^0$ (`T1tttt`)

(e) $\widetilde{g}\widetilde{g}^* \to b\bar{b}\widetilde{\chi}_1^0 b\bar{b}\widetilde{\chi}_1^0$ (`T1bbbb`)

Figure 5.9.: Production and decay modes for the various SMS models interpreted within the analysis.

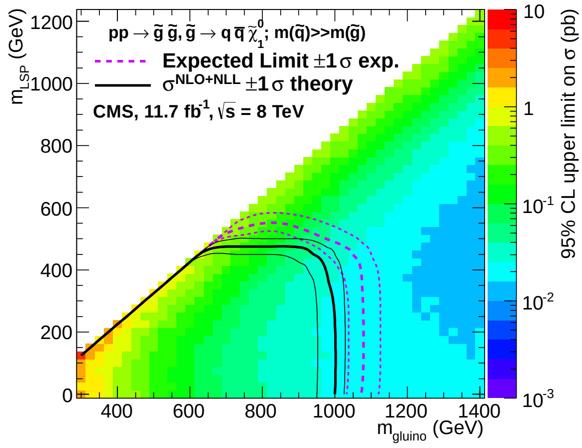

(a) $\widetilde{g}\widetilde{g}^{*} \rightarrow q\bar{q}\widetilde{\chi}_{1}^{0}q\bar{q}\widetilde{\chi}_{1}^{0}$ (T1)

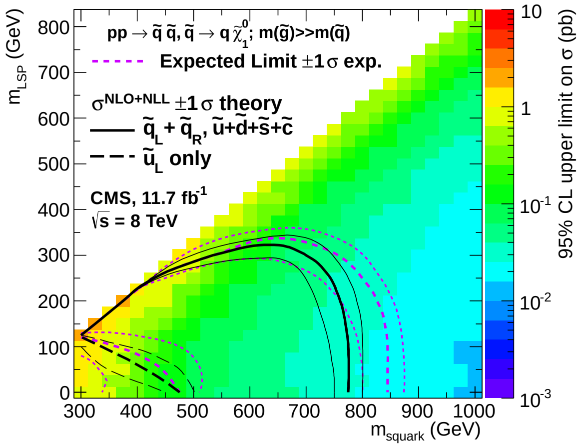

(b) $\widetilde{q}\widetilde{q}^{*} \rightarrow q\widetilde{\chi}_{1}^{0}\bar{q}\widetilde{\chi}_{1}^{0}$ (T2)

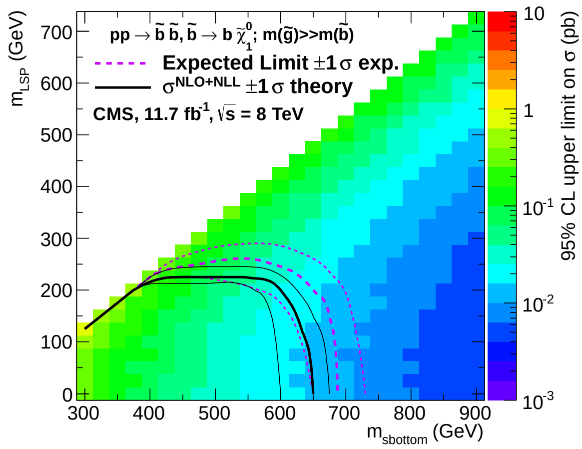

(c) $\widetilde{b}\widetilde{b}^{*} \rightarrow b\widetilde{\chi}_{1}^{0}\bar{b}\widetilde{\chi}_{1}^{0}$ (T2bb)

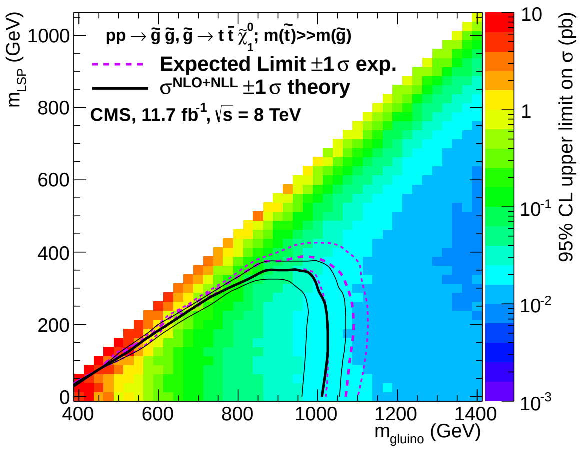

(d) $\widetilde{g}\widetilde{g}^{*} \rightarrow t\bar{t}\widetilde{\chi}_{1}^{0}t\bar{t}\widetilde{\chi}_{1}^{0}$ (T1tttt)

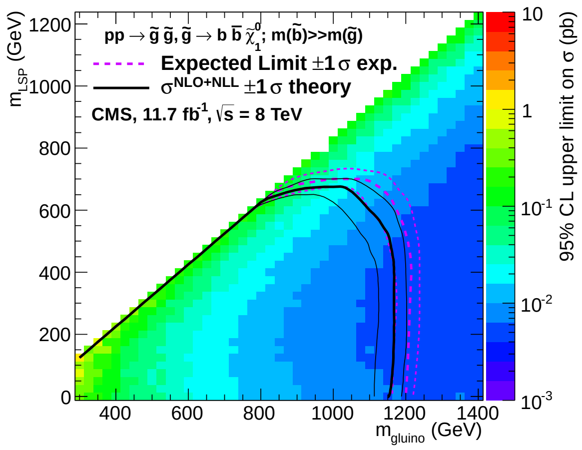

(e) $\widetilde{g}\widetilde{g}^{*} \rightarrow b\bar{b}\widetilde{\chi}_{1}^{0}b\bar{b}\widetilde{\chi}_{1}^{0}$ (T1bbbb)

Figure 5.10.: Upper limit of cross section at 95% CL as a function of $m_{\widetilde{q}/\widetilde{g}}$ and m_{LSP} for various SMS models. The solid thick black line indicates the observed exclusion region assuming NLO and NLL SUSY production cross section. The analysis selection efficiency is measured for each interpreted model, with the signal yield per point given by $\epsilon \times \sigma$. The thin black lines represent the observed excluded region when varying the cross section by its theoretical uncertainty. The dashed purple lines indicate the median (thick line) 1σ (thin lines) expected exclusion regions.

Chapter 6.

Searching For Natural SUSY With B-tag Templates.

Within this chapter a complimentary technique is discussed as a means to predict the distribution of three and four reconstructed b-quark jets in an event. The recent discovery of the Higgs boson has made third-generation "Natural SUSY" models attractive, given that light top and bottom squarks are a candidate to stabilise divergent loop corrections to the Higgs boson mass.

Using the α_T search as a base, a simple template fit is employed to estimate the SM background in higher b-tag multiplicities (3-4) from a fit conducted in a low number of reconstructed b-jets (0-2) control region. As a proof-of-concept, the procedure is applied to the SM enriched μ + jets control sample of the α_T all-hadronic search detailed in Chapter 4, in both data and simulation. To highlight the relative insensitivity of the choice of b-tagging algorithm working point in the effectiveness of the procedure, results are presented using the CSV tagger (introduced in Section (3.3.2)) for the "Loose", "Medium" and "Tight" working points.

6.1. Concept

The dominant SM backgrounds of most SUSY searches are typically $t\bar{t}$ + jets, W + jets, Z $\rightarrow \nu\bar{\nu}$ + jets or other rare processes with neutrinos in the final state. These process are characterised by typically having zero or two underlying b-quarks per event. Conversely a third generation squark production signal, such at the `T1tttt` and `T1bbbb` models described in the previous chapter, will typically have four underlying b-quarks in its final state. As SM processes with similar topologies are rare, an excess of $n_{\mathrm{b}}^{\mathrm{reco}} = 3$, ≥ 4 events would be indicative of a potential natural SUSY signature. Therefore the compatibility of the $n_{\mathrm{b}}^{\mathrm{reco}}$ distribution in data can be tested via the parameterisation of the SM backgrounds in terms of these two most common underlying b-quark topologies.

Typical underlying b-quark content	Process
$= 0$	$W \rightarrow l\nu$ + jets $\mathrm{Z} \rightarrow \nu\bar{\nu}$ + jets $Z/\gamma^{*} \rightarrow \mu\mu$ + jets
$= 1$	t + jets
$= 2$	$t\bar{t}$ + jets

Table 6.1.: Typical underlying b-quark content of different SM processes which are common to many SUSY searches.

Thus two templates are defined, Z0 and Z2 (single top processes are a negligible background, $\sim$1% within the α_T search, and are combined together with $t\bar{t}$) which represent processes which have an underlying b-quark content of zero or two respectively.

Both these templates are generated through the application of the relevant event selection, and can then be taken from the underlying n_b^{reco} distribution directly from simulation. However as discussed within Section (4.5), there are large uncertainties for high n_b^{reco} multiplicities due to limited MC statistics. This is particularly prominent for the Z0 templates, where events with a large number of reconstructed b-tags jets are driven primarily by the mis-tagging of light-quarks. Within both the medium and tight working point of the CSV tagger, the expected mis-tagging rate is only around 1 and 0.1% respectively, leading to large uncertainties in the template shape in this region. Therefore to improve the statistical precision of the predictions within the signal region, the formula method introduced in Section (4.5.1) is used.

The generation of the template shapes, are dependant upon the jet-flavour content and b-tagging rate within the phase space of interest, with the tagging probabilities of a jet being a function of the jet p_T, the pseudo-rapidity $|\eta|$, and jet-flavour. This can be observed in Figure 6.1, where the b-tagging / c-quark mis-tagging / light mis-tagging efficiency for the three working points of the CSV tagger are shown as a function of jet p_T.

Before the template shapes are determined and applied to data, the relevant jet p_T and η corrections are applied to correct the measured b-tagging rate in simulation to that of

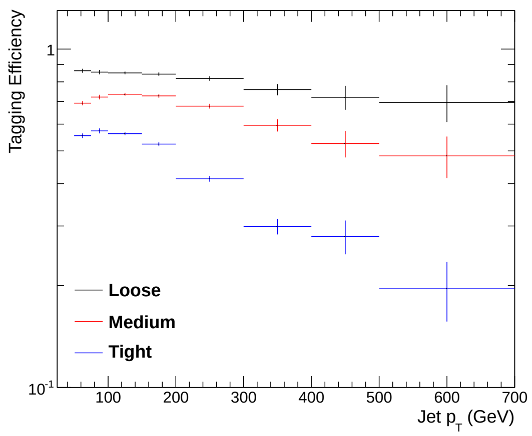

(a) b-jets

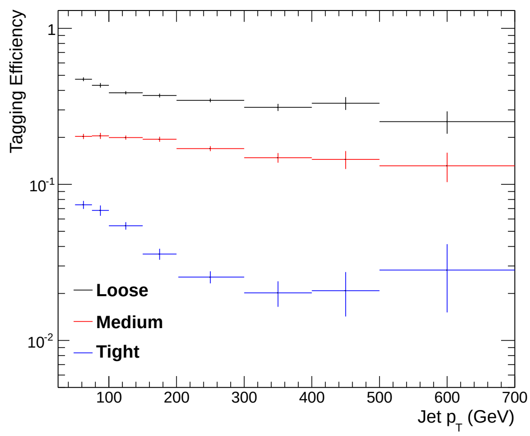

(b) c-jets

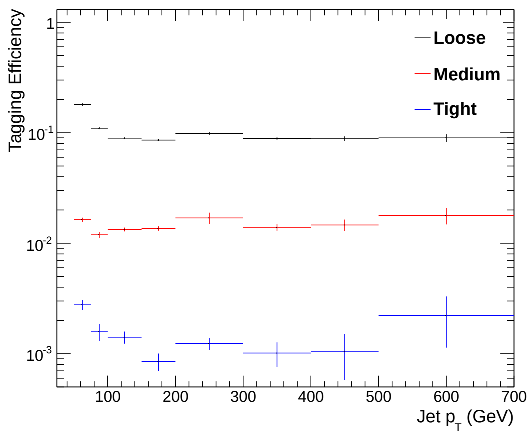

(c) light-jets

Figure 6.1.: The b-tagging (a), c-quark mis-tagging (b), and light-quark mis-tagging rate (c) as measured in simulation after the α_T analysis, μ + jets control sample selection in the region $H_T > 375$.

data, as specified in Section (4.5.3), which propagate through to the average determined b-tagging rates per analysis H_T bin, as in the α_T analysis.

These two template shapes once generated from simulation, can then be fit to data in a low n_b^{reco} control region (0-2). The fit result is used, along with the knowledge of the template shapes, to extrapolate an estimate to the high n_b^{reco} signal region (3,4), which is then compared to what is observed in data. Any large excess in data compared to the template prediction would indicate that the $n_{\mathrm{b}}^{\mathrm{reco}}$ distribution is not adequately described by the SM backgrounds which compose the templates. This method can, in principle, be applied to any analysis where the signal hypothesis has a larger underlying b-quark spectra than the SM backgrounds, as it solely relies on fitting to the shape of the n_b^{reco} distribution.

However in the scenario where a SUSY signal sits at a low number of underlying b-quarks, the template would be unable to discriminate between this signal and background and would be accommodated within the fit in the control region. This will be the case unless the jet p_T distribution of the signal and background were drastically different, in which case there would, anyway be many more sensitive ways to establish the presence of a signal in the data than this method. Indeed the template method is only really applicable to the hypothesis that any signal resides at high $n_{\mathrm{b}}^{\mathrm{reco}}$ and that the control region 0 $\geq n_{\mathrm{b}}^{\mathrm{reco}} \leq 2$ is indeed signal free.

6.2. Application to the α_T Search

As detailed in the previous chapter, the α_T analysis is a search for SUSY particles in all-hadronic final states, utilising the kinematic variable α_T to suppress QCD to a negligible level. SM enriched control samples are used to estimate the background within an all-hadronic signal region.

The selection for the μ + jets control samples defined in Section (4.2.3) is used to demonstrate the template fitting procedure both conceptually in simulation, and also when applied in data. This is chosen, as such a selection is dominated by events stemming from the SM processes with little or no signal contamination from potential new physics. Neither are contributions from rate SM processes with a higher underlying b-quark content (e.g. $t\bar{t}b\bar{b}$) expected. For these reasons, there is a degree of confidence that the procedure should adequately describe the observations in data when extrapolated to the signal region.

The analysis presented here is binning in source jet multiplicity bins, of 3, 4 and ≥ 5 reconstructed jets per event (di-jet events are not included as there is no contribution to the high n_b^{reco} region (3,4)) , in order to reduce the kinematic jet p_T dependence. Furthermore the analysis is split into three H_T regions,

- 275-325 GeV
- 325-375 GeV
- $>$ 375 GeV

contrary to the eight used within the α_T analysis. Templates for both underlying b-quark content hypotheses are then generated for the nine defined analysis bins.

6.2.1. Proof of principle in simulation

In order to demonstrate that the template procedure produces accurate predictions within simulation, the simulation samples in the analysis are firstly split into two to allow for statistically independent fits to be performed.

By combing the relevant ingredients necessary to employ the formula method, $n_{\mathrm{b}}^{\mathrm{reco}}$ templates for Z $= 0$ and Z$= 2$ are generated individually for each n_{jet} and H_T bin using one half of each simulation sample. A fit of these two templates is then performed in the low $n_{\mathrm{b}}^{\mathrm{reco}}$ (0-2) region, back to the sum of the other halves of each simulation sample in order to check that the relevant information can be recovered in the $n_{\mathrm{b}}^{\mathrm{reco}}$ signal region (3-4).

The fits are performed independently within each of the defined analysis bins to reduce the dependence of the shapes of these distributions on simulation. The half of the simulation sample for which the templates are fitted too, are taken directly from simulation, extending this procedure to also be a validation of the formula method in accurately describing the n_b^{reco} distribution within the control region itself. Additionally as this test is performed in simulation, the relevant corrections of the b-tagging rates between data and simulation are *not* applied.

Within Figure 6.2, the results of this fitting procedure are shown for each CSV working point. Results are presented for the $n_{\mathrm{jet}} \geq 5$ category, using the μ + jets control sample selection in the inclusive $H_T > 375$ GeV analysis bin. The grey bands represent the statistical uncertainty on the template shapes. Additional fits are shown for other n_{jet} categories can be found within Appendix D.1.

Furthermore the extrapolated fit predictions within the high n_b^{reco} signal region, are summarised for all H_T bins and working points in Table 6.2.

The pull distributions for all the fits performed can be found in Appendix D.2, and are compatible with a mean of zero and standard deviation of one, showing no obvious bias to the fitting procedure. The good overall agreement summarised in the table validates both the formula method used to generate the templates as well as the method of extrapolation to the high $n_{\mathrm{b}}^{\mathrm{reco}}$ signal region. The application of this method to the same selection in a

H_T	275-325	325-375	>375
Loose working point			
Simulation $n_b = 3$	793.0 ± 14.8	387.9 ± 10.2	794.1 ± 14.34
Template $n_b = 3$	820.4 ± 26.7	376.3 ± 11.9	780.1 ± 15.1
Simulation $n_b = 4$	68.2 ± 3.9	27.6 ± 2.7	91.28 ± 4.9
Template $n_b = 4$	72.5 ± 4.7	28.25 ± 2.34	84.4 ± 3.8
Medium working point			
Simulation $n_b = 3$	133.7 ± 5.7	74.5 ± 4.5	164.2 ± 6.4
Template $n_b = 3$	132.8 ± 4.8	74.5 ± 3.9	159.9 ± 5.7
Simulation $n_b = 4$	1.6 ± 0.6	0.6 ± 0.4	3.4 ± 0.9
Template $n_b = 4$	1.8 ± 0.2	1.1 ± 0.2	4.1 ± 0.4
Tight working point			
Simulation $n_b = 3$	26.9 ± 2.6	13.9 ± 1.9	31.8 ± 2.9
Template $n_b = 3$	24.7 ± 1.5	13.8 ± 1.2	28.1 ± 1.5
Simulation $n_b = 4$	0.5 ± 0.4	-	-
Template $n_b = 4$	0.1 ± 0.1	0.1 ± 0.1	0.2 ± 0.1

Table 6.2.: Summary of the fit predictions in the n_b^{reco} signal region for $n_{jet} = 3, = 4, \geq 5$. The fit region is $n_b^{reco} = 0$, 1, 2 and simulation yields are normalised to an integrated luminosity of 10 fb^{-1}. The uncertainties quoted on the template yields are purely statistical.

data control sample, is now used to demonstrate necessary control over the efficiency and mis-tagging rates when b-tagging scale factors are applied, and to test the assumption of no signal contamination with the μ + jets control sample.

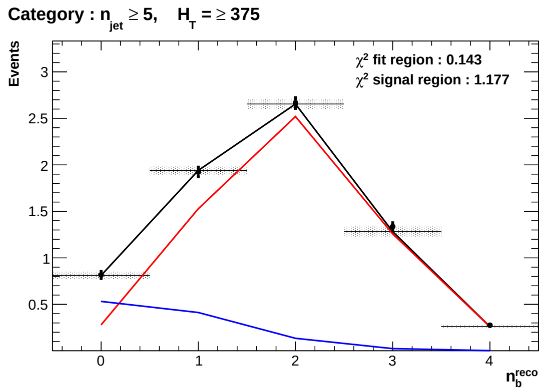

(a) Loose working point : $n_{jet} \geq 5$

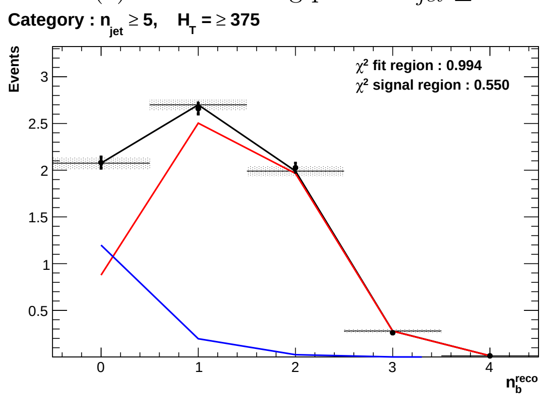

(b) Medium working point : $n_{jet} \geq = 5$

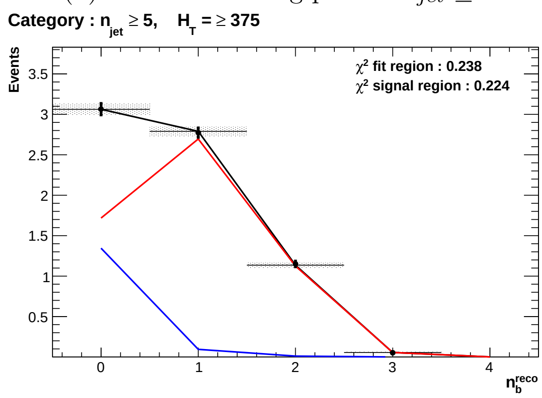

(c) Tight working point : $n_{jet} \geq 5$

Figure 6.2.: The results of fitting the Z = 0 and Z = 2 templates to the $n_b^{reco} = 0, 1, 2$ bins taken directly from simulation in the region $H_T > 375$ GeV, for the $n_{jet} \geq 5$ category. The blue template represents Z = 0, while the red template represents Z = 2. Grey bands represent the statistical uncertainty of the fit. The χ^2 parameter displayed represents the goodness of fit to the lown_b^{reco} (0-2) control region.

6.2.2. Results in a data control sample

The procedure is now applied to the 2012 8 TeV dataset in the μ + jets control sample, to establish the validity of this method in data. The relevant data to simulation b-tagging scale factors are applied to produce corrected values of the efficiency and mis-tagging rates within each analysis bin [86].

Figure 6.3 shows the results of the templates derived from simulation to each of the three defined H_T bins, in the $n_{jet} \geq 5$ category for the medium working point CSV tagger (the same working point used within the α_T analysis). Grey bands represent the statistical uncertainty of the fit combined in quadrature with the systematic uncertainties of varying the data to simulation scale factors up and down by their measured systematic uncertainties. Additional fit results for other jet multiplicities are found in Appendix D.3

The numerical results and extrapolation to the n_b^{reco} =3, 4 bins for all H_T and working points is shown in Table 6.3.

H_T	275-325	325-375	>375
	Loose working point		
Data $n_b = 3$	838	394	717
Template $n_b = 3$	861.8 ± 16.7	372.1 ± 10.1	673.2 ± 14.1
Data $n_b = 4$	81	43	81
Template $n_b = 4$	74.5 ± 2.3	27.6 ± 1.2	71.6 ± 2.6
	Medium working point		
Data $n_b = 3$	137	79	152
Template $n_b = 3$	131.2 ± 2.3	65.1 ± 1.7	127.8 ± 2.4
Data $n_b = 4$	1	1	3
Template $n_b = 4$	1.8 ± 0.1	0.9 ± 0.1	3.1 ± 0.1
	Tight working point		
Data $n_b = 3$	24	15	25
Template $n_b = 3$	23.0 ± 0.4	10.9 ± 0.3	20.3 ± 0.5
Data $n_b = 4$	0	0	1
Template $n_b = 4$	0.1 ± 0.1	0.1 ± 0.1	0.2 ± 0.1

Table 6.3.: Summary of the fit predictions in the n_b^{reco} signal region of the μ + jets control sample, for $n_{jet} = 3, = 4, \geq 5$. The fit region is n_b^{reco} = 0, 1, 2 using 11.4 fb^{-1} of data at $\sqrt{s} = 8$TeV. The uncertainties quoted on the template yields are purely statistical.

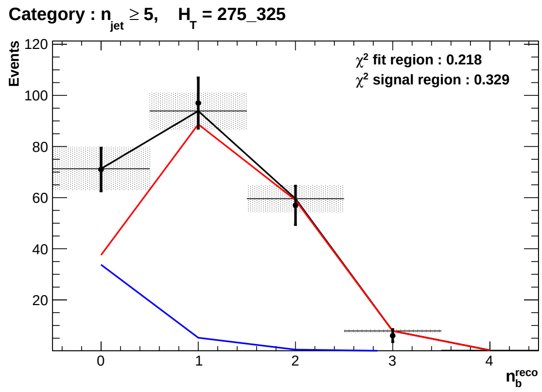

(a) $n_{jet} \geq 5$, $275 < H_T < 325$

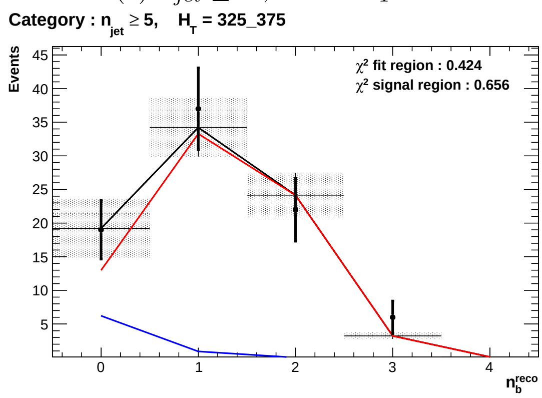

(b) $n_{jet} \geq = 5$, $325 < H_T < 375$

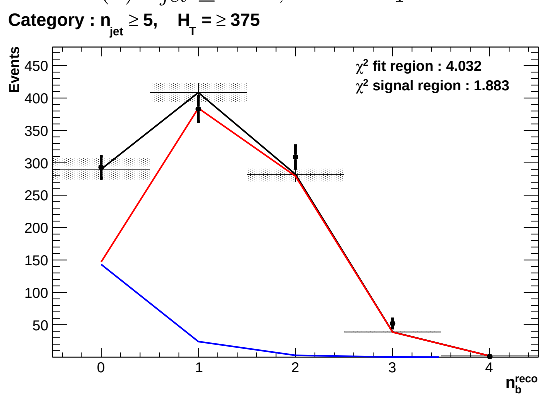

(c) $n_{jet} \geq 5$, $H_T > 375$

Figure 6.3.: The results of fitting the Z = 0 and Z = 2 templates to the $n_b^{reco} = 0, 1, 2$ bins taken directly from data, for the $n_{jet} \geq 5$ category and medium CSV working point. The blue template represents Z = 0, while the red template represents Z = 2. The χ^2 parameter displayed represents the goodness of fit to the low n_b^{reco} (0-2) control region.

When this method is applied to the μ + jets control sample, it is expected that good agreement would be observed between prediction and observation (in the absence of signal contamination) if the procedure is valid. The good compatibility for all working points as shown in the table, demonstrate that this is the case. However no such assumptions can be made when applied to the signal region of the α_T search.

6.2.3. Application to the α_T hadronic search region

As an accompaniment to the background estimation methods outlined by the α_T search. The b-tag template method offers a complimentary way of testing the SM only background hypothesis within the hadronic signal region of the search. In the presence of a natural SUSY signature containing four underlying $\widetilde{b}$ or $\widetilde{t}$ squarks, which subsequently decay to t or b quarks, the number of reconstructed $n_{\mathrm{b}}^{\mathrm{reco}} = 3, \geq 4$ events will be enhanced.

Figure 6.4 show the the results of the templates derived from simulation to each of the three CSV working points, in the $n_{jet} \geq 5$, $H_T > 375$ GeV category. Grey bands represent the statistical uncertainty of the fit combined in quadrature with the systematic uncertainties of varying the data to simulation scale factors up and down by their measured systematic uncertainties. Additional fit results for other jet multiplicities are found in Appendix D.4

The numerical results and extrapolation to the n_b^{reco} =3, 4 bins for all H_T and working points are shown in Table 6.4. No excess of data is found and predictions from this method are found to be compatible with the α_T maximum likelihood fit results from Table 5.2.

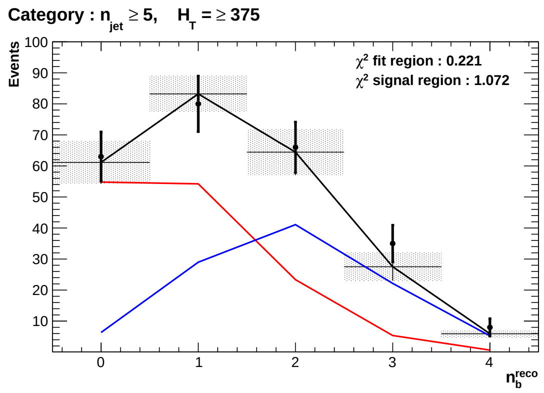

(a) Loose working point : $n_{jet} \geq 5$, $H_T > 375$

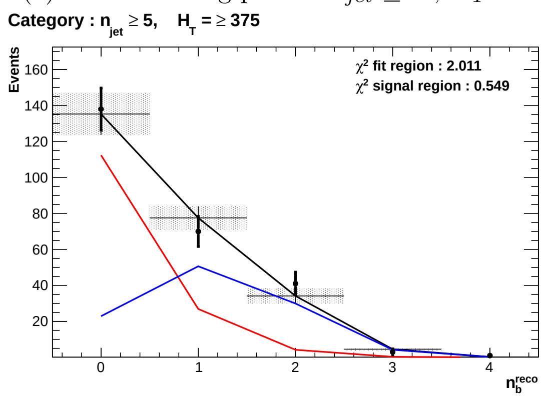

(b) Medium working point : $n_{jet} \geq 5$, $H_T > 375$

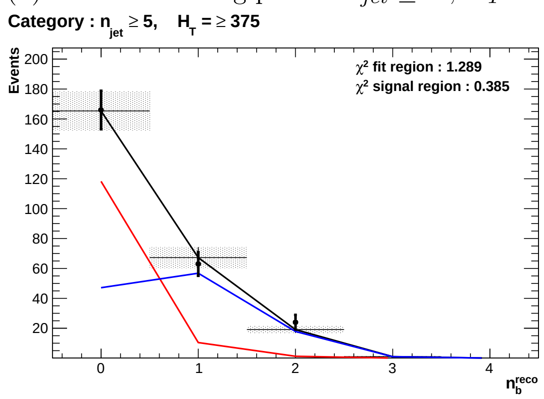

(c) Tight working point : $n_{jet} \geq 5$, $H_T > 375$

Figure 6.4.: The results of fitting the Z = 0 and Z = 2 templates to the $n_b^{reco} = 0, 1, 2$ bins taken from data, in the $n_{jet} \geq 5$ and $H_T > 375$ category for all CSV working points. The blue template represents Z = 0, while the red template represents Z = 2. The χ^2 parameter displayed represents the goodness of fit to the lown_b^{reco} (0-2) control region.

H_T	275-325	325-375	>375
	Loose working point		
Data $n_b = 3$	198	85	126
Template $n_b = 3$	207.1 ± 9.0	103.4 ± 5.9	124.98 ± 7.4
Data $n_b = 4$	15	9	16
Template $n_b = 4$	15.9 ± 1.2	8.05 ± 0.9	13.1 ± 1.3
	Medium working point		
Data $n_b = 3$	28	15	12
Template $n_b = 3$	24.4 ± 0.9	12.7 ± 0.8	19.9 ± 2.4
Data $n_b = 4$	1	0	2
Template $n_b = 4$	0.3 ± 0.2	0.3 ± 0.1	0.5 ± 0.1
	Tight working point		
Data $n_b = 3$	5	2	0
Template $n_b = 3$	4.03 ± 0.2	2.4 ± 0.2	3.1 ± 0.2
Data $n_b = 4$	1	0	0
Template $n_b = 4$	0.1 ± 0.1	0.1 ± 0.1	0.0 ± 0.1

Table 6.4.: Summary of the fit predictions in the n_b^{reco} signal region of the μ + jets control sample, for $n_{jet} = 3, = 4, \geq 5$. The fit region is $n_b^{reco} = 0$, 1, 2 using 11.7 fb^{-1} of data at $\sqrt{s} = 8$TeV. The uncertainties quoted on the template yields are purely statistical.

6.3. Summary

A SUSY signature such as one from gluino-induced third-generation squark production, would result in a final state with an underlying b-quark content greater than two. In order to be able to discriminate such signatures from the SM background, templates are generated based on a parameterisation of the number of the SM processes, where the underlying b-quarks per event is typically zero or two. These templates are then fit to data in a low n_b^{reco} (0-2) control region in order to extrapolate a prediction in a high n_b^{reco} (3-4) signal region. This approach is built upon the assumptions that the defined control region is almost entirely free of any possible signal contamination from either a third generation SUSY signal, or other possible event topologies with a small number of b quarks in the final state.

The method was demonstrated both in simulation and also in data, using the SM enriched μ + jets selection from the α_T search, to prove conceptually and experimentally that the method is valid and there is adequate control over the efficiency and mis-tagging rates in data for all working points of the CSV tagger. Additionally this method was also applied to the α_T analysis signal region, where good agreement is observed between the predictions from the template extrapolations, observations in data and the background estimation method of the α_T analysis.

Chapter 7.

Conclusions

A search for supersymmetry is presented based on a data sample of pp collisions collected at $\sqrt{s} = 8$ TeV, corresponding to an integrated luminosity of 11.7 ± 0.5 fb^{-1}. Final states with two or more jets and significant $\not\!\!E_T$, a typical final state topology of R-parity conserving SUSY models have been analysed and in which the α_T variable is utilised as the main discriminator between balanced multi-jet backgrounds and those with real missing energy. An additional complementary approach using a template method to estimate the b-tag jet distribution of SM processes, to search for gluino induced third generation squark SUSY production is also introduced, in which the α_T search selection is applied in both simulation and data to validate this technique.

Additionally a measurement the performance of the Level-1 trigger for jets and energy sum quantities is also presented. These studies quantify any change in level-1 performance after the introduction of a 5 GeV jet seed threshold into the jet algorithm configuration. This change is introduced to facilitate a reduction in the rate at which jets are formed at level-1 from pile-up jets which are not of interest to physics analyses. This change is necessary to ensure that trigger thresholds can be maintained at lower values, in the presence of an increasing number of pile-up interactions per event over the 2012 run period. No significant change in single jet trigger efficiencies is observed and good performance is observed for a range of level-1 quantities.

Within the SUSY search presented in this analysis, the sum of standard model backgrounds binned in H_T, $n_{\mathrm{b}}^{\mathrm{reco}}$ and n_{jet} categories are estimated from a simultaneous binned likelihood fit to a hadronic signal selection and μ + jets, $\mu\mu$ + jets, and γ + jets control samples. Systematic errors due to theory, detector effects and analysis choices are quantified through the use of data driven closure tests and accounted for in the final interpretation, where observations in data are found to be compatible with a SM only hypothesis.

In the absence of a signal like excess the analysis is further interpreted in a set of SMS models. In the considered models with gluino pair production and for small LSP masses, exclusion limits of the gluino mass are in the range 950-1125 GeV. For SMS models with direct squark pair production, first or second generation squarks are excluded up to around 775 GeV and bottom squarks are excluded up to 600 GeV, again for small LSP masses. In the context of 'natural' SUSY models, with many reconstructed b-jets in the final state, limits are set in the range of 975-1125 GeV again for large mass splittings between the parents squark and the LSP.

The template method, whose purpose is to identify any excess in data arising from third generation signatures, finds results that are compatible with the α_T search and a SM only hypothesis at a high number of reconstructed b-jets. As light third generation squarks are an important feature of 'natural' SUSY models if they are to solve the fine tuning problem [99], the limits imposed through interpretations in the `T1bbbb` and `T1tttt` SMS models within the α_T search, put pressure on such theories, by squeezing the parameter space in which 'natural' SUSY can reside.

Appendix A.

Miscellaneous

A.1. Jet Identification Criteria

For Calo jets the following criteria were applied:

Loose CaloJet Id	
Variable	Definition
$f_{HPD} < 0.98$	Fraction of jet energy contributed from "hottest" HPD, which rejects HCAL noise.
$f_{EM} > 0.01$	Noise from the HCAL is further suppressed by requiring a minimal electromagnetic component to the jet f_{EM}.
$N^{90}_{hits} \geq 2$	Jets that have $> 90\%$ of its energy from a single chanel are rejected, to serve as a safety net that catches jets arising from undiagnosed noisy channels.

Table A.1.: Criteria for a reconstructed jet to pass the loose calorimeter jet id.

For PF jets the following criteria were applied:

Loose PF jet Id	
Variable	Definition
nfhJet < 0.99	Fraction of jet composed of neutral hadrons. HCAL noise tends to populate high values of neutral hadron fraction.
nemfJet < 0.99	Fraction of jet composed of neutral electromagnetic energy. ECAL noise tends to populate high values of neutral EM fraction.
nmultiJet > 1	Number of constituents that jet is composed from.
chfJet > 0	Fraction of jet composed of charged hadrons.
cmultiJet > 0	Number of charged particles that compose jet.
cemfJet < 0.99	Fraction of jet composed of charged electromagnetic energy.

Table A.2.: Criteria for a reconstructed jet to pass the loose PF jet id.

A.2. Primary Vertices

The pileup per event is defined by the number of 'good' reconstructed primary vertices in the event, with each vertex satisfying the following requirements

Good primary vertex requirement	
Variable	Definition
$N_{dof} > 4$	The number of degree of freedom, from the vertex fit to compute the best estimate of the vertex parameters.
$\lvert \Delta z_{vtx} \rvert < 24\text{cm}$	The distance, $\lvert \Delta z_{vex} \rvert$, to the position of the closest HLT primary vertex.
$\rho < 2\text{cm}$	The perpendicular distance of track position to the beam spot.

Table A.3.: Criteria for a vertex in an event to be classified as a 'good' reconstructed primary vertex.

Appendix B.

L1 Jets

B.1. Jet matching efficiencies

The single jet turn-on curves are derived from events independent of wether the leading jet in an event is matched to a Level 1 jet using ΔR matching detailed in Section (3.4.3) or not. These turn-ons are produced from events which are not triggered on jet quantities and therefore it is not guaranteed that the lead jet of an event will be seeded by a Level 1 jet. Figure B.1 shows the particular matching efficiency of a lead jet to a L1 jet.

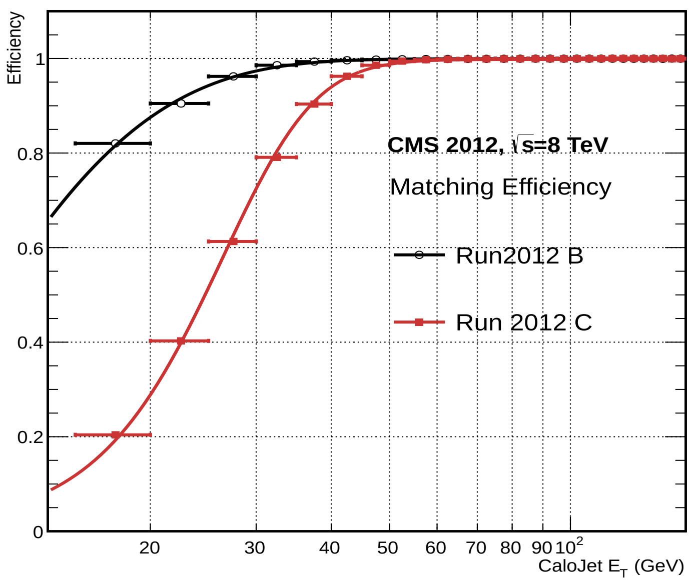

Figure B.1.: Leading jet matching efficiency as a function of the offline CaloJet E_T, measured in an isolated muon triggered dataset in the 2012B and 2012C run periods.

Run Period	μ	σ
2012B	6.62 $\pm$ 0.01	0.79 $\pm$ 0.03
2012C	19.51 $\pm$ 0.03	7.14 $\pm$ 0.02

Table B.1.: Results of a cumulative EMG function fit to the turn-on curves for the matching efficiency of the leading jet in an event to a Level-1 jet in run 2012C and 2012B data, measured in an isolated muon triggered sample. The turn-on point, μ, and resolution, σ, are measured with respect to offline Calo Jet E_T.

It can be seen that the turn on is sharper during the 2012B run period. The seed threshold requirement of a 5 GeV jet seed in run 2012C results in more events in which even the lead offline jet does not have an associated L1 jet. For larger jet E_T thresholds, typical of thresholds used in physics analyses, 100% efficiency is observed, and therefore this effect has no impact to overall physics performance.

The matching efficiencies have a μ values of 6.62 GeV and 19.51 GeV for Run 2012B and 2012C respectively and is shown in Table B.1.

B.2. Leading Jet Energy Resolution

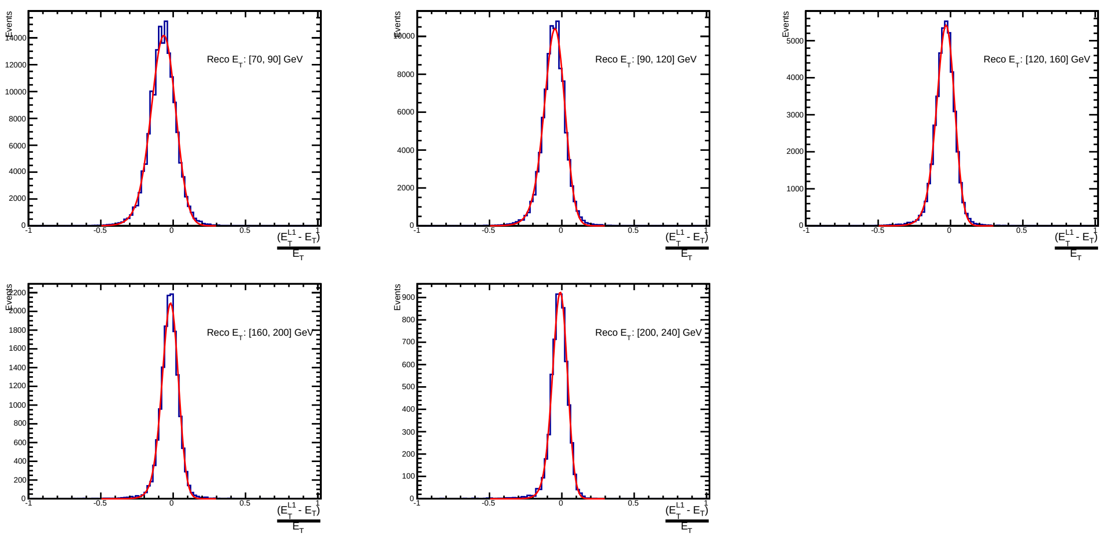

(a)

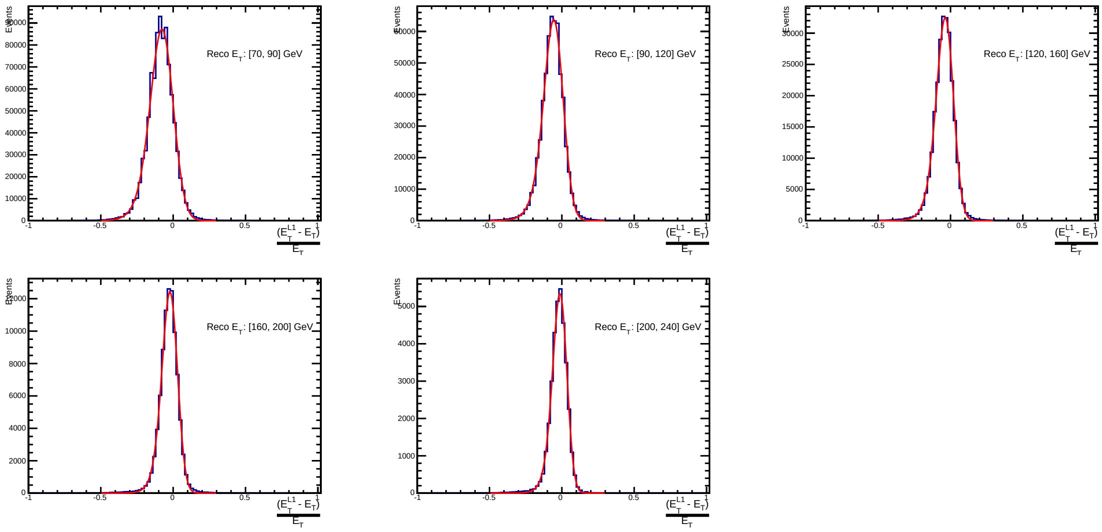

(b)

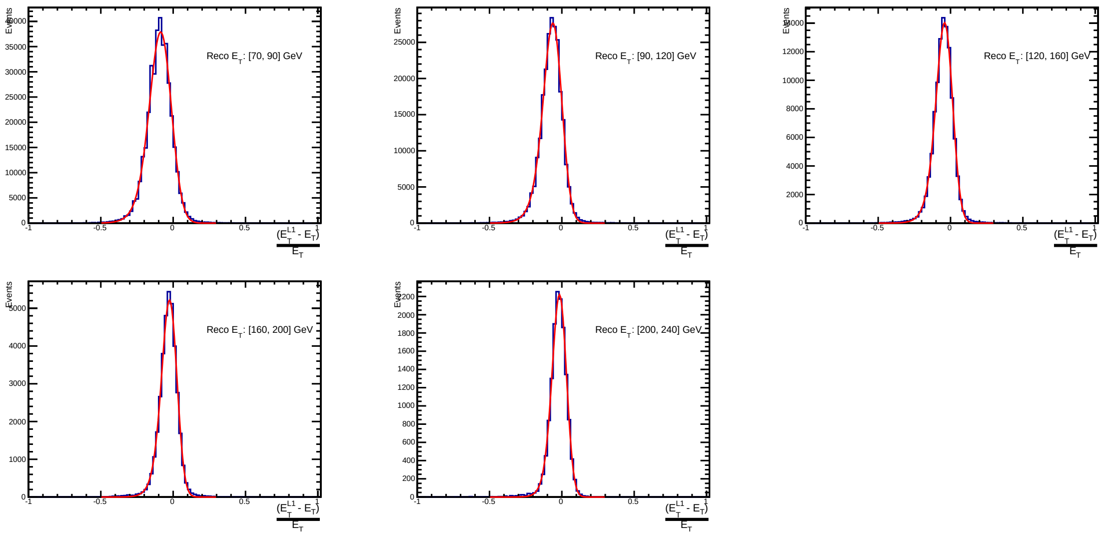

(c)

Figure B.2.: Resolution plots of the leading offline jet Calo E_T measured as a function of $\frac{(\text{L1 E}_T - \text{Offline E}_T)}{\text{Offline E}_T}$ for low (a), medium (b) and high (c) pile-up conditions as defined in Section (3.4.4).

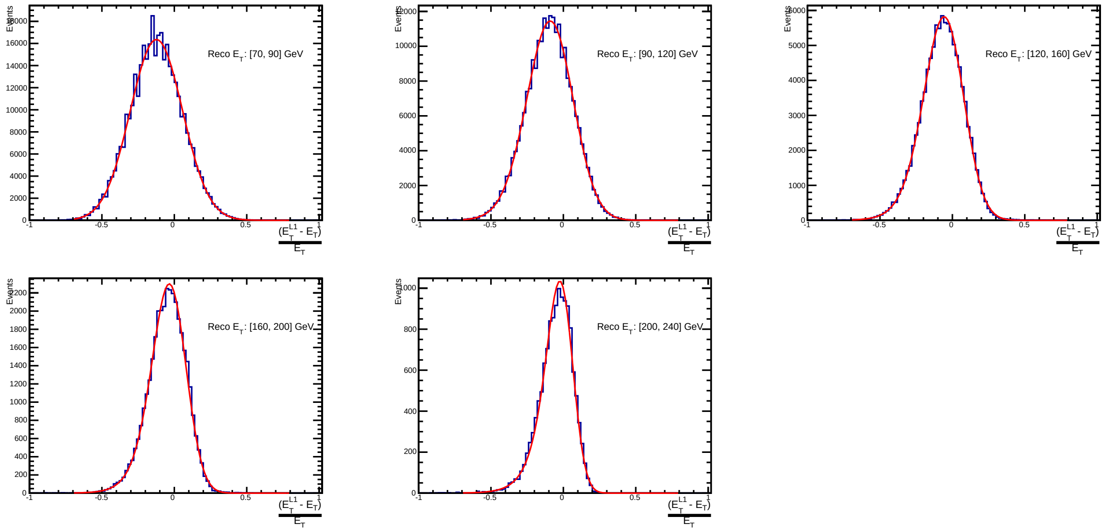
Reco E_T: [70, 90] GeV
Reco E_T: [90, 120] GeV
Reco E_T: [120, 160] GeV
Reco E_T: [160, 200] GeV
Reco E_T: [200, 240] GeV
Events
$\frac{(E_T^{L1} - E_T)}{E_T}$

(a)

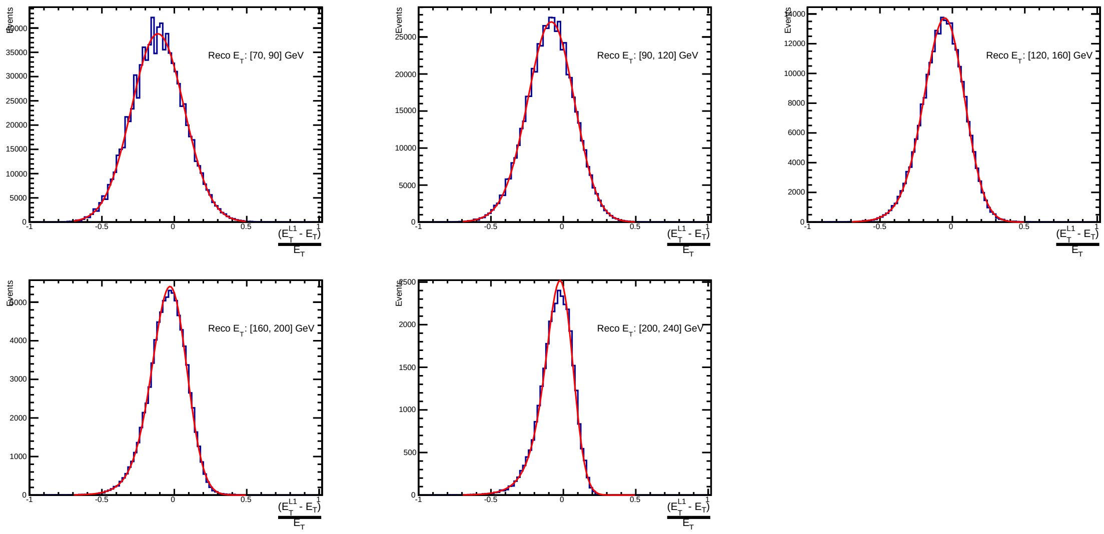
Reco E_T: [70, 90] GeV
Reco E_T: [90, 120] GeV
Reco E_T: [120, 160] GeV
Reco E_T: [160, 200] GeV
Reco E_T: [200, 240] GeV
Events
$\frac{(E_T^{L1} - E_T)}{E_T}$

(b)

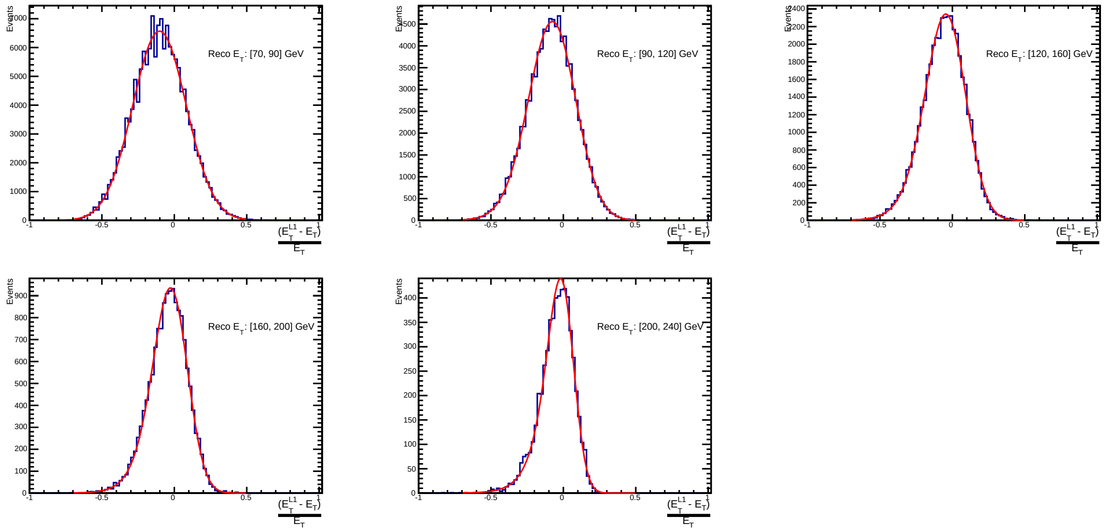

(c)

Figure B.3.: Resolution plots of the leading offline jet PF E_T measured as a function of $\frac{(\text{L1 E}_T - \text{Offline E}_T)}{\text{Offline E}_T}$ for low (a), medium (b) and high (c) pile-up conditions as defined in Section (3.4.4).

B.3. Resolution for Energy Sum Quantities

The following plots show the resolution parameters for energy sum quantities as a function of the quantity (q) itself. In this case, The mean and RMS of the individual $\frac{(\text{L1 q} - \text{Offline q})}{\text{Offline q}}$ distributions, in bins of the quantity q is displayed.

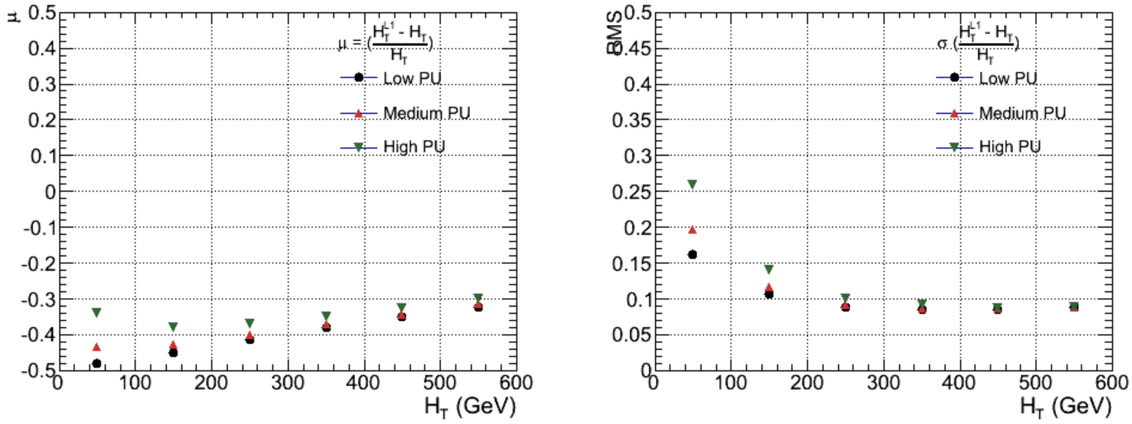

Figure B.4.: H_T resolution parameters in bins of Calo H_T measured for the defined low, medium and high pile up conditions. The plots show the mean μ (left), resolution σ (RMS) of the $\frac{\Delta q}{q}$ distributions.

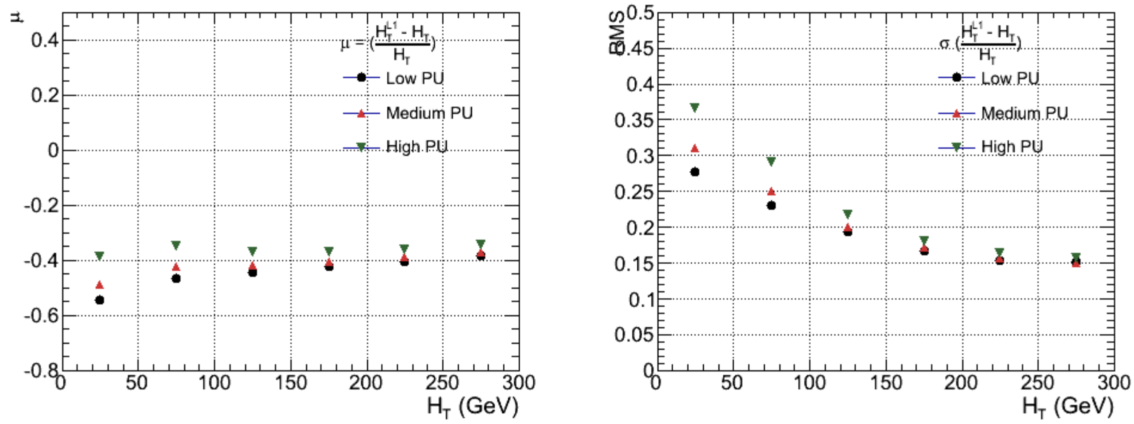

Figure B.5.: H_T resolution parameters in bins of PF H_T measured for the defined low, medium and high pile up conditions. The plots show the mean μ (left), resolution σ (RMS) of the $\frac{\Delta q}{q}$ distributions.

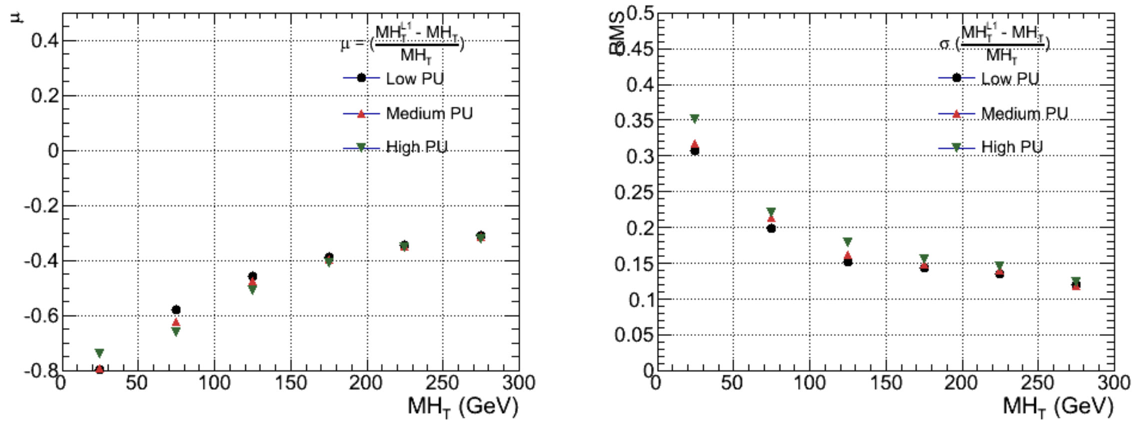

Figure B.6.: $\not{H}_T$ resolution parameters in bins of $\not{H}_T$ measured for the defined low, medium and high pile up conditions. The plots show the mean μ (left), resolution σ (RMS) of the $\frac{\Delta q}{q}$ distributions.

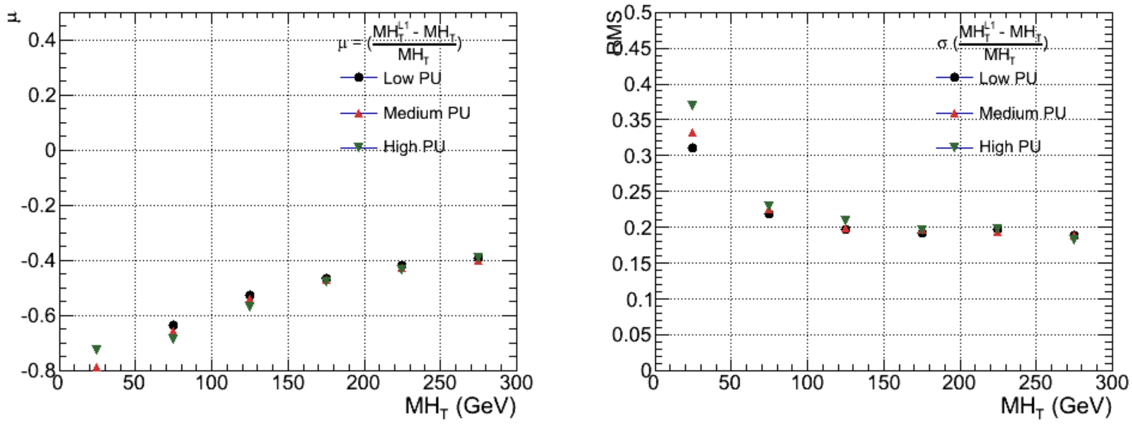

Figure B.7.: $\not{H}_T$ resolution parameters in bins of PF $\not{H}_T$ measured for the defined low, medium and high pile up conditions. The plots show the mean μ (left), resolution σ (RMS) of the $\frac{\Delta q}{q}$ distributions.

Appendix C.

Additional material on background estimation methods

C.1. Determination of k_{QCD}

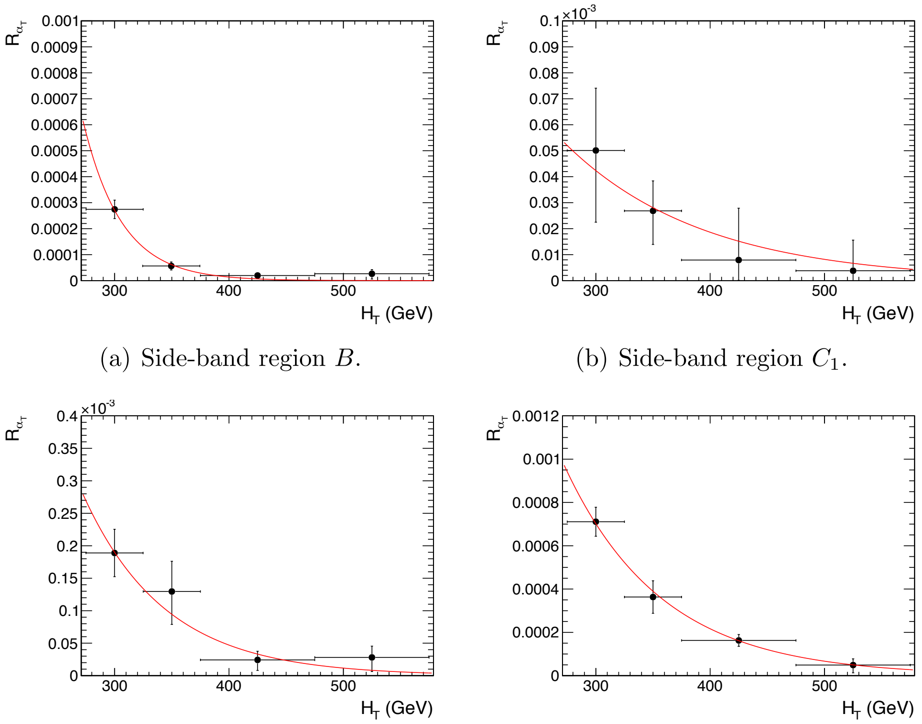

(a) Side-band region B.

(b) Side-band region C_1.

(c) Side-band region C_2.

(d) Side-band region C_3.

Figure C.1.: $R_{\alpha_T}(H_T)$ and exponential fits for each of the data sideband regions. Fit is conducted between the H_T region $275 < H_T < 575$.

C.2. Effect of varying background cross sections on closure tests

Closure tests with cross section variations of +20% and -20% applied to W + jets and $t\bar{t}$ processes respectively.

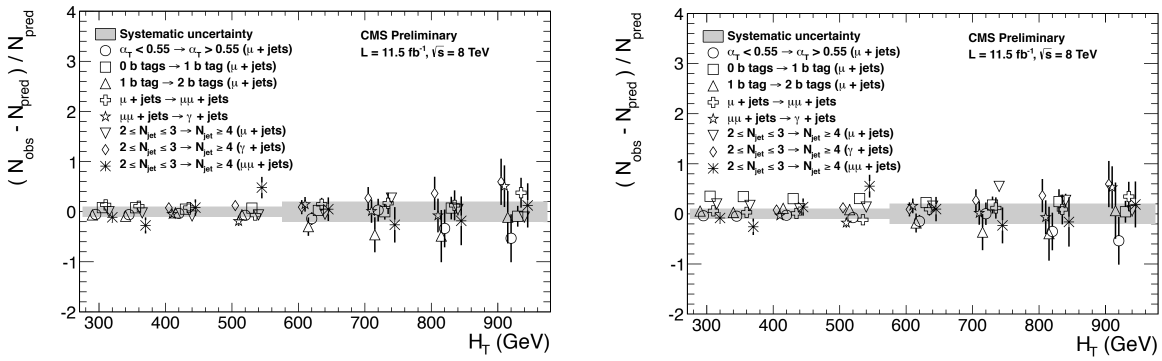

(a) (b)

Figure C.2.: Sets of closure tests (open symbols) overlaid on top of the systematic uncertainty used for each of the five H_T regions (shaded bands) and for the two different jet multiplicity bins:(a) $2 \leq n_{jet} \leq 3$ and (b) $n_{jet} \geq 4$.

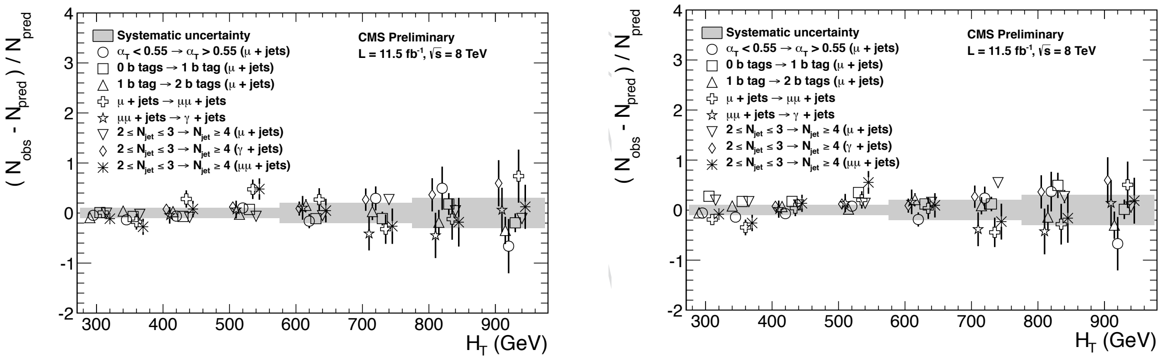

(a) (b)

Figure C.3.: Sets of closure tests (open symbols) overlaid on top of the systematic uncertainty used for each of the five H_T regions (shaded bands) and for the two different jet multiplicity bins:(a) $2 \leq n_{jet} \leq 3$ and (b) $n_{jet} \geq 4$.

		H_T (GeV)			
n_b^{reco}	Cross Section	275–325	325–375	375–475	475–575
0	Nominal	0.303 ± 0.010	0.258 ± 0.007	0.192 ± 0.003	0.148 ± 0.004
0	Varied	0.300 ± 0.010	0.256 ± 0.007	0.191 ± 0.003	0.147 ± 0.004
1	Nominal	0.294 ± 0.005	0.246 ± 0.004	0.189 ± 0.003	0.139 ± 0.003
1	Varied	0.295 ± 0.006	0.248 ± 0.004	0.191 ± 0.003	0.140 ± 0.003
2	Nominal	0.208 ± 0.003	0.183 ± 0.004	0.145 ± 0.003	0.123 ± 0.004
2	Varied	0.211 ± 0.004	0.185 ± 0.004	0.147 ± 0.003	0.124 ± 0.004
3	Nominal	0.214 ± 0.005	0.202 ± 0.007	0.159 ± 0.006	0.140 ± 0.007
3	Varied	0.215 ± 0.005	0.203 ± 0.007	0.159 ± 0.006	0.140 ± 0.007
≥4	Nominal	0.220 ± 0.015	0.245 ± 0.035	0.119 ± 0.009	-
≥4	Varied	0.220 ± 0.015	0.245 ± 0.035	0.119 ± 0.009	-
n_b^{reco}	Cross Section	575–675	675–775	775–875	875–∞
0	Nominal	0.119 ± 0.004	0.098 ± 0.005	0.077 ± 0.006	0.049 ± 0.005
0	Varied	0.120 ± 0.005	0.098 ± 0.006	0.077 ± 0.007	0.049 ± 0.005
1	Nominal	0.115 ± 0.004	0.093 ± 0.005	0.075 ± 0.007	0.063 ± 0.006
1	Varied	0.116 ± 0.004	0.098 ± 0.005	0.081 ± 0.007	0.065 ± 0.006
2	Nominal	0.096 ± 0.005	0.070 ± 0.006	0.051 ± 0.007	0.063 ± 0.008
2	Varied	0.098 ± 0.005	0.073 ± 0.006	0.053 ± 0.007	0.064 ± 0.008
3	Nominal	0.114 ± 0.009	0.065 ± 0.007	0.070 ± 0.017	0.092 ± 0.020
3	Varied	0.114 ± 0.009	0.066 ± 0.007	0.070 ± 0.016	0.093 ± 0.020

Table C.1.: Translation factors constructed from the μ + jets control sample and signal selction MC, to predict yields for the W + jets and $t\bar{t}$ back-grounds in the signal region with (a) NNLO cross sections corrected by k-factors determined from a data sideband see Section (4.4), marked as Nominal, and (b) the same cross sections but with those for W + jets and $t\bar{t}$ varied up and down by 20%, respectively, marked as Varied. No requirement is placed on the jet multiplicity of events within this table.

Appendix D.

Additional Material For B-tag Template Method

D.1. Templates Fits in Simulation

Template fits for the three CSV working points in the $n_{jet} = 3$, $H_T > 375$ category :

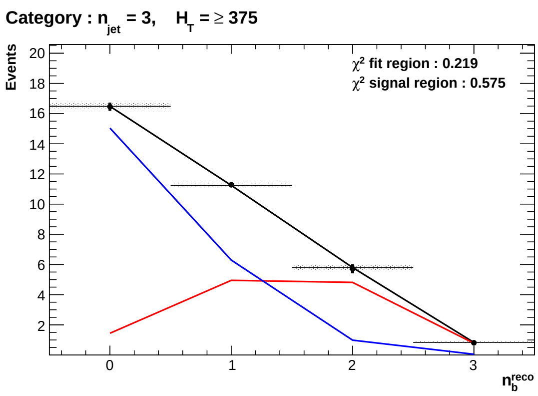

(a) Loose working point $n_{jet} = 3$

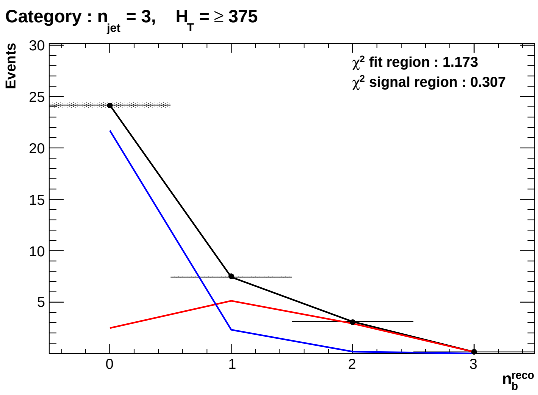

(b) Medium working point $n_{jet} = 3$

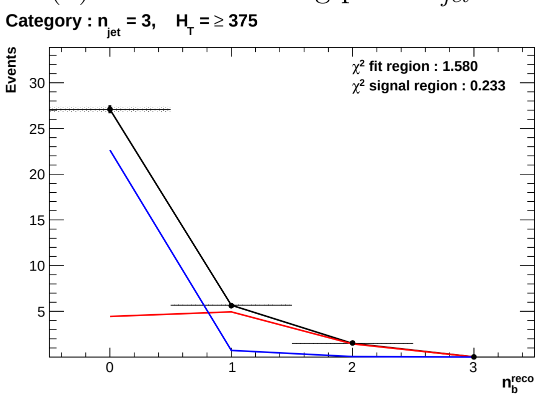

(c) Tight working point $n_{jet} = 3$

Figure D.1.: The results of fitting the Z = 0 and Z = 2 templates to the n_b^{reco} = 0, 1, 2 bins taken directly from simulation in the region $H_T > 375$ GeV, for the $n_{jet} = 3$ category. The blue template represents Z = 0, while the red template represents Z = 2. Grey bands represent the statistical uncertainty of the fit.The χ^2 parameter displayed represents the goodness of fit to the lown_b^{reco} (0-2) control region.

2417 Template fits for the three CSV working points in the $n_{jet} = 4$, $H_T > 375$ category :

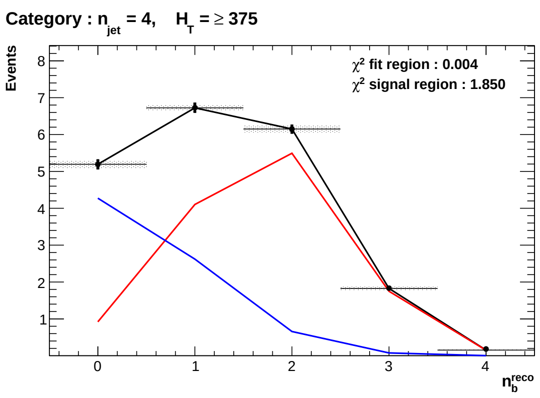

(a) Loose working point $n_{jet} = 4$

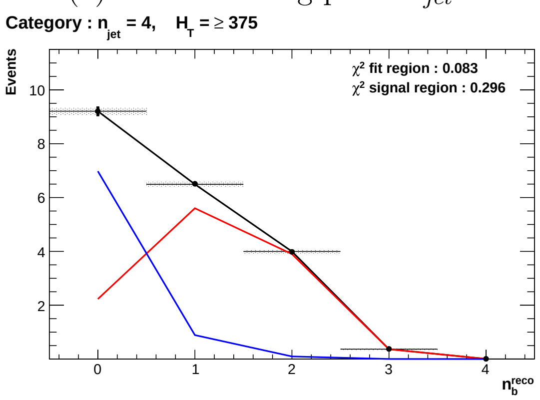

(b) Medium working point $n_{jet} = 4$

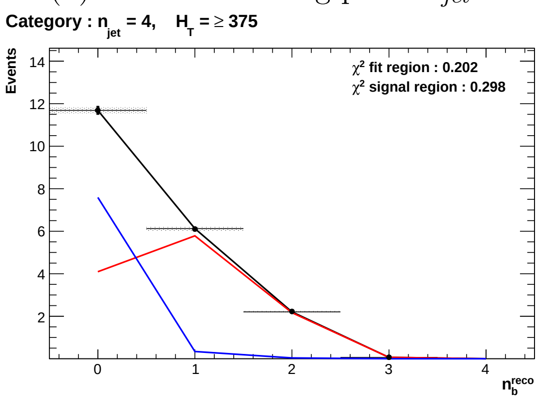

(c) Tight working point $n_{jet} = 4$

Figure D.2.: The results of fitting the Z = 0 and Z = 2 templates to the $n_b^{reco} = 0$, 1, 2 bins taken directly from simulation in the region $H_T > 375$ GeV, for the $n_{jet} = 4$ category. The blue template represents Z = 0, while the red template represents Z = 2. Grey bands represent the statistical uncertainty of the fit.The χ^2 parameter displayed represents the goodness of fit to the lown_b^{reco} (0-2) control region.

D.2. Pull Distributions for Template Fits

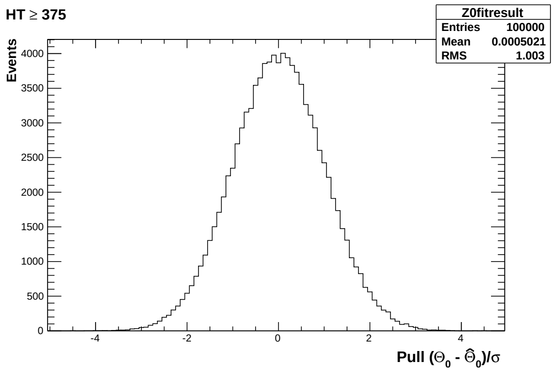

(a) Z0 Template, $H_T > 375$, $n_{jet} = 3$

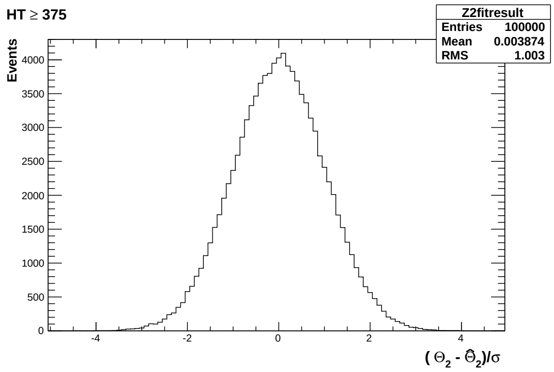

(b) Z2 Template, $H_T > 375$, $n_{jet} = 3$

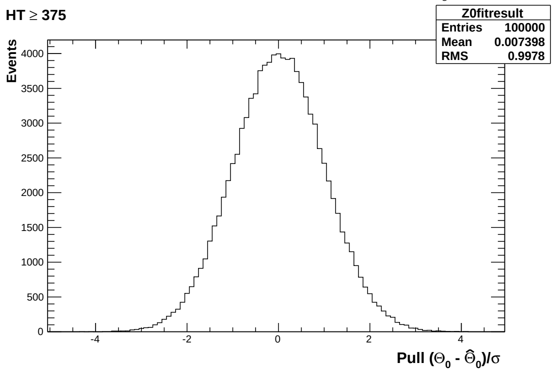

(a) Z0 Template, $H_T > 375$, $n_{jet} = 4$

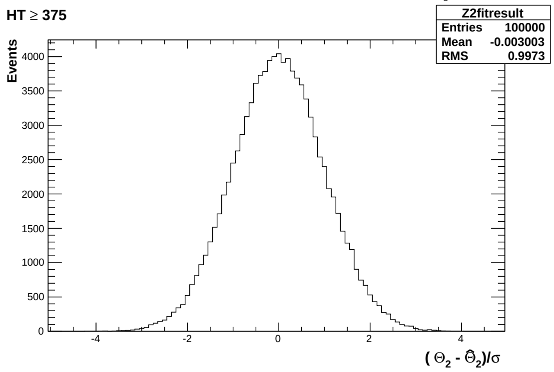

(b) Z2 Template, $H_T > 375$, $n_{jet} = 4$

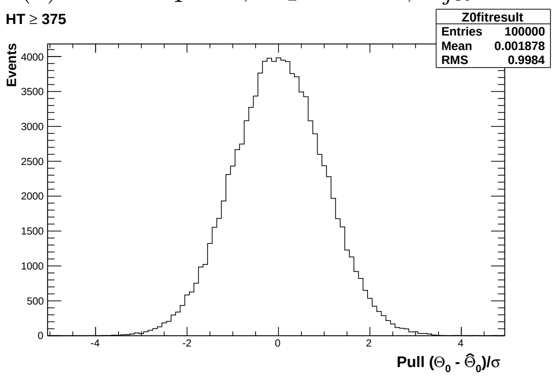

(a) Z0 Template, $H_T > 375$, $n_{jet} \geq 5$

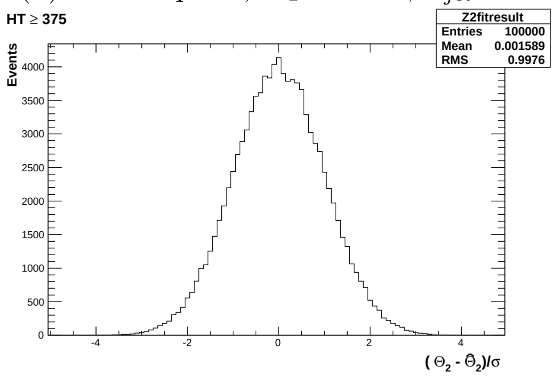

(b) Z2 Template, $H_T > 375$, $n_{jet} \geq 5$

Figure D.3.: Pull distributions of $\frac{(\theta-\hat{\theta})}{\sigma}$ for 10^4 pseudo-experiments generated from a gaussian distribution centred on the n_b^{reco} template values from simulation with width σ. Distributions are shown for both Z0 and Z2 templates for the medium CSV working point.

D.3. Templates Fits in Data Control Sample

Template fits for the three H_T bins, in the $n_{jet} = 3$, medium CSV working point:

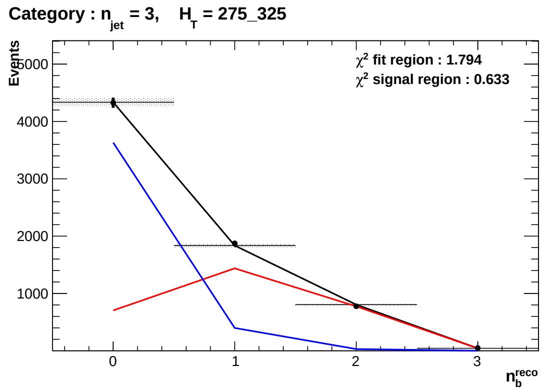

(a) $n_{jet} = 3$, $275 < H_T < 325$

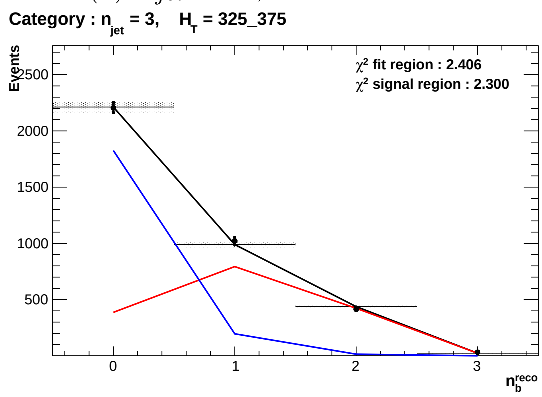

(b) $n_{jet} = 3$, $325 < H_T < 375$

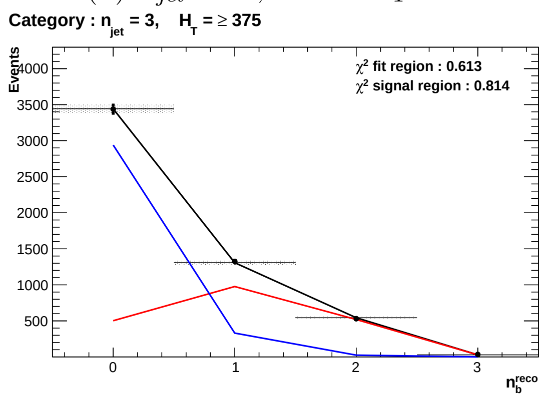

(c) $n_{jet} = 3$, $H_T > 375$

Figure D.4.: The results of fitting the Z = 0 and Z = 2 templates to the $n_b^{reco} = 0, 1, 2$ bins taken from data, for the $n_{jet} = 3$ category and medium CSV working point. The blue template represents Z = 0, while the red template represents Z = 2. The χ^2 parameter displayed represents the goodness of fit to the low n_b^{reco} (0-2) control region.

Template fits for the three H_T bins, in the $n_{jet} = 4$, medium CSV working point:

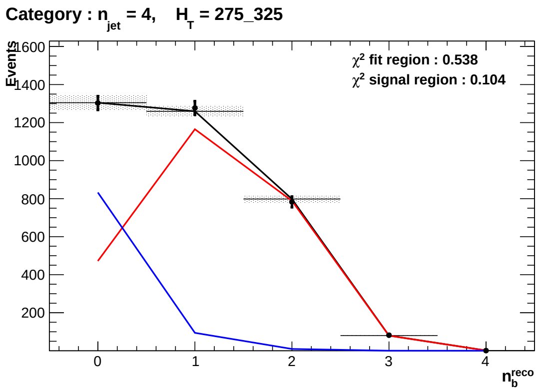

(a) $n_{jet} = 4$, $275 < H_T < 325$

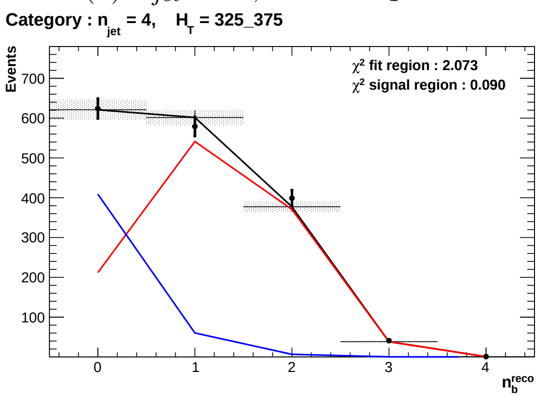

(b) $n_{jet} = 4$, $325 < H_T < 375$

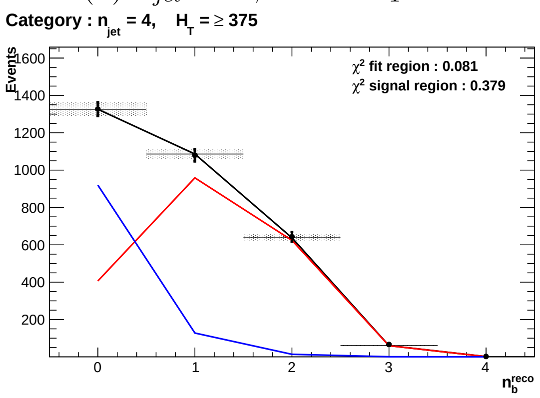

(c) $n_{jet} = 4$, $H_T > 375$

Figure D.5.: The results of fitting the Z = 0 and Z = 2 templates to the $n_b^{reco} = 0$, 1, 2 bins taken from data, for the $n_{jet} = 4$ category and medium CSV working point. The blue template represents Z = 0, while the red template represents Z = 2. The χ^2 parameter displayed represents the goodness of fit to the low n_b^{reco} (0-2) control region.

D.4. Templates Fits in Data Signal Region

Template fits for the three CSV working points, in the $n_{jet} = 3$, $H_T > 375$ category :

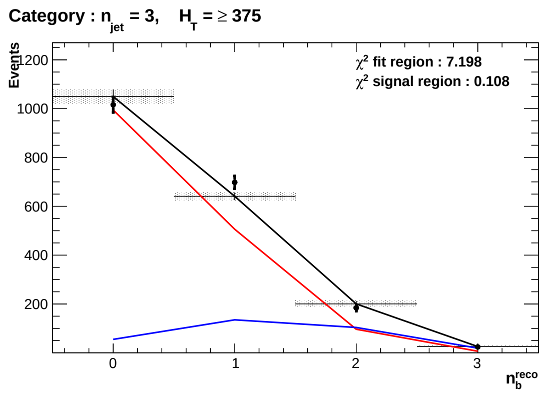

(a) Loose working point : $n_{jet} = 3$, $H_T > 375$

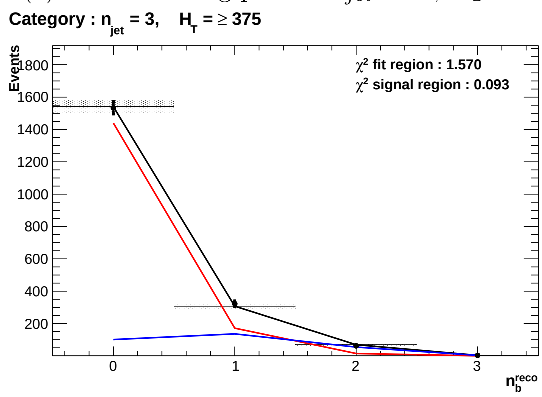

(b) Medium working point : $n_{jet} = 3$, $H_T > 375$

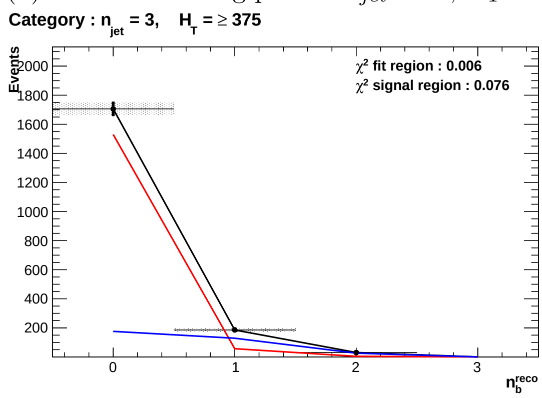

(c) Tight working point : $n_{jet} = 3$, $H_T > 375$

Figure D.6.: The results of fitting the Z = 0 and Z = 2 templates to the $n_b^{reco} = 0, 1, 2$ bins taken from data, in the $n_{jet} = 3$ and $H_T > 375$ category for all CSV working points. The blue template represents Z = 0, while the red template represents Z = 2. The χ^2 parameter displayed represents the goodness of fit to the lown_b^{reco} (0-2) control region.

Template fits for the three CSV working points, in the $n_{jet} = 4$, $H_T > 375$ category :

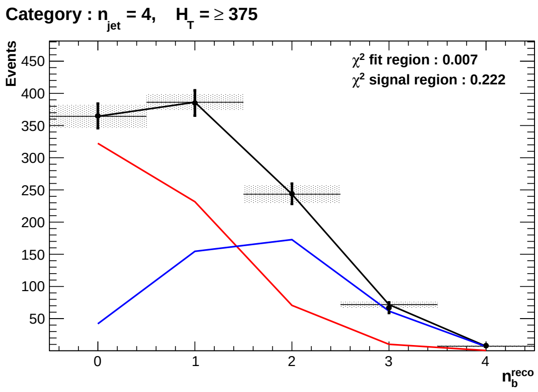

(a) Loose working point : $n_{jet} = 4$, $H_T > 375$

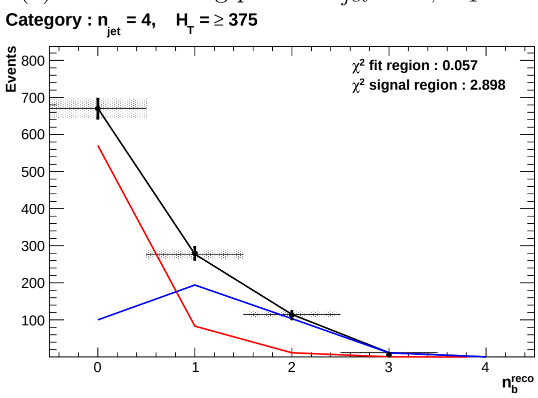

(b) Medium working point : $n_{jet} = 4$, $H_T > 375$

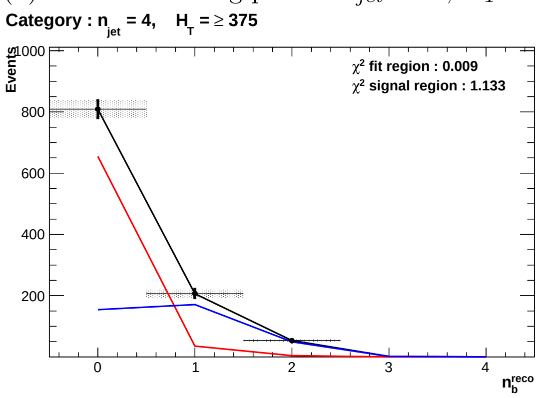

(c) Tight working point : $n_{jet} = 4$, $H_T > 375$

Figure D.7.: The results of fitting the Z = 0 and Z = 2 templates to the $n_b^{reco} = 0, 1, 2$ bins taken from data, in the $n_{jet} = 4$ and $H_T > 375$ category for all CSV working points. The blue template represents Z = 0, while the red template represents Z = 2. The χ^2 parameter displayed represents the goodness of fit to the lown_b^{reco} (0-2) control region.

2425

Bibliography

[1] Particle Data Group Collaboration, "Review of Particle Physics (RPP)", *Phys.Rev.* **D86** (2012) 010001, doi:10.1103/PhysRevD.86.010001.

[2] G. H. et al., "Nine-year Wilkinson Microwave Anisotropy Probe (WMAP) Observations: Cosmological Parameter Results", *The Astrophysical Journal Supplement Series* **208** (2013), no. 2,.

[3] ATLAS Collaboration Collaboration, "Observation of a new particle in the search for the Standard Model Higgs boson with the ATLAS detector at the LHC", *Phys.Lett.* **B716** (2012) 1–29, doi:10.1016/j.physletb.2012.08.020, arXiv:1207.7214.

[4] CMS Collaboration, "Observation of a new boson at a mass of 125 GeV with the CMS experiment at the LHC", *Phys.Lett.* **B716** (2012) 30–61, doi:10.1016/j.physletb.2012.08.021, arXiv:1207.7235.

[5] CMS Collaboration, "Search for supersymmetry in hadronic final states with missing transverse energy using the variables AlphaT and b-quark multiplicity in pp collisions at 8 TeV", *Eur.Phys.J.* **C73** (2013) 2568, doi:10.1140/epjc/s10052-013-2568-6, arXiv:1303.2985.

[6] S. Weinberg, "A Model of Leptons", *Phys. Rev. Lett.* **19** (Nov, 1967) doi:10.1103/PhysRevLett.19.1264.

[7] S. Glashow, "Partial Symmetries of Weak Interactions", *Nucl.Phys.* **22** (1961) doi:10.1016/0029-5582(61)90469-2.

[8] A. Salam, "Weak and Electromagnetic Interactions", *Conf.Proc.* **C680519** (1968).

[9] G. Hooft, "Renormalizable Lagrangians for massive Yang-Mills fields", *Nuclear Physics B* **35** (1971) doi:http://dx.doi.org/10.1016/0550-3213(71)90139-8.

[10] Gargamelle Neutrino Collaboration Collaboration, "Observation of Neutrino Like

Interactions Without Muon Or Electron in the Gargamelle Neutrino Experiment", *Phys.Lett.* **B46** (1973) 138–140, doi:10.1016/0370-2693(73)90499-1.

[11] UA1 Collaboration Collaboration, "Experimental Observation of Lepton Pairs of Invariant Mass Around 95-GeV at the CERN SPS Collider", *Phys.Lett.* **B126** (1983) 398–410, doi:10.1016/0370-2693(83)90188-0.

[12] UA2 Collaboration Collaboration, "Observation of Single Isolated Electrons of High Transverse Momentum in Events with Missing Transverse Energy at the CERN $\bar{p}p$ Collider", *Phys.Lett.* **B122** (1983) doi:10.1016/0370-2693(83)91605-2.

[13] E. Noether, "Invariante Variationsprobleme", *Nachrichten von der Gesellschaft der Wissenschaften zu Gttingen, Mathematisch-Physikalische Klasse* **1918** (1918).

[14] F. Halzen and A. D. Martin, "Quarks and Leptons". 1985.

[15] "Introduction to Elementary Particles". Wiley-VCH, 2nd edition, October, 2008.

[16] C. S. Wu et al., "Experimental Test of Parity Conservation in Beta Decay", *Physical Review* **105** (February, 1957) doi:10.1103/PhysRev.105.1413.

[17] P. Higgs, "Broken symmetries, massless particles and gauge fields", *Physics Letters* **12** (1964), no. 2, doi:http://dx.doi.org/10.1016/0031-9163(64)91136-9.

[18] F. Englert and R. Brout, "Broken Symmetry and the Mass of Gauge Vector Mesons", *Phys. Rev. Lett.* **13** (Aug, 1964) doi:10.1103/PhysRevLett.13.321.

[19] P. W. Higgs, "Broken Symmetries and the Masses of Gauge Bosons", *Phys. Rev. Lett.* **13** (Oct, 1964) doi:10.1103/PhysRevLett.13.508.

[20] G. S. Guralnik, "Global Conservation Laws and Massless Particles", *Phys. Rev. Lett.* **13** (Nov, 1964) doi:10.1103/PhysRevLett.13.585.

[21] S. Weinberg, "A Model of Leptons", *Phys. Rev. Lett.* **19** (Nov, 1967) 1264–1266, doi:10.1103/PhysRevLett.19.1264.

[22] H. Yukawa, "On the Interaction of Elementary Particles. I", *Progress of Theoretical Physics Supplement* **1** (1955) doi:10.1143/PTPS.1.1.

[23] (Super-Kamiokande Collaboration) Collaboration, "Evidence for Oscillation of Atmospheric Neutrinos", *Phys. Rev. Lett.* **81** (Aug, 1998) doi:10.1103/PhysRevLett.81.1562.

[24] R. Becker-Szendy et al., "A Search for muon-neutrino oscillations with the IMB detector", *Phys.Rev.Lett.* **69** (1992) doi:10.1103/PhysRevLett.69.1010.

[25] S. P. Martin, "A Supersymmetry primer", arXiv:hep-ph/9709356.

[26] H. Nilles, "Supersymmetry, Supergravity and Particle Physics". Physics reports. North-Holland Physics Publ., 1984.

[27] H. E. Haber and G. L. Kane, "The Search for Supersymmetry: Probing Physics Beyond the Standard Model", *Phys.Rept.* **117** (1985) doi:10.1016/0370-1573(85)90051-1.

[28] E. Witten, "Dynamical Breaking of Supersymmetry", *Nucl.Phys.* **B188** (1981) doi:10.1016/0550-3213(81)90006-7.

[29] J. Wess and B. Zumino, "Supergauge transformations in four dimensions", *Nuclear Physics B* **70** (1974), no. 1, doi:http://dx.doi.org/10.1016/0550-3213(74)90355-1.

[30] H. Muller-Kirsten and A. Wiedemann, "Introduction to Supersymmetry". World Scientific lecture notes in physics. World Scientific, 2010.

[31] I. Aitchison, "Supersymmetry in Particle Physics: An Elementary Introduction". Cambridge University Press, 2007.

[32] K. A. Intriligator and N. Seiberg, "Lectures on Supersymmetry Breaking", *Class.Quant.Grav.* **24** (2007) arXiv:hep-ph/0702069.

[33] Y. Shadmi, "Supersymmetry breaking", arXiv:hep-th/0601076.

[34] C. Burgess et al., "Warped Supersymmetry Breaking", *JHEP* **0804** (2008) doi:10.1088/1126-6708/2008/04/053, arXiv:hep-th/0610255.

[35] H. Murayama, "Supersymmetry breaking made easy, viable, and generic", arXiv:0709.3041.

[36] H. Baer and X. Tata, "Weak Scale Supersymmetry: From Superfields to Scattering Events". Cambridge University Press, 2006.

[37] S. P. Martin, "Implications of supersymmetric models with natural R-parity conservation", doi:10.1103/PhysRevD.54.2340, arXiv:hep-ph/9602349.

[38] G. L. Kane, C. F. Kolda, L. Roszkowski, and J. D. Wells, "Study of constrained

minimal supersymmetry", *Phys.Rev.* **D49** (1994) doi:10.1103/PhysRevD.49.6173, arXiv:hep-ph/9312272.

[39] C. Strege et al., "Updated global fits of the cMSSM including the latest LHC SUSY and Higgs searches and XENON100 data", *JCAP* **1203** (2012) doi:10.1088/1475-7516/2012/03/030, arXiv:1112.4192.

[40] M. Citron et al., "The End of the CMSSM Coannihilation Strip is Nigh", *Phys.Rev.* **D87** (2013) doi:10.1103/PhysRevD.87.036012, arXiv:1212.2886.

[41] D. Ghosh, M. Guchait, S. Raychaudhuri, and D. Sengupta, "How Constrained is the cMSSM?", *Phys.Rev.* **D86** (2012) doi:10.1103/PhysRevD.86.055007, arXiv:1205.2283.

[42] LHC New Physics Working Group Collaboration, "Simplified Models for LHC New Physics Searches", *J.Phys.* **G39** (2012) 105005, doi:10.1088/0954-3899/39/10/105005, arXiv:1105.2838.

[43] J. Alwall, P. Schuster, and N. Toro, "Simplified Models for a First Characterization of New Physics at the LHC", *Phys.Rev.* **D79** (2009) 075020, doi:10.1103/PhysRevD.79.075020, arXiv:0810.3921.

[44] CMS Collaboration, "Interpretation of Searches for Supersymmetry with simplified Models", *Phys.Rev.* **D88** (2013) 052017, doi:10.1103/PhysRevD.88.052017, arXiv:1301.2175.

[45] J. Hisano, K. Kurosawa, and Y. Nomura, "Natural effective supersymmetry", *Nucl.Phys.* **B584** (2000) 3–45, doi:10.1016/S0550-3213(00)00343-6, arXiv:hep-ph/0002286.

[46] M. Papucci, J. T. Ruderman, and A. Weiler, "Natural SUSY Endures", *JHEP* **1209** (2012) 035, doi:10.1007/JHEP09(2012)035, arXiv:1110.6926.

[47] B. Allanach and B. Gripaios, "Hide and Seek With Natural Supersymmetry at the LHC", *JHEP* **1205** (2012) 062, doi:10.1007/JHEP05(2012)062, arXiv:1202.6616.

[48] ALICE Collaboration, "The ALICE experiment at the CERN LHC", *JINST* **3** (2008) S08002, doi:10.1088/1748-0221/3/08/S08002.

[49] ATLAS Collaboration, "The ATLAS Experiment at the CERN Large Hadron Collider", *JINST* **3** (2008) doi:10.1088/1748-0221/3/08/S08003.

[50] CMS Collaboration, “The CMS experiment at the CERN LHC”, *JINST* **0803** (2008) S08004, doi:10.1088/1748-0221/3/08/S08004,10.1088/1748-0221/3/08/S08004.

[51] LHCb Collaboration, “The LHCb Detector at the LHC”, *JINST* **3** (2008) S08005, doi:10.1088/1748-0221/3/08/S08005.

[52] J.-L. Caron, “LHC Layout. Schema general du LHC.”, (Sep, 1997).

[53] CMS Collaboration, “CMS Luminosity - Public Results”, , (2011). http://twiki.cern.ch/twiki/bin/view/CMSPublic/LumiPublicResults.

[54] CERN, “CMS Compact Muon Solenoid.”, (Feb, 2010). http://public.web.cern.ch/public/Objects/LHC/CMSnc.jpg.

[55] “The CMS Electromagnetic Calorimeter Project: Technical Design Report”. Technical Design Report CMS. CERN, Geneva, 1997.

[56] “The CMS Muon Project: Technical Design Report”. Technical Design Report CMS. CERN, Geneva, 1997.

[57] CMS Collaboration, “The CMS Physics Technical Design Report, Volume 1”, *CERN/LHCC* **2006-001** (2006).

[58] M. Cacciari, G. P. Salam, and G. Soyez, “The anti-k_t jet clustering algorithm”, *Journal of High Energy Physics* **2008** (2008), no. 04, 063.

[59] “Jet Performance in pp Collisions at 7 TeV”, CMS-PAS-JME-10-003, CERN, Geneva, (2010).

[60] X. Janssen, “Underlying event and jet reconstruction in CMS”, CMS-CR-2011-012, CERN, Geneva, (Jan, 2011).

[61] CMS Collaboration, “Determination of jet energy calibration and transverse momentum resolution in CMS”, *Journal of Instrumentation* **6** (2011), no. 11,.

[62] R. Eusebi, “Jet energy corrections and uncertainties in CMS: reducing their impact on physics measurements”, *Journal of Physics: Conference Series* **404** (2012).

[63] CMS Collaboration, “Algorithms for b Jet identification in CMS”, CMS-PAS-BTV-09-001, CERN, 2009. Geneva, (Jul, 2009).

[64] CMS Collaboration, “Performance of b-tagging at $\sqrt{s} = 8$ TeV in multijet, $t\bar{t}$ and

boosted topology events", CMS-PAS-BTV-13-001, CERN, Geneva, (2013).

[65] CMS Collaboration, "Identification of b-quark jets with the CMS experiment", *Journal of Instrumentation* **8** (2013), no. 04,.

[66] CMS Collaboration, "CMS. The TriDAS Project. Technical design report, Vol. 1: The trigger systems",.

[67] CMS Collaboration, "CMS: The TriDAS Project. Technical design report, Vol. 2: Data acquisition and high-level trigger",.

[68] CMS Collaboration, " Calibration and Performance of the Jets and Energy Sums in the Level-1 Trigger", CMS IN 2013/006 (2013), CERN, Geneva, (2013).

[69] CMS Collaboration, " Study of Level-1 Trigger Jet Performance in High Pile-up Running Conditions",.

[70] J. J. Brooke, "Performance of the CMS Level-1 Trigger", CMS-CR-2012-322, CERN, Geneva, (Nov, 2012).

[71] CMS Collaboration, "Search for supersymmetry in final states with missing transverse energy and 0, 1, 2, or at least 3 b-quark jets in 7 TeV pp collisions using the variable alphaT", *JHEP* **1301** (2013) 077, doi:10.1007/JHEP01(2013)077, arXiv:1210.8115.

[72] CMS Collaboration, "SUSY searches with dijet events", CMS-PAS-SUS-08-005, (2008).

[73] L. Randall and D. Tucker-Smith, "Dijet Searches for Supersymmetry at the Large Hadron Collider", *Phys. Rev. Lett.* **101** (Nov, 2008) 221803, doi:10.1103/PhysRevLett.101.221803.

[74] CMS Collaboration, "Search strategy for exclusive multi-jet events from supersymmetry at CMS", CMS-PAS-SUS-09-001, CERN, 2009. Geneva, (Jul, 2009).

[75] CMS Collaboration, "Calorimeter Jet Quality Criteria for the First CMS Collision Data", CMS-PAS-JME-09-008, CERN, 2010. Geneva, (Apr, 2010).

[76] The CMS Collaboration, "Performance of CMS muon reconstruction in pp collision events at 7 TeV", *Journal of Instrumentation* **7** (October, 2012) 2P, doi:10.1088/1748-0221/7/10/P10002, arXiv:1206.4071.

[77] CMS Collaboration, "Search for supersymmetry in events with photons and missing

energy", CMS-PAS-SUS-12-018, CERN, Geneva, (2012).

[78] M. Cacciari and G. P. Salam, "Pileup subtraction using jet areas", *Phys.Lett.* **B659** (2008) doi:10.1016/j.physletb.2007.09.077, arXiv:0707.1378.

[79] Z. Bern et al., "Driving missing data at next-to-leading order", *Phys. Rev. D* **84** (Dec, 2011) 114002, doi:10.1103/PhysRevD.84.114002.

[80] Z. Bern et al., "Driving Missing Data at Next-to-Leading Order", *Phys.Rev.* **D84** (2011) 114002, doi:10.1103/PhysRevD.84.114002, arXiv:1106.1423.

[81] CMS Collaboration Collaboration, "Data-Driven Estimation of the Invisible Z Background to the SUSY MET Plus Jets Search", CMS-PAS-SUS-08-002, CERN, 2009. Geneva, (Jan, 2009).

[82] T. Sjostrand, S. Mrenna, and P. Z. Skands, "PYTHIA 6.4 Physics and Manual", *JHEP* **0605** (2006) 026, doi:10.1088/1126-6708/2006/05/026, arXiv:hep-ph/0603175.

[83] W. Beenakker, R. Hopker, M. Spira, and P. Zerwas, "Squark and gluino production at hadron colliders", *Nucl.Phys.* **B492** (1997) 51–103, doi:10.1016/S0550-3213(97)80027-2, arXiv:hep-ph/9610490.

[84] S. Abdullin et al., "The Fast Simulation of the CMS Detector at LHC", *Journal of Physics: Conference Series* **331** (2011), no. 3,.

[85] S. Banerjee, M. D. Hildreth, and the CMS Collaboration, "Validation and Tuning of the CMS Full Simulation", *Journal of Physics: Conference Series* **331** (2011).

[86] CMS Collaboration, "CMS Btag POG : CMS b-tagging performance database", , (2013). https://twiki.cern.ch/twiki/bin/viewauth/CMS/BtagPOG.

[87] CMS Collaboration, "CMS Luminosity Based on Pixel Cluster Counting - Summer 2012 Update", CMS-PAS-LUM-12-001, CERN, Geneva, (2012).

[88] M. Botje et al., "The PDF4LHC Working Group Interim Recommendations", arXiv:1101.0538.

[89] E. M. Laird, "A Search for Squarks and Gluinos with the CMS Detector",.

[90] R. Cousings, "Probability Density Functions for Positive Nuisance Parameters". 2012. http://www.physics.ucla.edu/cousins/stats/cousinslognormalprior.pdf.

[91] L. Moneta, K. Cranmer, G. Schott, and W. Verkerke, "The RooStats project", 2010. arXiv:1009.1003.

[92] F. James and M. Roos, "Minuit: A System for Function Minimization and Analysis of the Parameter Errors and Correlations", *Comput.Phys.Commun.* **10** (1975) 343–367, doi:10.1016/0010-4655(75)90039-9.

[93] A. L. Read, "Presentation of search results: the CL s technique", *Journal of Physics G: Nuclear and Particle Physics* **28** (2002).

[94] T. Junk, "Confidence level computation for combining searches with small statistics", *Nuclear Instruments and Methods in Physics Research Section A* **434** (1999), no. 23, doi:http://dx.doi.org/10.1016/S0168-9002(99)00498-2.

[95] A. L. Read, "Modified frequentist analysis of search results (the CL_s method)", CERN-OPEN-2000-205, (2000).

[96] G. Cowan, K. Cranmer, E. Gross, and O. Vitells, "Asymptotic formulae for likelihood-based tests of new physics", *The European Physical Journal C* **71** (2011) doi:10.1140/epjc/s10052-011-1554-0.

[97] G. Cowan, K. Cranmer, E. Gross, and O. Vitells, "Asymptotic formulae for likelihood-based tests of new physics", *European Physical Journal C* **71** (February, 2011) doi:10.1140/epjc/s10052-011-1554-0, arXiv:1007.1727.

[98] CMS Collaboration Collaboration, "Search for supersymmetry in final states with missing transverse energy and 0, 1, 2, or at least 3 b-quark jets in 7 TeV pp collisions using the variable alphaT", *JHEP* **1301** (2013) 077, doi:10.1007/JHEP01(2013)077, arXiv:1210.8115.

[99] E. Hardy, "Is Natural SUSY Natural?", *JHEP* **1310** (2013) 133, doi:10.1007/JHEP10(2013)133, arXiv:1306.1534.

Acronyms

ALICE A Large Ion Collider Experiment

ATLAS A Toroidal LHC ApparatuS

APD Avalanche Photo-Diodes

BSM Beyond Standard Model

CERN European Organization for Nuclear Research

CMS Compact Muon Solenoid

CMSSM Compressed Minimal SuperSymmetric Model

CSC Cathode Stripe Chamber

CSV Combined Secondary Vertex

CSVM Combined Secondary Vertex Medium Working Point

DT Drift Tube

ECAL Electromagnetic CALorimeter

EB Electromagnetic CALorimeter Barrel

EE Electromagnetic CALorimeter Endcap

ES Electromagnetic CALorimeter pre-Shower

EMG Exponentially Modified Gaussian

EPJC European Physical Journal C

EWK Electroweak Sector

GCT Global Calorimeter Trigger

GMT Global MuonTrigger

GT Global Trigger

HB Hadron Barrel

HCAL Hadronic CALorimeter

HE Hadron Endcaps

HF Hadron Forward

HLT Higher Level Trigger

HO Hadron Outer

HPD Hybrid Photo Diode

ISR	Initial State Radiation
LUT	Look Up Table
L1	Level 1 Trigger
LEP	Large Electron-Positron Collidor
LHC	Large Hadron Collider
LHCb	Large Hadron Collider Beauty
LO	Leading Order
LSP	Lightest Supersymmetric Partner
NLL	Next to Leading Logorithmic Order
NLO	Next to Leading Order
NNLO	Next to Next Leading Order
POGs	Physics Object Groups
PS	Proton Synchrotron
QED	Quantum Electro-Dynamics
QCD	Quantum Chromo-Dynamics
QFT	Quantum Field Theory
RBXs	Readout Boxes
RPC	Resistive Plate Chamber
RCT	Regional Calorimeter Trigger
RMT	Regional Muon Trigger
SUSY	SUperSYmmetry
SM	Standard Model
SMS	Simplified Model Spectra
SPS	Super Proton Synchrotron
TF	Transfer Factor

TP Trigger Primative

VEV Vacuum Expectation Value

VPT Vacuum Photo-Triodes

WIMP Weakly Interacting Massive Particle